The Bent Coplanar Waveguide at Sub-Terahertz Frequencies

by

Sotiris Alexandrou

Submitted in Partial Fulfillment
of the
Requirements for the Degree
Doctor of Philosophy

Supervised by Professor Thomas Y. Hsiang

Department of Electrical Engineering
College of Engineering and Applied Science

University of Rochester
Rochester, New York

1994

Curriculum Vitae

Sotiris Alexandrou was born in Cyprus on May 26, 1964. He graduated from the Higher Technical Institute, Nicosia, Cyprus in 1987 with a diploma in Electrical Engineering. In 1987, he enrolled at Lehigh University with a scholarship from the Fullbright Amideast Scholarship Program and graduated with his B.S. degree in 1989. He then joined the Department of Electrical Engineering at the University of Rochester and received his M.S. degree in 1990.

During his first year of study at the University of Rochester Mr. Alexandrou was a Teaching Assistant at the Department of Electrical Engineering. Since then, he has been a Research Assistant at the Laboratory for Laser Energetics of the University of Rochester, were he has been a fellow since 1990. His primary research interests lie in the area of optoelectronics and include ultrafast photodetectors, transmission line structures, the physics of semiconductor devices, and the development of femtosecond laser systems.

Mr. Alexandrou is a member of IEEE and OSA.

Acknowledgments

I wish to acknowledge the great help and support of my thesis Advisor, Professor Thomas Y. Hsiang. I would also like to acknowledge the valuable guidance and assistance of Professor Roman Sobolewski, who has been a second Advisor to me. I want to thank them both, not only for their contributions towards this thesis, but more importantly, for offering me their trust and providing me the means to enter the scientific community.

I would like to thank all the students of the "Picogroup" at the Laser Lab for their help on an everyday basis. I would like to acknowledge the assistance of Hiroyoki Nakano (Fujita), Major Bradford Tousley, Larry Golob, and Bill Donaldson during my early days in the research environment. I am also thankful to Matt Warmouth and Naoki Yakapayashi for the time and effort they spend to make the acquisition programs functional. I would also like to express my gratitude for the help of Wei Xiong, Andrew Denysenko, Doug Jakobs-Perkins and Mark Currie. I am also thankful to Doug Dykaar of AT&T Bell Labs, for useful discussions and suggestions. It is with great pleasure that I acknowledge the extensive help of Chia-Chi Wang during the two and a half years we spent in the lab. I am particularly thankful for the efforts he invested so that we could work together as productive team, as well as his constructive suggestions during our long discussions.

I would also like to acknowledge the help Professor Philippe Fauchet and the members of his group, together with the staff in the Illustrations Department at the Laser Lab.

Θελω να ευχαριστησω τους γονεις μου, καθως και ολη μου την οικογενεια, γιατι μου εδωσαν την ευκαιρια που αυτοι ποτε δεν ειχαν.

Abstract

Recent advancements in the field of high speed electronics put increasing pressure on the development of active devices that can operate at increasingly faster rates. However, at the frequency range of several GHz and above, loss and dispersion in the interconnecting transmission lines are dramatically enhanced. The elaborate characterization of such structures then becomes instrumental in the overall performance of ultrafast circuits. This thesis focuses on this aspect and presents a broad-band experimental characterization of coplanar transmission lines that extends to the THz range.

Our samples were fabricated on semi-insulating GaAs substrates using a lift-off process. Both coplanar waveguides and coplanar strips with different dimensions were fabricated. Various straight and bent lines with different geometries were included. The transmission lines were excited by picosecond electrical transients generated by the illumination of photoconductive switches embedded in the lines. The time evolution of these transients was recorded by a subpicosecond electro-optic sampling system.

Subsequent analysis of the experimental results was initially carried out in the time domain. With the development of a suitable pulse generation scheme and data processing algorithms, the analysis was also extended to the frequency domain. It included a study of the various transmission lines which incorporated the effects of lateral dimensions, ground plane width, bends, and wirebonds together with the evolution of the CPW even mode. When the transmission lines were excited by step-like electrical transients, our time-domain studies were based on the study of propagation velocity and the evolution of the signal's rise time. With the implementation of picosecond pulses the analysis was also extended to the qualitative comparison of loss and dispersion in the lines. Quantitative results on the effective dielectric permittivity, dispersion, and attenuation were extracted by frequency domain analysis that extended to frequencies up to 1 THz. With these results we provide a complete high-frequency characterization of the coplanar transmission lines.

Table of Contents

List of Figures

List of Tables

1. Introduction

1.1 Motivation

The field of semiconductor electronics is expanding at an impressive rate. Recent advances in materials and photolithography, as well as growth and processing techniques, facilitate the development of increasingly superior devices and circuits. With the development of heterostructures, both the High Electron Mobility Transistor (HEMT) and the Heterojunction Bipolar Transistor (HBT) have been able to achieve frequencies of operation in the range of 400 GHz[1]. Even the less exotic Si-Ge bipolar, as well as the silicon MOSFET, have demonstrated operation around 100 GHz [2, 3]. Simpler devices, such as photodetectors and Resonant Tunneling diodes can operate at even faster rates. For instance, the fastest photodetectors have 3-dB bandwidths in excess of 0.5 THz [4]. On the systems level, microprocessors with a 50 ps clock cycle are already being proposed [5]. In addition, Monolithic Microwave Integrated Circuits (MMICs) made on III-V substrates have already demonstrated operational frequencies up to 140 GHz [1]. Moreover, optical modulators which can utilize the immense bandwidth of optical fibers to transfer information, can now operate at frequencies up to 40 GHz [6].

These developments on both the device and circuit level put increasing pressure for advancements in two other directions. The first is the establishment of a new generation of testing tools that are able to accommodate the wide bandwidths of the new devices. Traditional oscilloscopes can only provide information below 50 GHz. Microwave network analyzers can operate at higher frequencies, but testing can only be performed at single frequency at a time. Moreover, losses in probes and connectors increase with frequency and degrade the accuracy of the results.

The other problem, which also arises from the increasing frequency of operation of ultrafast circuits, is the loss and dispersion induced by the interconnecting transmission lines. In the KHz-MHz range, designers are used to treating interconnects as perfect conductors. However, in the GHz range, the transmission-line characteristics often become the limiting factor in the overall performance of high-speed circuits. Attenuation and dispersion induced by the interconnects are very important; so are reflections caused by bends and other

discontinuities. In addition, the actual amount of time signals require to reach different active devices becomes increasingly significant.

This thesis will focus on the characterization of transmission lines that can be used as interconnects in ultrafast MMICs. In order to achieve this primary goal we have also developed a testing tool which can be readily implemented for the broadband characterization of a *wide range* of ultrafast devices and circuits.

1.2 Status of transmission line characterization

Traditionally, the microstrip was the transmission line most frequently used in MMICs. However, the CPW [7] is increasingly becoming the interconnection medium of choice for high speed applications. The CPW has a number of advantages over the microstrip transmission line because it is a planar structure with very low dispersion and substrate sensitivity. It also enables easy mounting of shunt and series elements without the implementation of via holes through the substrate. Finally, it allows a larger propagation velocity than a microstrip on a substrate with the same dielectric constant.

The studies of straight coplanar transmission line structures, suitable for high-speed interconnects, have been the subject of intensive research in the past [8-14]. Both normal conductor [8-11] and superconducting [12-14] lines have been investigated. However, apart from a single attempt to characterize one CPW and one coplanar strip (CPS) in the frequency domain, all other experimental work was limited to time-domain analysis [9]. Moreover, previous studies of bent coplanar transmission lines were primarily limited to the low frequency regime, where the bends were treated as point discontinuities [15]. Recent work has increased the range of characterization to higher frequencies [16, 17] but experimental treatment was still limited to less than 40 GHz. The increased complexity and speed of modern MMIC's however, calls for careful characterization of transmission lines at much higher frequencies. This work will focus on the properties of straight and bent CPW's in the sub-THz frequency range.

At the time the research for this thesis was initiated, the available tools suitable for ultrafast measurements were sampling techniques. Electro-optic sampling was a demonstrated method with high frequency potential. External electro-optic sampling, which seemed to be the most promising, was based on the CPM dye laser

that offered a few tens of mW of light power as a fixed wavelength—usually at 620 nm. Judging from the volume of data produced at that time, such systems required improvements in order to become solid, reliable tools. Internal electro-optic sampling, using GaAs circuits and infrared lasers, was also demonstrated [18]. This system, however, had an inferior bandwidth performance, because of the ps pulse duration of the IR lasers. Moreover, its practicality was questionable because the substrate had to be both electro-optic and transparent. Photoconductive methods were also used [19] but with similar limitations. In order to provide high temporal resolution, they required a substrate with ultrashort carrier lifetime— a characteristic that is usually incompatible with high speed devices and circuits.

For the ultrafast characterization of a device or circuit, it is required that the device under test is excited by ultrafast *electrical* signals. The transition from a femtosecond or picosecond optical pulse to an electrical waveform with a rise time of the order of a picosecond could be done with the implementation of photoconductive switches [20]. In order to achieve comparable falltimes and generate pulses, it was necessary to reduce the substrate lifetime. On high quality substrates, such as semi-insulating GaAs, only picoseconds step-like transients could be generated at that time.

Because of the intrinsic problems involved with the excitation with step transients, the analysis of the results was almost always done in the time domain. Another reason was that such measurements were initiated by researchers in the laser community who are accustomed to time rather than frequency domain analysis. Early attempts to present results in the frequency domain were primarily limited to frequencies less than 100 GHz [21, 22].

The proposal for this thesis set a number of objectives whose implementation could enable the complete characterization of the transmission lines. We started with a time-domain study with the excitation of step transients on straight and bent transmission lines. The initial analysis provided valuable results, but at the same time indicated that a spectral approach was necessary. For the correct implementation of spectral analysis a reliable pulse generation scheme was required. It would also be much preferred if this could be implemented on a high quality substrate. Once a picosecond pulse generation scheme was available, we could continue with the time domain analysis of picosecond pulses in order to extract additional information about the transmission lines. Comparative studies could readily give results on both attenuation and dispersion. However, in order to give solid, quantitative results on the

transmission line characteristics, a frequency-domain analysis was necessary. This would require some effort to understand the problems and limitation associated with spectral analysis, and write the machine code to transfer and manipulate the data in the frequency domain.

With the completion of this thesis _all_ of the above objectives have been achieved. In the meantime, some other benefits have surfaced from this research. Because their scope is diverse and is not directly related to our main objective, only a small part of these additional results will be discussed in this thesis.

1.3 A thesis overview

The thesis is organized in the following manner: Chapter 2 starts with a description of the measurement tool— the electro-optic sampling system. Its principle of operation, features and performance characteristics, which demonstrate that this system defines the state of the art, are described in detail. Chapter 3 gives an overview of the CPW characteristics. We present the formalism through which the line impedance and phase velocity are estimated, together with the influence of the transmission line parameters on attenuation and dispersion. Discontinuities, and their role in the excitation of the unwanted even mode, are also discussed. Chapter 4 is dedicated to the description of the actual transmission lines. First, we discuss the fabrication procedure and the geometrical features of the various lines. The chapter is completed with a brief overview of the different methods of electrical-pulse generation.

The experimental data is presented in the last 3 chapters. The results on propagation of picosecond step-like transients on a range of straight and bent CPWs are introduced in chapter 5. Our findings on propagation velocity and signal distortion are presented, together with the role of wirebonds and the excitation of the even mode. The time domain characterization of a family of coplanar lines with picosecond _pulses_ is introduced in Chapter 6. The effects of lateral dimensions, ground plane width, bends and wirebonds on the behavior of the transmission lines are discussed in detail. The time evolution of signal velocity and a comparative study of attenuation and dispersion in the lines are also presented. Chapter 7 starts with a brief introduction to the fundamentals of frequency domain analysis. Spectral results on

attenuation and dispersion in each line are presented for frequencies up to 1 THz. In this manner we have been able to estimate the influence of the various features on the frequency dependent characteristics of the transmission lines in a *quantitative* way.

Chapter 7 is followed by a summary of the main points of the thesis and an overview of the conclusions we have reached. The algorithms written for the processing of the experimental data and the implementation of the frequency domain analysis are presented in the Appendix.

The main accomplishments of this thesis can be summarized as follows:

• The development of a state-of-the-art electro-optic sampling system, with subpicosecond temporal resolution and *microvolt* sensitivity, based on a tunable titanium doped sapphire laser. In addition, a fiber coupler was implemented to enable practical testing on the chip level, and the electro-optic crystal was redesigned to improve accuracy and enable *contact-free* sampling, even at ultrashort distances.

• The development of two powerful schemes for the generation of ultrashort electrical pulses on high quality substrates: One with the use of nonuniform illumination of photoconductive switches, and the other with the implementation of nanoscale metal-semiconductor-metal photodiodes.

• The complete time *and* frequency domain characterization of coplanar strips and waveguides. A comparative study of the various transmission lines which included the effects of lateral dimensions, ground plane width, bends, and wirebonds was presented, together with the evolution of the CPW even mode.

• The demonstration of a broad-band, frequency-domain analysis tool which not only can be used for the fast and accurate characterization of transmission lines but also ultrafast active devices and circuits.

A number of aspects that originated from the research dedicated to this thesis have expanded into different directions. In time, their scope diversified and they grew independently into separate projects. For this reason, they will only be briefly introduced in this thesis. For the complete and accurate information of the dedicated reader, a number of our papers are referenced at the relevant chapters. These additional projects are listed below.

- The nanoscale metal-semiconductor-metal photodiode which was fabricated on a range of substrates, such as low-temperature MBE-grown and semi-insulating GaAs, silicon, and silicon-on-insulator. The influence of metal finger separation and light wavelength on the temporal response and sensitivity of the devices was examined in detail, together with the dependence on biasing voltage and light intensity.

- The role of nonuniform gap illumination on the generation of subpicosecond electrical pulses on GaAs. With 2-dimensional electro-optic sampling we have been able to explain that the mechanism of this pulse generation technique arises from carrier-induced field screening. In addition, we plan to use the part of the radiated energy to conduct free space radiation experiments.

- The development of a reliable and practical sampling system with ultrahigh bandwidth and superb sensitivity, coupled with the analysis tools for spectral analysis constitute a powerful instrument. This tool, which is essentially a combination of an oscilloscope and a spectrum analyzer, is already being used for the characterization of high-speed single flux quantum superconducting circuits [23].

References

[1]   L. D. Nguyen, "InP high electron mobility transistors: status and promise," OSA Proceedings on Ultrafast Electronics and Optoelectronics, S. Shah and U. Mishra, eds., vol. 14, pp. 82-84, 1993 and references therein.
Also, A. A. Grinberg, and S. Luryi, "Theory of ultra high frequency performance heterojunction bipolar transistors," OSA Proceedings on Ultrafast Electronics and Optoelectronics, S. Shah and U. Mishra, eds., vol. 14, pp. 71-76, 1993.

[2]   R. H. Yan, K. F. Lee, Y. O. Kim, D. Y. Jeon, and E. H. Westerwick, "Ultra-deep submicron Si MOSFETs with f_T exceeding 100 GHz," OSA Proceedings on Ultrafast Electronics and Optoelectronics, S. Shah and U. Mishra, eds., vol. 14, pp. 60-64, 1993.

[3]   G. L. Patton, et al, "75-GHz f_T SiGe-base heterojunction bipolar transistors," *IEEE Electr. Dev. Lett.*, vol. 11, pp. 171-173, April 1990.

[4]   Y. Liu, S.Y. Chou, T. Y. Hsiang, S. Alexandrou, "Ultrafast Nanoscale Metal-Semiconductor-Metal Photodetectors on Bulk and Low Temperature Grown GaAs," *Appl. Phys. Lett.*, vol. 61, pp. 819–1821, August 1992

[5]   R. W. Keyes, and M. B. Ketchen, "A 50 ps cycle-time microprocessor: the technological challenges," OSA Proceedings on Ultrafast Electronics and Optoelectronics, S. Shah and U. Mishra, eds., vol. 14, pp. 56-59, 1993.

[6]   T. Ikegami, and K. Kubodera, "Overview of the applications of high speed electronics," OSA Proceedings on Ultrafast Electronics and Optoelectronics, S. Shah and U. Mishra, eds., vol. 14, pp. 1-5, 1993.

[7]   C.P. Wen, "Coplanar waveguide: A surface strip transmission line suitable for nonreciprocal gyromagnetic device applications," *IEEE MTT.*, vol. 17, No. 12, pp. 1087-1090, December 1969.

[8]   D. R. Dykaar, A. F. J. Levi, and M. Anzlowar, "Ultrafast coplanar air-transmission lines," *Appl. Phys. Lett.*, vol. 57, pp. 1123–1125, September 1990.

[9]   M. Y. Frankel, S. Gupta, J. A. Valdmanis, and G. A. Mourou, "Terrahertz attenuation and dispersion of coplanar transmission lines," *IEEE MTT.*, vol. 39, no. 6, pp. 910-916, June 1991.

[10] D. S. Phatak, N. K. Das, and A. P. Defonzo, "Dispersion characteristics of optically excited coplanar striplines: comprehensive full wave analysis," *IEEE MTT.*, vol. 38, pp. 1719–1730, November 1990.

[11] M. Riaziat, R. Majidi-Ahi, and I.-J. Feng, "Propagation modes and dispersion characteristics of coplanar waveguides," *IEEE Trans. Microwave Theory Tech.*, vol. 38, no. 3, pp. 245–251, March 1990.

[12] J. F. Whitaker, R. Sobolewski, D. R. Dykaar, T. Y. Hsiang, and G. A. Mourou, "Propagation model for ultrafast signals on superconducting dispersive lines," *IEEE MTT.*, vol. 36, pp. 227–285, February 1988

[13] D. R. Dykaar, R. Sobolewski, J. M. Chwalek, J. F. Whitaker, T. Y. Hsiang, G. A. Mourou, D. K. Lanthrop, S. E. Russek, and R. A. Buhrman, "High-frequency characterization of thin-film Y-Ba-Cu oxide superconducting transmission lines," *Appl. Phys. Lett.*, vol. 52, pp. 1444–1446, April 1988.

[14] M. C. Nuss, K. W. Goossen, P. M. Mankiewich, R. E. Howard, B. L. Straughn, T. E. Harvey, G. W. Berkstresser, and C. D. Brandle, "$YBa_2Cu_3O_7$ superconductors for high-speed interconnects," *IEEE Electron Dev. Lett.*, vol. 11, pp. 200–202, May 1990.

[15] R. N. Simonns, G. E. Ponchak, K. S. Martzaklis, and R. R. Romanofsky, "Channelized coplanar waveguide: discontinuities, junctions, and propagation characteristics," *IEEE Int. Sump. Digest*, pp. 915–918, 1989.

[16] N. I. Dib, G. E. Ponchak, and L. P. B. Katehi, "A theoretical and experimental study of coplanar waveguide shunt stubs", *IEEE MTT*, pp. 38-42, vol. 41, No. 1, January 1993

[17] A. A. Omar and Y. L. Chow, "A versatile moment method solution of the conventional and modified coplanar waveguide T-junctions, *IEEE MTT*, pp. 687-692, vol. 41, No. 4, April 1993

[18] B. H. Kolner and D. M. Bloom, "Electrooptic sampling in GaAs Integrated circuits," *IEEE JQE.*, vol QE-22, No. 1, pp. 79-93, January 1986.

[19] C. Shu, X. Wu, E. S. Yang, X.-C. Zhang, and D. H. Auston, "Propagation characteristics of picosecond electrical pulses on a periodically loaded coplanar waveguide," *IEEE MTT.*, vol. 39, No. 6, pp. 930-935, June 1991.

[20] D. H. Auston, "Picosecond photoconductors: physical properties and applications," Picosecond optoelectronic devices edited by C. H. Lee, Academic press, 1984

[21] S-L. L. Huang, E. A. Chauchard, C. H. Lee, H-L. A. Hung, T. T. Lee and T. Joseph, "On wafer photoconductive sampling of MMICs," *IEEE MTT*, vol. 40, pp. 2312-2320, December 1992

[22] A. Deutch , G. Arjavalingam, and G. V. Kopcsay, "Characterization of resistive transmission lines by short-pulse propagation," *IEEE Microwave and Guides Wave Lett.*, vol. 2, pp. 25-27, January 1992.

[23] T. Y. Hsiang, C.-C. Wang, A. Denysenko, S. Alexandrou, R. Sobolewski, "An Electro-Optic Sampling System for Ultrafast Testing of Superconducting Circuits," presented at the International Superconducting Electronics Conference, Boulder , Colorado 93.

2. The Electro-optic Sampling System

This chapter is devoted to the electro-optic sampling system — the work horse of this research. The electro-optic sampler is an ultrafast scope that takes advantage of the fine temporal resolution of a femtosecond laser to probe electric field through a non-linear crystal. When the crystal is placed atop an electronic device, or circuit, the adjacent electric field induces a birefringence in the crystal (the Pockels effect) and the temporal profile of the field is recorded by the laser beam as a change in its state of polarization. Since the speed of the system is essentially determined by the optical pulse width of the laser, the time resolution falls well into the subpicosecond regime. Because the measurement is done optically, the speed requirements on the systems electronics can be very relaxed. Most devices and circuits, however, function with voltages in the range of millivolts to a few volts. The electric fields that correspond to these voltages induce a very small change in birefringence in most electro-optic materials and in order to minimize noise and achieve submillivolt sensitivity, a number of issues have to be addressed.

In this chapter we will describe the electro-optic sampling system in detail with special emphasis given to a set of factors that are instrumental in understanding the functionality of the sampler. The femtosecond laser is presented in the first section together with a brief overview of the system. The second section describes the electro-optic amplitude modulator, while the third examines the issue of voltage sensitivity. Section 4 concentrates on the merits of optimal crystal design, section 5 focuses on the temporal resolution, and section 6 addresses the issue of signal reproducibility. During our description, we will point out the performance limits of the system through a set of experimental results.

2.1   The femtosecond laser and a system overview

As we have mentioned in the introduction, the heart of the electro-optic sampler is a femtosecond laser. Among the first lasers to be used in such a system [1] was the colliding pulse mode-locked (CPM) dye laser [2]. Starting in the mid 1980's, the CPM became the standard laser source for subpicosecond electro-optic samplers mainly because of it relative stability and superior temporal resolution. Even though its organic dyes were toxic and had a lifetime of the order of a month, this laser could readily provide stable pulses with a temporal duration of ~ 50 fs. Its wavelength of operation was 620 nm with an output power of ~40 mW (for both beams), and a repetition rate of ~ 100 MHz.

The development of the superior titanium doped sapphire (Ti:Al$_2$O$_3$) laser in the early 1990's overshadowed the CPM very quickly. This laser is inherently more stable and durable because it is based on a solid state gain medium—a sapphire crystal that does not degrade and is virtually indestructible. Moreover, the Ti:Al$_2$O$_3$ laser is tunable, offering light wavelengths starting from the red and extending well into the near IR by more than 300 nm. It can offer an average output power of the order of a Watt for most of this spectrum (almost 2 orders of magnitude greater than the CPM). More importantly, the high power coupled with the stability of this laser make frequency doubling and optical parametric amplification [3] practical, extending the usable bandwidth in both the UV and IR regions. Optical pulses as short as 13 fs [4] have been demonstrated but at the expense of wavelength tunability. Slightly longer pulses, between 100 and 200 fs, can be generated throughout the whole gain spectrum of Ti:Al$_2$O$_3$.

The electro-optic sampler described in this thesis initially used a home made CPM laser source. The results presented in chapter 5 were taken with this laser. In its current configuration, however, the system uses a commercial continuous wave (CW) mode locked Ti:Al$_2$O$_3$ femtosecond laser (Coherent Mira 900) as shown in Fig. 2.1. The Ti:Al$_2$O$_3$ is pumped by a commercial CW argon ion laser (not shown in the Figure) with all visible lines at an average power of ~12W. When the Ti:Al$_2$O$_3$ laser is mode locked it generates ~140 fs pulses [5] with an average power of 1-2 watts at wavelengths ranging between 700 and 1000 nm. Three separate mirror sets with a bandwidth of ~ 100 nm each are required to cover the whole lasing spectrum. The laser runs at a frequency of the 76 MHz determined by its cavity length. The inverse of this

frequency, which gives the temporal spacing between two consecutive laser pulses (13.2 ns) is an important parameter since it determines the maximum time window the system can scan. Any measured event has to recover to its original state within this time interval to avoid signal-overlap between neighboring transients.
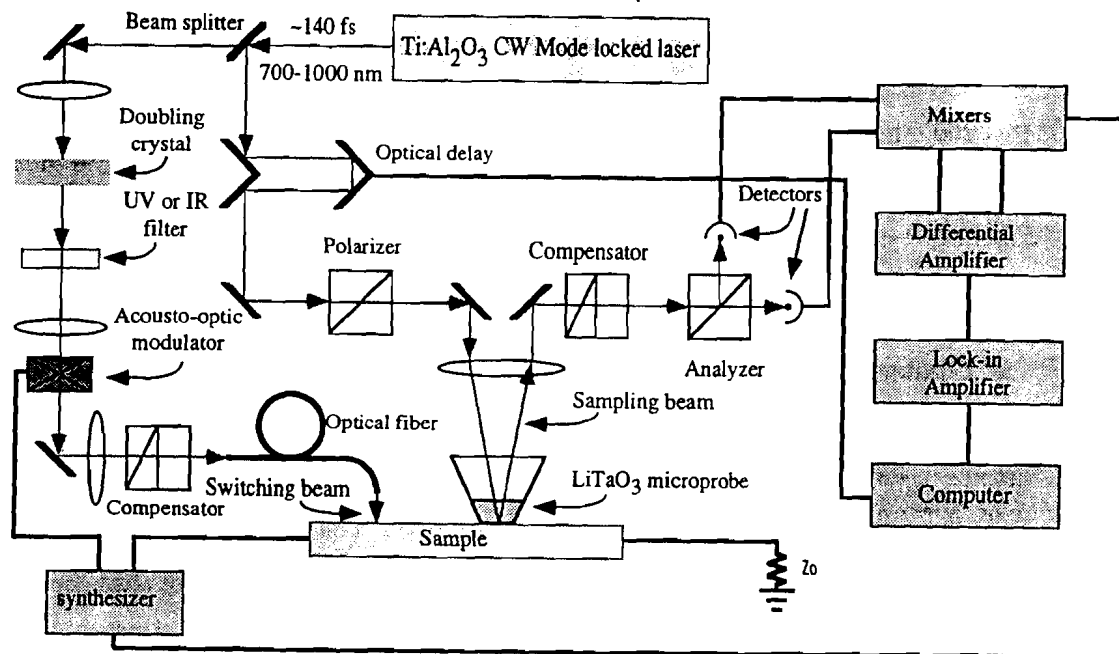
Fig. 2.1   A schematic representation of our electro-optic sampling system.

The laser output is first divided into the switching and sampling beams by a 30/70 % beam splitter. The switching beam, which is more powerful, is focused on a BaB_2O_4 crystal (BBO) and part of it is frequency doubled in the UV-blue region. A spectral filter chooses between the fundamental or the second harmonic. The beam is then modulated acousto-optically to reduce noise (the details of the frequency modulation scheme will be discussed in section 3) and guided to the sample through a single-mode optical fiber. Thus a train of femtosecond pulses from the switching beam excite an optoelectronic transducer (such as a photoconductive switch) to generate an electrical transient as shown in Fig. 2.2. (The photoconductive switch, as well other schemes of generating electrical pulses by optical means, will be described in Chapter 4). The electrical waveform can either be used to trigger a circuit under test or can be measured directly as shown in the figure.

The sampling beam travels through a delay line and then through an electro-optic LiTaO3 crystal tip. Any electric field parallel to the optical axis of the crystal introduces a birefringence in the material, which in turn alters the polarization of the probing beam as it propagates through the crystal. As we shall see in section 2, the analyzer (Fig. 2.1) converts this change in polarization to amplitude modulation. The detectors carry the optically encoded information to the electronic part of the system for frequency conversion and averaging. Using the delay line to change the relative path of the two light beams creates a time-domain mapping of the electric field in the crystal which is recorded by the computer.
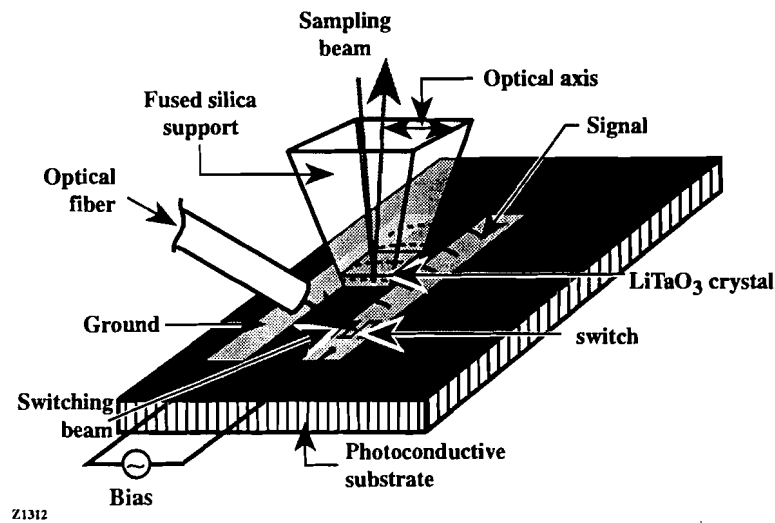
Fig. 2.2 A demonstration of the principle of external electro-optic sampling.

2.2 Electro-optic amplitude modulator

A crucial part of the sampling system is the section along the path of the sampling beam near the LiTaO3 crystal between the polarizer and the analyzer (Fig. 2.1), which forms an electro-optic amplitude modulator [6]. The input polarizer ensures that the polarization of the incident light pulses forms an angle of 45 degrees with respect to the optical axis of the LiTaO3 crystal shown in Fig. 2.2. Since the electro-optic effect in LiTaO3 is transverse, the direction of the sampling beam has to be perpendicular to the optical axis of the crystal. In this case, the laser beam is experiencing a retardation (Γ) given by Eq. 2.1[7]

$$\Gamma = \frac{4\pi}{\lambda}\left(n_e - n_o\right)d - \int_0^d \frac{2\pi}{\lambda}\left(n_e^3 r_{33} - n_o^3 r_{13}\right) E\, r(z)\, dz \qquad (2.1)$$

where n_O and n_e are the ordinary and extraordinary indices of refraction, r_{33} and r_{13} are the corresponding elements of the permeability tensor. The wavelength of the laser light is given by λ, the parameter d denotes the thickness of the crystal, while E is the magnitude of the electric field parallel to the optical axis and $r(z)$ expresses the field variation in the z direction. The first term in Eq. 2.1 gives the static retardation which arises from the crystal anisotropy and does not depend on electric field. The second term, on the other hand, is proportional to E and describes the contribution of the Pockels effect.
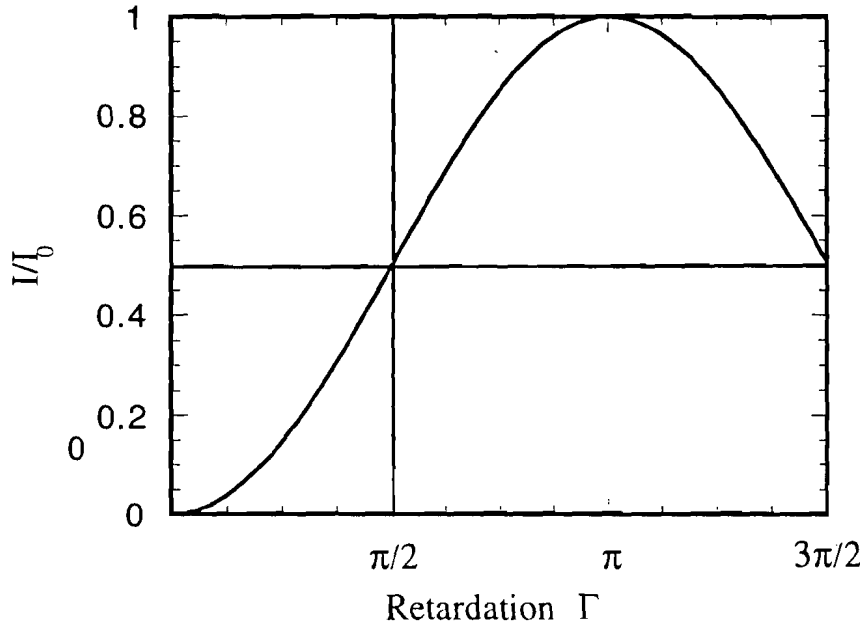
Fig. 2.3   The transfer function of the amplitude modulator as per Eq. 2.2.

When the direction of polarization of the analyzer is orthogonal to the one of the polarizer before the crystal, the ratio of the transmitted to the incident light intensity (I_τ/I_O) is given by Eq. 2.2 and is plotted in Fig. 2.3.

$$I_\tau/I_o = \frac{\left(1 + \sin(\Gamma)\right)}{2} \qquad (2.2)$$

Because the thickness of the crystal is small, even a field of ~ 1 kV/cm induces a retardation only on the order of 10^{-3} rad. The value of the static retardation is even smaller. Under these conditions the operating point in Fig. 2.3 is very close to the origin unless extra retardation is added by the compensator. Of course, one would like to have the operating point at a position where the sensitivity is maximum. In other words, in a position where the smallest change in retardation would cause the largest change in the value of the transmitted intensity. This occurs when the compensator is adjusted to make the total retardation equal to $\pi/2$. More importantly, in the neighborhood of $\Gamma = \pi/2$ the transmitted intensity is a linear function of retardation and consequently ΔI_τ becomes directly proportional to E as indicated by Eq. 2.3.

$$\frac{\Delta I_\tau}{I_\tau} = \frac{\pi\,d}{\lambda}\left(n_e^3 r_{33} - n_o^3 r_{13}\right) E \int_0^d r(z)\,dz \qquad (2.3)$$

An increase in retardation, caused by a higher value of the electric field E, will increase the transmitted light intensity to $I_\tau + \Delta I_\tau$ and at the same time decrease the intensity of the deflected beam to $I_\tau - \Delta I_\tau$. Both beams are then fed to a pair of reverse biased PIN photodiodes and the electrical signals are amplified differentially to a value of $K[(I_\tau+\Delta I_\tau)-(I_\tau-\Delta I_\tau)] = 2K\Delta I_\tau$, where K is the amplification factor. Thus, differential amplification increases the detected signal by a factor of two and improves the signal to noise ratio drastically by rejecting the vast amount of noise included in the common mode signal since $I_\tau >> \Delta I_\tau$.

2.3 Frequency modulation scheme and noise reduction requirements

In section 2 we noted that even strong electric fields cause minimal changes in retardation and as a consequence, the ΔI_τ is frequently smaller than I_τ by more than four orders of magnitude. The low-frequency noise levels of femtosecond lasers, on the other hand, lie in the neighborhood of 1-2 % RMS at best. Under these conditions, it is evident that a direct measurement is a hopeless task. The first step towards improving sensitivity is to employ differential detection in the manner described in the

previous section. Further improvement can be achieved by the detailed frequency modulation scheme described here.

In order to attack the problem of noise in the right direction the spectral characteristics of the femtosecond laser have to be well understood. In Fig. 2.4 we show an illustration of the noise spectrum of the Ti:Al2O3 laser. At low frequencies and up to approximately 500 KHz the 1/f noise dominates [8], but for higher frequencies, the noise characteristic levels off to a plateau. Ideally, one would like to operate the detection system at audio frequencies, because in this range the noise characteristics of the lock-in and differential amplifiers (see Fig. 2.1) are optimal. However, if we choose to operate in this mode a large amount of 1/f noise would fall directly into the detection system. In order to avoid these shortcomings we employ the technique of frequency mixing as developed by Chwalek and Dykaar [9].
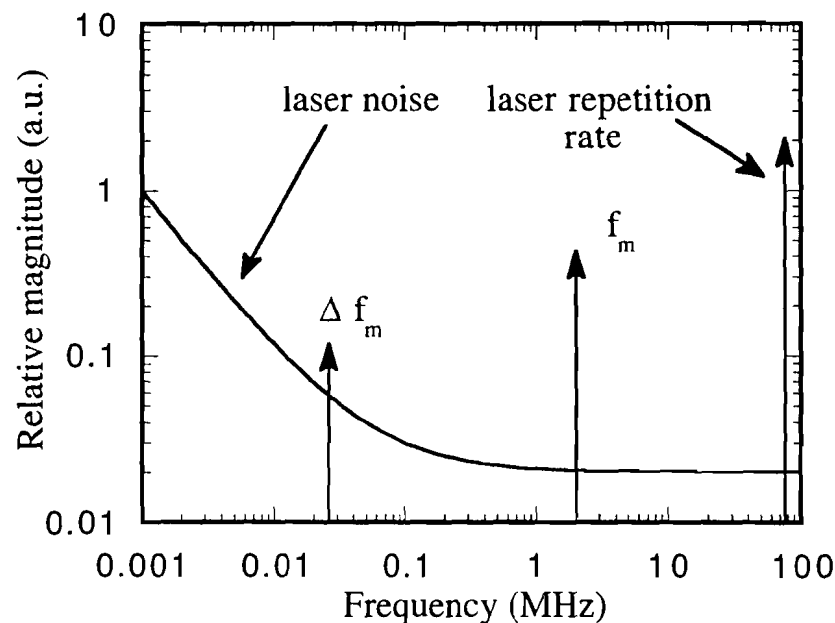
Fig. 2.4   An illustration of the noise spectrum of the Ti:Al2O3 laser together with the modulation scheme used to avoid the 1/f noise.

In this technique, the switching beam is modulated by the acousto-optic modulator at a frequency f_m = 2 MHz, much higher than the 1/f noise limit. The switching beam excites an electrical signal which transfers the modulation to the

sampling beam when the waveform is probed at the LiTaO₃ crystal. The optical signals are first converted to electrical current by the photodiodes and then fed to two identical frequency mixers. At this stage both signals are modulated at a second frequency $f_m + \Delta f_m$, where Δf_m = 2.55 KHz. Mixing the signals at these two frequencies generates one sideband in the audio range (Δf_m) and another in the megahertz range ($2f_m + \Delta f_m$, not shown in Fig. 2.4). After differential amplification, the lock-in filters out the high frequency signal and only averages the preferred audio sideband. In this manner the 1/f noise is completely bypassed even though the detection is done at low frequencies.

In order for the mixing scheme to function accurately it is required that the optoelectronic transducer, which converts the laser pulses into electrical waveforms, responds linearly to light intensity. If this condition is not satisfied, the transducer nonlinearity will distort the measured waveform. An alternative approach is to modulate the circuit's biasing voltage rather than the switching beam (see Fig. 2.1). Obviously, this option will only work if the transducer responds linearly to the bias voltage. The linearity requirements can be dropped if the switch beam is modulated by a square wave. In this case the modulating waveform contains components at both the fundamental frequency and the higher-order harmonics as shown in Eq. 2.4

$$F_{(\omega)} = \left(\frac{4}{\pi}\right) \sum_{1}^{2n+1} \frac{1}{n} \sin(n\omega t) \tag{2.4}$$

A study of the modulation scheme shows that only the fundamental will contribute to the signal sideband that is averaged by the lock-in amplifier (see Fig. 2.4). Its amplitude, however, will be larger by a factor of $4/\pi$ and the magnitude of the measured waveform will be amplified accordingly. This factor has been overlooked in the calibration of previous sampling measurements.

In the case where the system is limited by the shot noise of the detectors, the theoretical signal sensitivity falls in the range of 100 $\mu V/\sqrt{Hz}$ [10]. In practice the ultimate signal to noise is determined by two parameters: the averaging time constant of the lock-in amplifier, and the total data acquisition time. With the use of data averaging we have been able to reach a voltage sensitivity of less than 100 μV as shown in Fig. 2.5. The data displayed in this figure represent the electrical response of a silicon metal-semiconductor-metal (MSM) photodiode when excited by a 5 fJ violet optical pulse. An

acquisition time of two hours was required to achieve a < 100 μV sensitivity with a bandwidth of 500 GHz over a time span of 100 ps. This measurement demonstrates the highest sensitivity ever achieved with an electro-optic sampling system.
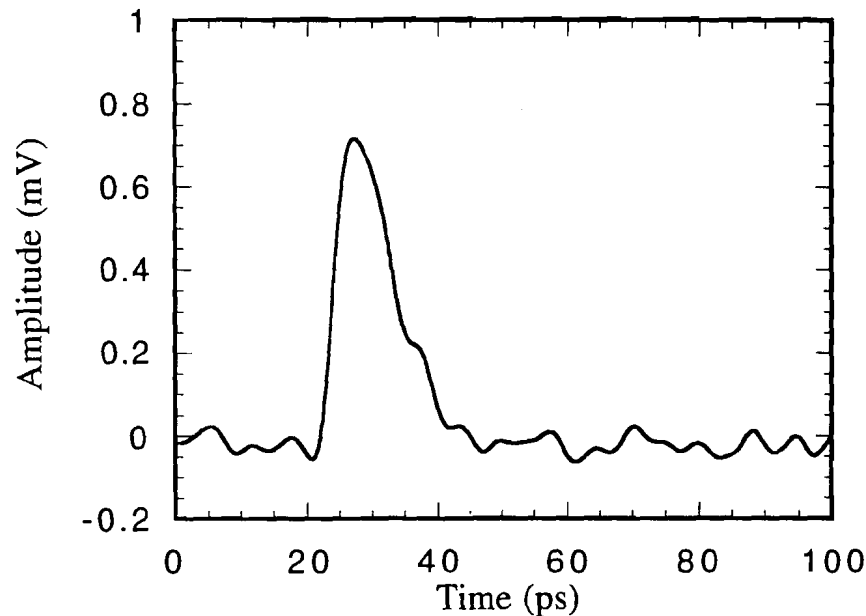
Fig. 2.5 A sub-millivolt electrical pulse generated by a Silicon MSM photodiode when illuminated by a 5 fJ optical pulse at a wavelength of 400 nm.

2.4 Electro-optic crystal design

Apart from the frequency-mixing scheme we just described, submillivolt sensitivity requires that the design of the electro-optic crystal be optimal. The choice of electro-optic material is, of course, of primary importance. The material most commonly used for external sampling is $LiTaO_3$ because it combines a high electro-optic coefficient with excellent mechanical properties. The disadvantage is that this material has a high dielectric constant at microwave frequencies ($\varepsilon_r = 43$) which can cause significant capacitive loading. AlGaAs, which has an ε_r around ~11, was also investigated [11], but it has a relatively small bandgap (> 1.6 eV) which may allow significant light absorption by in-gap subbands. Another promising material is SiC

[12]. It has a high bandgap of 2.2 eV, low dielectric constant (~11) and a high electro-optic coefficient coupled with unsurpassed mechanical properties. We have manufactured crystal probes using this material and their characterization is currently under way. All electro-optic measurements reported in this thesis were done with small LiTaO3 probes.
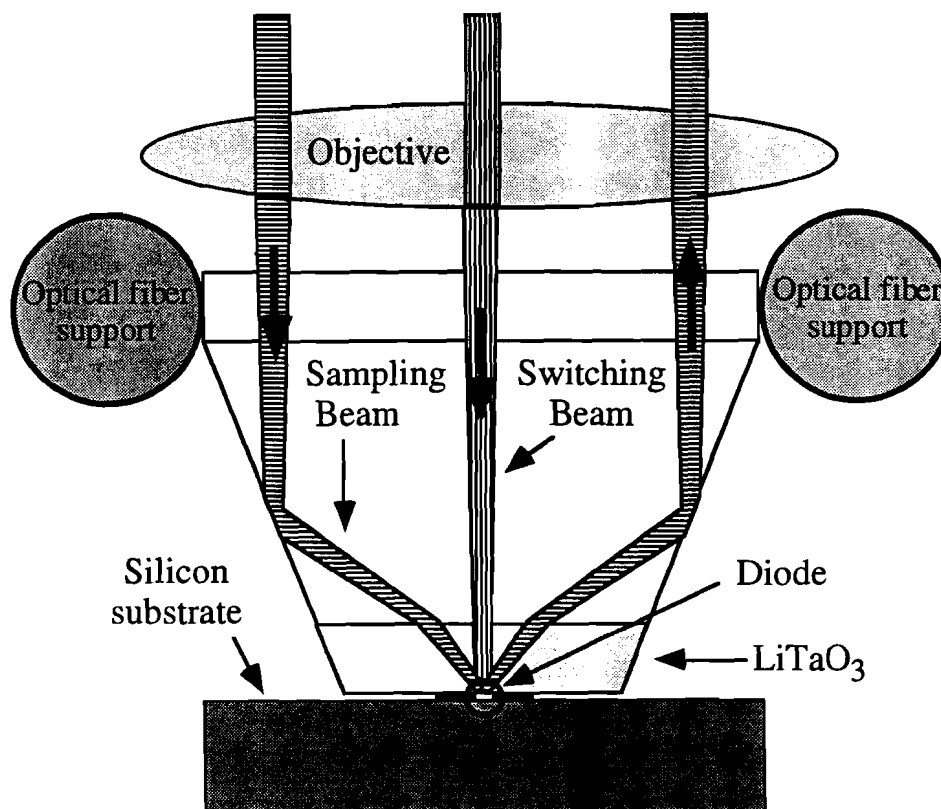
Fig. 2.6 Electro-optic sampling at short propagation distances, with the sampling beam in the total internal reflection mode and the switching beam incident on the device under test (an Si MSM photodiode) through the LiTaO3 crystal tip.

The advantage of having a small, movable crystal probe in a pyramid shape was recognized from the early days of electro-optic sampling [1] (see Fig. 2.2). The small size of the probe tip makes fine positioning practical and reduces the capacitive loading to the circuit or device under test. When the front face of the crystal is coated by a high reflectivity dielectric layer the probe beam can hit the crystal-dielectric interface and bounce back directly, as shown in Fig. 2.2. The disadvantage of this implementation is that when the electric field is concentrated near the surface of the structure, sensitivity

can be reduced. More importantly, the dielectric limits the range of light wavelengths that can be used for sampling.
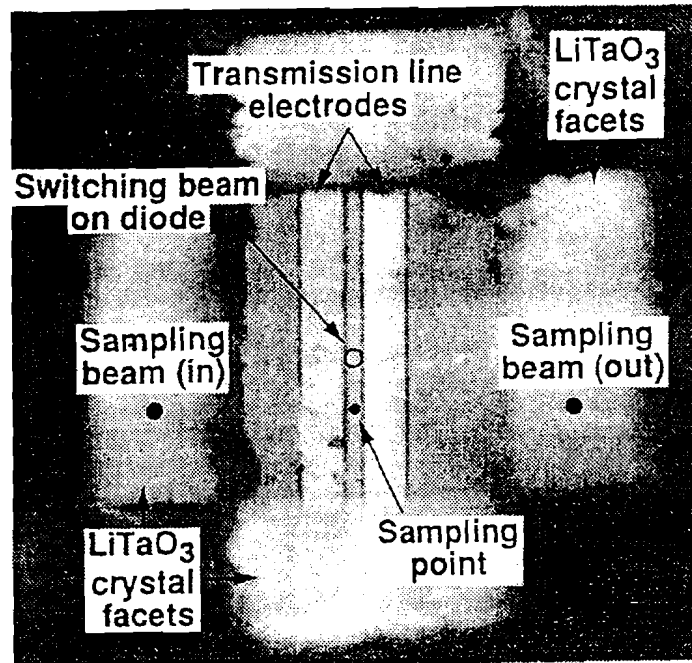
Fig. 2.7   A top view of the sampling geometry as illustrated in Fig. 2.7. The picture is taken through the $LiTaO_3$ crystal tip.

An alternative approach is to guide the sampling beam through the crystal in the total internal refection mode as seen in Fig. 2.6. This is achieved by cutting the crystal facets at an angle of ~30 degrees. The size of the crystal base is 1x1 mm^2 and its total thickness is ~2 mm. For the most part, the tip consist of fused silica, with a very thin 30 μm layer of $LiTaO_3$ at its edge [13]. The $LiTaO_3$ is initially glued on the fused silica support with UV cured optical adhesive and then thinned down and polished. It usually forms a front face with dimensions of ~150x200 $μm^2$ with the short side parallel to the optical axis. The crystal tip is supported by a pair of super-elastic optical fibers as shown in Fig. 2.6. A standard optical microscope, in conjunction with a long focal length objective, are used to align the crystal parallel to the substrate within a single fringe and ensure maximum sensitivity. In this geometry, the switching beam can be focused by the same microscope through the crystal tip to facilitate sampling measurements even at zero propagation distance[14]. A picture of such a set-up that was used to study the response characteristics of 5x5 $μm^2$ silicon MSM photodiodes [15] is shown in Fig. 2.7.
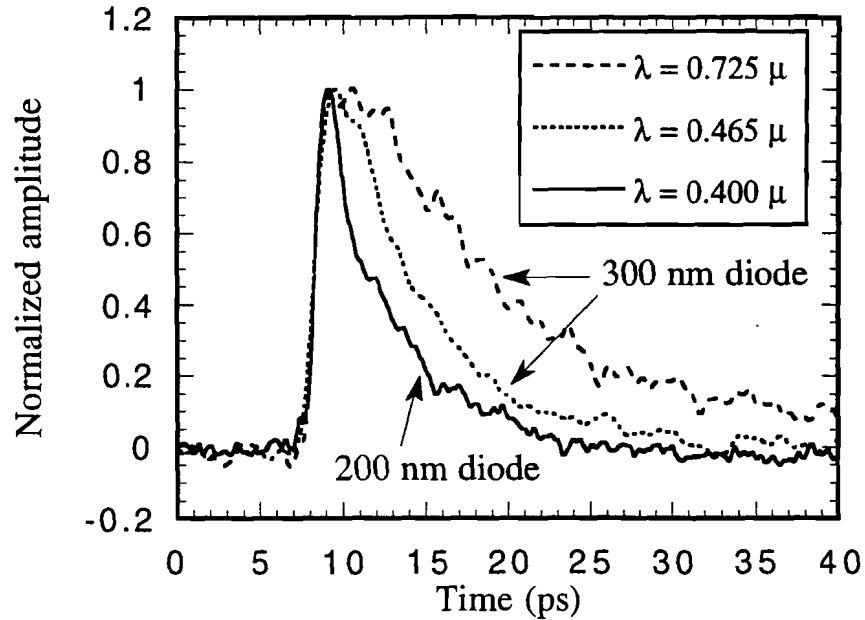
Fig. 2.8 Electrical responses of Si MSM photodiodes to a range of light wavelengths. The results correspond to diodes with a finger spacing of 200 and 300 nm. The electrical waveforms were sampled at the fundamental optical frequency of the Ti:Al$_2$O$_3$ laser when the diodes were excited at the second harmonic (0.465 and 0.400 μm).

Because the crystal is not coated, the wavelength of both the switching and sampling beams can be varied freely without any complications in the performance of the system. The electrical response of silicon photodiodes [16] was studied with this method at a range of wavelengths and representative results are shown in Fig. 2.8. These measurements demonstrate the first tunable, as well as frequency-doubled, electro-optic sampling system.

It has to be noted that until now, all measurements performed by external electro-optic sampling were limited to coplanar structures. Our ability to align the crystal parallel to the substrate within an optical wavelength, coupled with the enhanced sensitivity provided by the mixing set-up, enable us to make measurements even on low-impedance microstrip transmission lines [17],[18]. As can be seen in fig. 2.9, submillivolt sensitivity has been readily demonstrated.
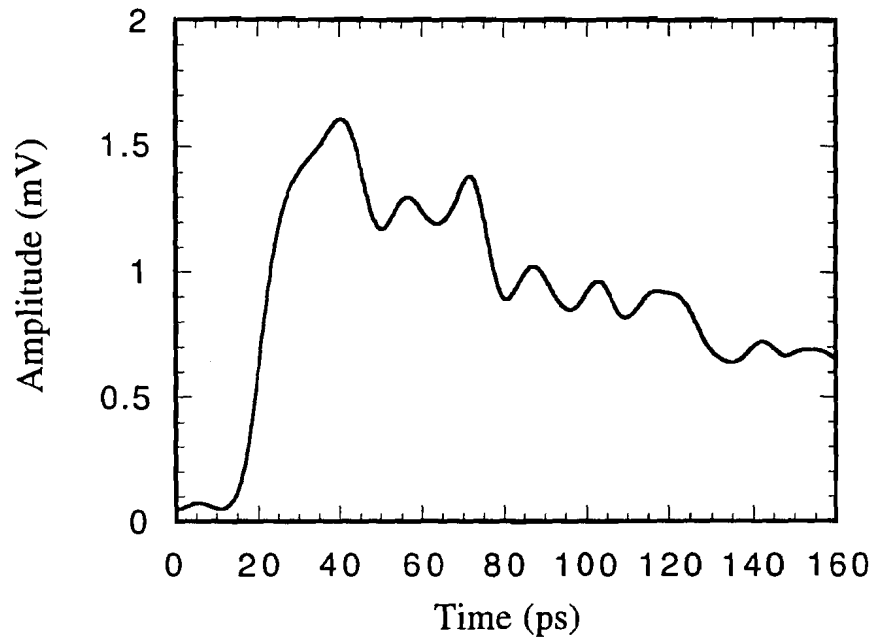
Fig. 2.9 An 1.5 mV electrical waveform measured on a microstrip transmission line

2.5 Temporal resolution

The temporal resolution of the system depends on the pulse width of the sampling beam (Δt_p), the transit time of the optical beam through the electro-optic crystal (Δt_o), and the averaging time over the span of the optical beam diameter (Δt_b). Of these three, the most important is Δt_p which has a value of ~140 fs for our Ti:Al$_2$O$_3$ laser. The upper bounds of Δt_o and Δt_b can be calculated from the following formulas,

$$\Delta t_o = 2\frac{d\, n_c}{c} \quad , \qquad \Delta t_b = \frac{r}{c}\sqrt{\frac{\varepsilon_c + \varepsilon_s}{2}} \qquad\qquad (2.5)\ ,\ (2.6)$$

where d is the thickness of LiTaO$_3$, n_c is its refractive index, c is the speed of light in vacuum, r is the optical beam diameter, and ε_c and ε_s are the dielectric constants of LiTaO$_3$ and the substrate, respectively. For a 30 μm thick LiTaO$_3$ crystal and a beam diameter of 5 μm, Δt_o is ~400 fs and Δt_p ~80 fs.
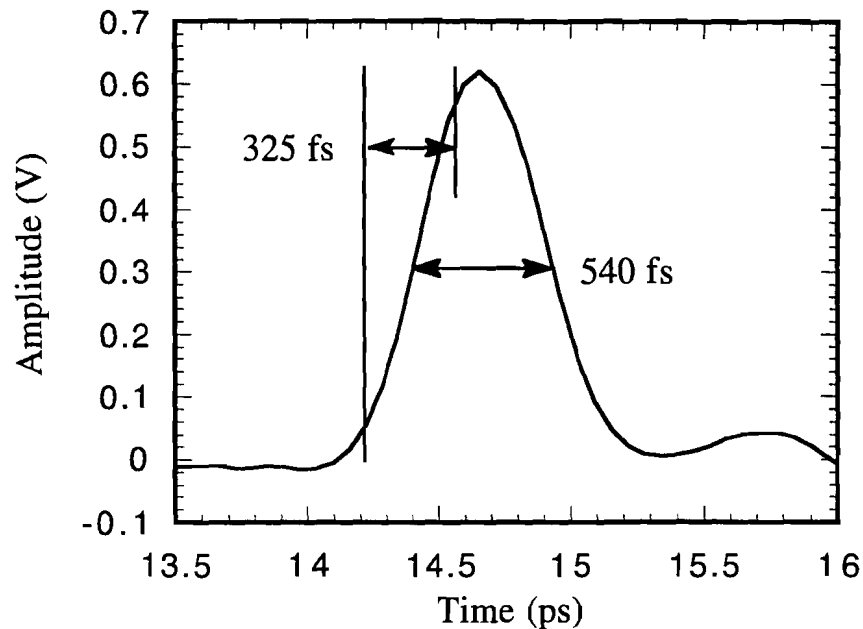
Fig. 2.10 An electrical waveform generated by the nonuniform illumination of a transmission line gap demonstrates the subpicosecond resolution of the electro-optic sampling system.

However, signal broadening due to Δt_O is usually much smaller because the electric field is much stronger at the surface of the crystal tip. In Fig. 2.9 we show one of the fastest signals we measured, an electrical waveform generated by the nonuniform illumination of a transmission line gap [19]. This waveform has a risetime of 325 fs and a full width at half maximum of 540 fs. Even finer temporal resolution (less than 200 fs) can be obtained with the use of narrower optical pulses [14].

2.6 Optical fiber

Measuring electrical signals with optical means offers the advantages of superior temporal resolution provided by the femtosecond laser pulses and precise time-scale calibration, controlled by the fine positioning of the optical delay line on a μm scale (see Fig 2.1). However, the very fact that real-space numbers are ultimately

converted into measuring time, can be a real problem in a situation where sequential measurements are required. Take for example, the case where a set of measurements are performed on a transmission line in order to estimate the signal propagation velocity in the manner indicated by Fig. 2.2. If the sampling beam and the crystal are moved to probe the signal at some distance further down the line, the relative time between the switching and sampling pulses is changed. A better option is to keep the crystal at a fixed position and move the whole sample. If we use an optical fiber to guide the switching beam on the sample, we ensure that timing is unperturbed and that the excitation is unchanged. In this manner, it is possible to do a sequence of measurements on the transmission line, and be able to describe its complete propagation function, as we shall see in Chapter 7.

Summary

In this chapter we gave a detailed description of our electro-optic sampler and addressed a set of design issues which during the span of this thesis research, have transformed the system from a demonstration unit to a solid instrumentation tool. In its current configuration, our system defines the state-of-the-art in almost every aspect. Among others, we have been able to demonstrate

- Best proven voltage sensitivity
- Temporal resolution less than 325 fs, and a bandwidth in excess of 1.5 THz
- Non-contact probing with feature size less than $(5 \ \mu m)^2$
- Frequency doubling and tunability both in the UV-blue and red-IR regions
- Sampling of non planar structures such as low impedance microstrips with μV sensitivity.

References

[1]   J. A. Valdmanis, "1-THz-bandwidth prober for high-speed devices and integrated circuits," *Electr. Lett.*, vol. 23, pp. 1308–1310, 1987.

[2]   J. A. Valdmanis and R. L. Fork, "Design considerations for a femtosecond pulse laser balancing self phase modulation, group velocity dispersion, saturable Absorption, and saturable gain," *IEEE JQE.*, vol QE-22, No. 1, pp. 112–118 January 1986.

[3]   Q. Fu, G. Mak, and H. M. van Driel, "High-power, 62-fs optical parametric oscillator synchronously pumped by a 76-MHz Ti:sapphire laser, *Opt. Lett.* vol. 17, pp. 1006-1008, July 1992.

[4]   B. Proctor and F. Wise, "Generation of 13-fs pulse from a mode-locked Ti:AL$_2$O$_3$ laser with reduced third-order dispersion," *Appl. Phys. Lett.*, vol. 62, pp.470–472, February 1993.

[5]   our autocorrelation measurement.

[6]   A. Yariv, "Optical waves in crystals," *Whiley & Sons*, New York, 1984.

[7]   J.M. Wiesenfield, "Electro-optic sampling of high speed devices and circuits," *IBM J. Res. Dev.*, vol. 34, No. 2/3, pp. 141-161, March/May 1990.

[8]   J. Son, J. V. Rudd, and J. F. Whitaker, "Noise characterization of a self mode locked Ti:sapphire laser," *Opt. Lett.*, vol. 17, pp. 733-735, May 1992. (Also verified by our independent measurements).

[9]   J. M. Chwalek, and D. R. Dykaar, "A mixer based electro-optic sampling system for submillivolt signal detection," *Rev. Sci. Instrum.*, vol. 61, no 4, pp. 1273-1276, April 1990.

[10]   B. H. Kolner and D. M. Bloom, "Electrooptic sampling in GaAs Integrated circuits," *IEEE JQE.*, vol. QE-22, No. 1, pp. 79-93, January 1986.

[11]   D. R. Dykaar, R. F. Kopf, U. D. Keil, E. J. Laskowski, and G. J. Zydzik, "Electro-optic sampling using an aluminum gallium arsenide probe," *Appl. Phys. Lett.*, vol. 62, pp.470–472, February 1993.

[12]   X. Tang, K. G. Irvine, D. Zhang, and M. G. Spencer, "Linear electro-optic effect in cubic silicon carbide," *Appl. Phys. Lett.*, vol. 59, pp.1938–1940, October 1992.

[13]   M. Y. Frankel, J. F. Whitaker, G. A. Mourou, and J. A. Valdmanis, "Experimental characterization of external electrooptic probes," *IEEE Microwave and Guided Wave Letters*, vol. 1, no. 3, pp. 60-63, Mar. 1991.

[14]   U. D. Keil and D. R. Dykaar, "Electro-optic sampling and carrier dynamics at zero propagation distance," *Appl. Phys. Lett.*, vol. 61, pp.1504–1506 ,1992.

[15]   S. Alexandrou, C.-C. Wang, T.Y. Hsiang, Y. Liu, and S.Y. Chou, "A 75 GHz silicon metal-semiconductor-metal Schottky photodiode," *Appl. Phys. Lett.*, vol. 62, pp. 2507-2509, May 17, 1993.

[16]   S. Alexandrou, C.-C. Wang, T.Y. Hsiang, Y. Liu, and S.Y. Chou, "3.7-ps silicon metal-semiconductor-metal Schottky photodiodes," *Conference on Lasers and Electro -Optics (CLEO)*, paper CTcC6, Baltimore, Maryland, 1993.

[17]   A. Denysenko, S. Alexandrou, C.-C. Wang, T. Hsiang, R. Sobolewski, W.R. Donaldson, and D.K. Bradley, "Picosecond characterization of x-ray microstrip channel plate detectors used in diagnosing inertial confinement fusion," to appear in *Rev. Sci. Instr.*

[18]   T. Y. Hsiang, C.-C. Wang, A. Denysenko, S. Alexandrou, R. Sobolewski, "An electro-optic sampling system for ultrafast testing of superconducting circuits," presented at the *International Superconducting Electronics Conference, Boulder* , Colorado 1993.

[19]   S. Alexandrou, C.-C. Wang, R. Sobolewski, and T.Y. Hsiang, "Generation of subpicosecond electrical pulses by nonuniform illumination of GaAs transmission line gaps," to appear in *IEEE J.Q.E.*

3. CPW Theory

The coplanar waveguide (CPW), together with coplanar strips (CPS) and the microstrip line (seen in Fig. 3.1), are the most common representatives of a family transmission lines known as open boundary waveguides. In these lines, the inhomogeneity of the dielectric interface between the substrate and the superstrate, prohibits TEM propagation. As a result, the main propagating mode has non-zero field components in the direction of propagation. At low frequencies, both loss and dispersion are limited and this mode is frequently called "quasi-TEM" because its propagation characteristics are similar to the TEM mode. On the other hand, at high frequencies the substrate modes (also known as surface waves) interact with the main CPW mode and as a result both dispersion and loss become considerable.

Coplanar waveguide   Coplanar strips

Microstrip
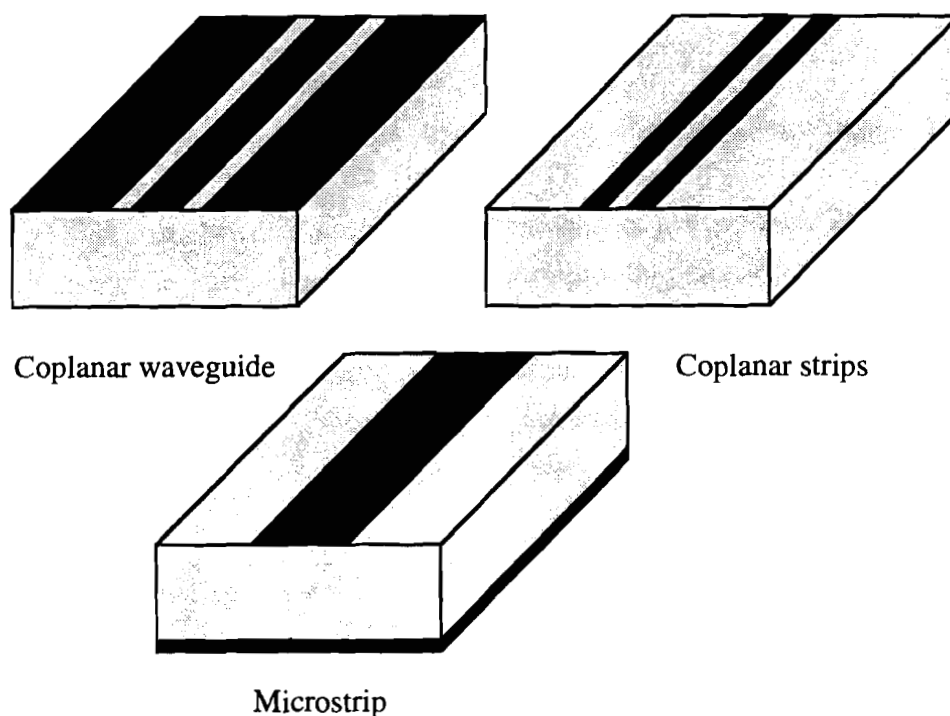
Fig. 3.1   The geometry of some open boundary waveguides. The black regions represent the metal conductors and the shaded areas the dielectric substrate.

All three lines seen in Fig. 3.1 exhibit similar propagation characteristics. The similarity is particularly strong between the CPW and the CPS since their structures are Babinet-complement (the areas covered by metal in the CPW are exposed to the dielectric substrate in the CPS). The coplanar lines have the advantage that their

impedance and lateral dimensions can be varied independently. They also offer convenient mounting of both series and shunt elements. The microstrip, on the other hand, frees substrate area since it uses the back side of the substrate for ground and has a higher current carrying capacity.

In this chapter we will concentrate on the CPW theory. The first section will focus on the quasistatic analysis, i.e. at frequencies low enough so that the characteristics of the line are insensitive to frequency. It will include the effect of different designs on the characteristic impedance and signal velocity. The following sections (2-4) will focus on high frequency behavior with special focus in the multi-gigahertz range. The role of dispersion and its relation to the substrate modes will be discussed in the second section, while the third is dedicated to the effects of attenuation with particular attention to radiation. Bends and other discontinuities are treated in section 4.

3. 1 Quasistatic analysis

The CPW [1] is a planar transmission line structure consisting of three metallic conductors placed on the same side of a dielectric substrate (Fig. 3.2). The center conductor, with width S, is separated from the two ground conductors by a distance W. In the ideal case, both the substrate thickness (h) and the width of the ground conductors are assumed to be infinite while the metal thickness (t) is taken to be zero but still sufficiently larger than the skin depth.
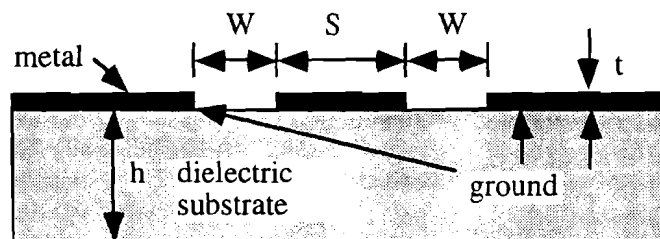
Fig 3.2   Transverse cross-section of a CPW transmission line.

There are a number of variations that can be made to the CPW design. The most common are: metalization of the back side of the substrate, reduction of the

ground conductor width to a size comparable to that of the center conductor, shielding of the entire CPW, and reduction of the substrate thickness. The effect of such parameters will be addressed in this section. Our discussion begins with the conformal transformation of a CPW transmission line on an infinitely thick substrate with semi-infinite ground planes [2], as shown in Fig. 3.2 (top).
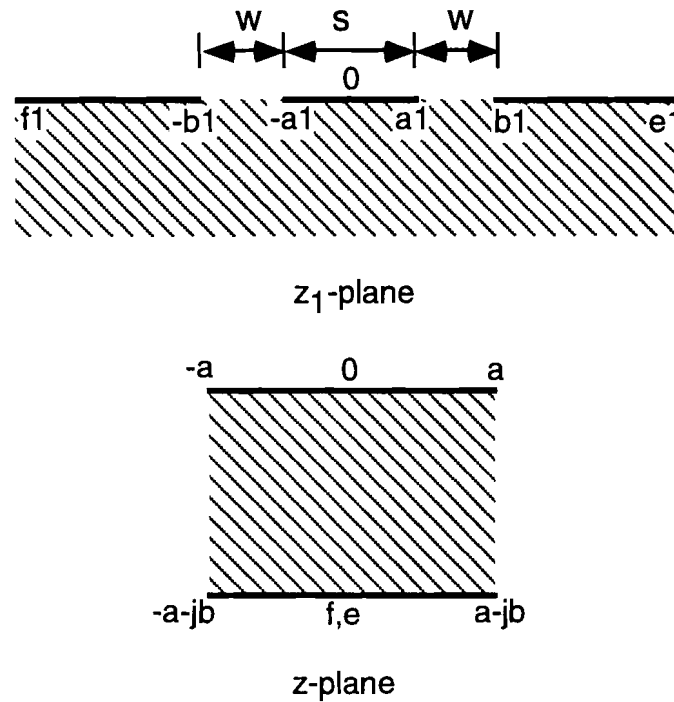
Fig. 3.3 Conformal transformation from a CPW in real space (z1-plane) to a rectangle in the z-plane.

In such a case, the dielectric half plane z_1 can be transformed to a rectangle in z-plane (Fig. 3.2), by the transformation

$$\frac{dz}{dz_1} = \frac{A}{\left(z_1^2 - a_1^2\right)^{\frac{1}{2}} \left(z_1^2 - b_1^2\right)^{\frac{1}{2}}} \qquad (3.1)$$

where A is a constant and $a/b = K(k)/ K'(k)$. $K(k)$ is the complete elliptic integral of the first kind and $K'(k) = K\left(\sqrt{1-k^2} \right)$ with $k = S/(S + 2W)$.

The top and bottom surfaces of the z-plane rectangle in Fig. 3.2 are conducting and form a capacitor which has a capacitance per unit length given by $C_d = \varepsilon_0\, \varepsilon_r\, 2a/b$. The total transmission line capacitance includes the contribution of the empty space half-plane and is given by $C = \varepsilon_0\, (\varepsilon_r+1)\, 2a/b$. In the quasi-static approximation, the phase velocity of the CPW is the average of the velocities of electromagnetic waves in air and the dielectric, and is given by

$$v_{ph} = c\sqrt{\frac{2}{\varepsilon_r+1}} = \frac{c}{\sqrt{\varepsilon_q}} \qquad (3.2)$$

where c is the speed of light in vacuum and ε_q is the quasistatic value of the effective dielectric permittivity. The characteristic impedance can be determined by the line capacitance and phase velocity as indicated by Eq. 3.3

$$Z_0 = \frac{1}{C\, v_{ph}} = \frac{30\pi}{\sqrt{\varepsilon_q}}\frac{K'(k)}{K(k)}\ [\Omega] \qquad (3.3)$$

The effect of finite ground plane width shows as a void in the dielectric half plane z (see Fig. 3.3) which decreases capacitance but increases impedance as indicated by Eq. 3.3. The phase velocity is also increased since additional field lines penetrate the back side of the substrate into the air. Table 3.1 , however, indicates that the changes in these parameters are only significant if the substrate thickness is comparable to the slot width W as long as $\varepsilon_r \gg 1$.

Parameter	Substrate thickness		
	Infinite	3W	W
v_{ph}	0.43	0.44	0.48
Z_0	51.4	52.4	57.7
energy in dielectric %	91	89	79

Table 3.1   The effect of substrate height on the properties a CPW with $\varepsilon_r = 10$ and $k = 0.5$, from Ref. 2.

The finite thickness of the metal conductors influences the characteristic impedance and phase velocity in a manner reciprocal to the substrate thickness. The

thicker the metal conductors get, the larger the capacitance and the higher the fraction of energy in air. As a result, the phase velocity is increased and the line impedance is decreased. In most applications, however, the conductor thickness (*t*) is much smaller than the line dimensions (*S+2W*) and its influence on the line parameters is minimal [3].

In the case where the back side of the substrate is covered by a conducting layer, the transmission line forms a microstrip-CPW hybrid [4]. If the substrate thickness is much bigger than *S+2W* the quasi-static characteristics of the CPW are only marginally affected. As the substrate thickness is reduced (*h~S+2W*), the line behaves more like a microstrip. The phase velocity increases and the line impedance becomes a strong function of *S* and *h* instead of *S* and *W*.

In real circuits, the ground plane width is limited by the finite dimensions of the substrate, but more importantly, by the density of active and passive devices. The effect of finite ground plane width was theoretically investigated by Gione and Naldi [5]. It was found that reducing the ground plane width to distances smaller than the center conductor width (*S*) could increase both phase velocity and line impedance significantly.

Sometimes the CPW is referred to as a coupled slotline pair. In this case, the separation (*W*) between the center and the two ground conductors is called the slot width. If the width of one slot is larger than the other then the line becomes an asymmetric CPW [6].

Of these variations in the CPW design discussed in this section, the reduction of the substrate height is the most important because it directly affects the CPW properties when *h* becomes comparable to the transverse dimensions of the line. The influence of the substrate height on both dispersion and loss will be addressed in the following sections.

3.2 Dispersion

In the previous section we gave a description of the CPW characteristics at low frequencies where the quasi TEM CPW mode is unaffected by the substrate modes. The reason is that in this frequency region, the phase velocities of the allowed TE and TM substrate modes are much larger than the phase velocity of the CPW

mode. As the frequency of operation is increased, however, the phase velocities of the substrate modes decrease monotonically and they eventually become smaller than the phase velocity of the quasi-TEM CPW mode [7, 8]. The CPW mode can interact with the substrate modes in a frequency neighborhood where their phase velocities are comparable. The influence of each substrate mode on the CPW mode depends on the degree of overlap between the field profiles of the two modes. This interaction affects the phase velocity of the quasi-TEM CPW mode and the line impedance through a change in the effective dielectric permittivity ($\varepsilon_{eff}(f)$). The value of $\varepsilon_{eff}(f)$ at each frequency can be calculated by detailed full-wave analysis which in turn can be approximated by Eq. 3.4 via curve fitting [9].

$$\sqrt{\varepsilon_{eff}(f)} = \sqrt{\varepsilon_q} + \frac{\sqrt{\varepsilon_r} - \sqrt{\varepsilon_q}}{\left(1 + a\left(\frac{f}{f_{te}}\right)^{-b}\right)} \qquad (3.4)$$

where f_{te} is the cut-off frequency of the first TE mode and is given by Eq. 3.5,

$$f_{te} = \frac{c}{4h\sqrt{\varepsilon_r - 1}} \qquad (3.5)$$

while a and b are empirical parameters [9]. The value of b (~ 1.8) is independent of geometry but a depends on the line dimensions as expressed by Eq. 3.6

$$\log(a) = u \log\left(\frac{S}{W}\right) + v \qquad (3.6)$$

where $u \sim 0.54 - 0.64\, q + 0.015\, q^2$ $\qquad (3.7)$

$v \sim 0.43 - 0.86\, q + 0.54\, q^2$ $\qquad (3.8)$

and $q = \log\left(\frac{S}{h}\right)$ $\qquad (3.9)$

The values of line impedance and phase velocity at all frequencies can still be expressed by Eq. 3.2 and 3.3 if the static value of the dielectric permittivity ε_q is replaced by $\varepsilon_{eff}(f)$. More elaborate formulas for Z_o that include variations due to the conductor width and substrate height can be found in [2,10].

The influence of the substrate modes on the value of $\varepsilon_{eff}(f)$ is shown in Fig. 3.4 as a function of frequency. For low frequencies, $\varepsilon_{eff}(f)= \varepsilon_q$ and is unaffected by the CPW geometry, as long as the substrate thickness $h >> S+ 2W$. The line dimensions, however, have a strong effect on the value of $\varepsilon_{eff}(f)$ at frequencies around the substrate cut-off. For small line dimensions, the quasi-TEM CPW mode is confined close to the surface of the substrate and its field-overlap with the substrate modes is diminished. As a result, the effective dielectric permittivity does not deviate from the quasi-static value even at frequencies much higher than f_{te}.
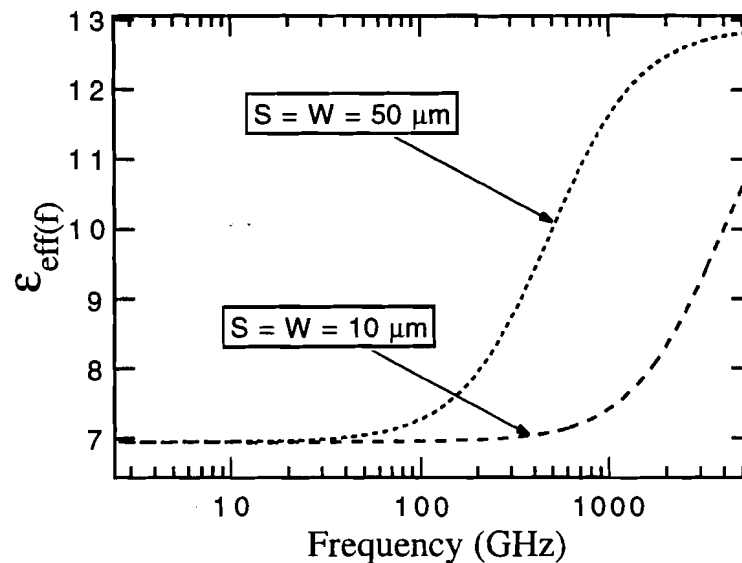
Fig. 3.4   Effective dielectric permittivity as a function of frequency for CPWs with different line dimensions (but same quasi-static impedance) on GaAs substrate with thickens h = 500 μm and ε_r = 12.9.

Changes in the value of $\varepsilon_{eff}(f)$ are very important because they are ultimately translated into modal dispersion [7, 8, 11] which distorts any signal propagating on the transmission line. Modal dispersion can be minimized by reducing the CPW lateral dimensions which limit the field-overlap with the substrate modes, or by reducing the thickness of the substrate which directly increases its cut-off frequency. A selection of a substrate with low dielectric constant has a similar effect.

Dispersion can also arise from the finite resistance of the metal conductors and the conductance of the substrate even at low frequencies, but such contributions are usually small compared to modal dispersion [12]. The complex impedance of the

metal conductors can also introduce dispersive effects but its contribution is only important for superconducting lines [13], or lines with very small lateral dimensions [14].

3.3 Attenuation

There are mainly three different mechanisms through which the signal propagated on a CPW suffers attenuation: dielectric loss, conductor loss, and radiation. Radiation is more important at high frequencies while conductor loss dominates the low-frequency regime. The dielectric loss is given by [7]

$$\alpha_d = 27.3 \ \frac{\varepsilon_r}{\sqrt{\varepsilon_q}} \ \frac{\varepsilon_q - 1}{\varepsilon_r - 1} \ \frac{\tan \delta}{\lambda o} \quad \left(mm^{-1} \right) \tag{3.10}$$

where λo is the wavelength in free space in millimeters, and $tan \ \delta$ is given by [12]

$$\tan \delta = \frac{\omega \varepsilon'' + \sigma}{\omega \varepsilon'} \tag{3.11}$$

where ω is the angular frequency, σ is the substrate conductivity, and ε' and ε'' are the real and imaginary parts of the substrates dielectric permittivity, respectively. In practical circuits, the substrate is chosen such that its dielectric relaxations occur at frequencies much higher than the operational bandwidth. This is readily achievable with semiconductor substrates, which have resonances in the range of several terahertz. In the absence of resonances, ε'' is very small and $tan \ \delta$ tends to zero as long as conductivity is kept low (by avoiding high doping). Under these conditions dielectric loss is very small compared to conductor loss and radiation and can be neglected [7, 15].

The finite surface resistance ($Rs(f)$) of the metal electrodes is responsible for the conductor loss given by Eq. 3.12 [2]. For this reason, the loss increases as the line dimensions get smaller (example shown in Fig. 3.5). Moreover, since $Rs(f)$ is directly related to the skin effect, the conductor loss has a square root frequency dependence as shown in the figure.

$$\alpha_c = \left(4.88 \ 10^{-4}\right) Rs(f) \ \varepsilon_{eff}(f) \ Z_0 \frac{P'}{\pi \ W}\left(1 + \frac{S}{W}\right)\Omega \quad \left(\frac{dB}{mm}\right) \qquad (3.12 \ a)$$

$$\text{with} \quad P' = g_1^2 \ k \left\{\left(1 - \sqrt{1-k^2}\right)\left(1-k^2\right)^{3/4}\right\}^{-1} \qquad (3.12 \ b)$$

$$\text{where} \quad g_1 = \frac{K(k)}{K'(k)} \qquad (3.12 \ c)$$

$$\text{and} \quad \Omega = \left\{\frac{\frac{1.25}{\pi} \ln\left(\frac{4\pi S}{t}\right) + 1 + \frac{1.25 \ t}{\pi \ S}}{\left[2 + \frac{S}{W} - \frac{1.25 \ t}{\pi \ W}\left(1 + \ln\left(\frac{4\pi S}{t}\right)\right)\right]^2}\right\} \qquad (3.12 \ d)$$
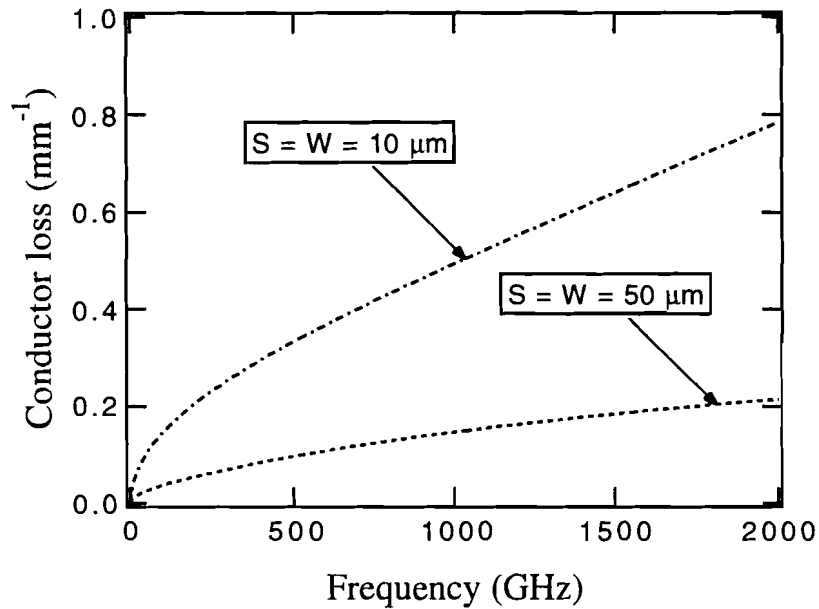
Fig. 3. 5   The conductor loss as a function of frequency for two CPWs on a dielectric substrate with $\varepsilon_r = 12.9$.

The coupling between the quasi-TEM CPW mode and the substrate modes is not only responsible for modal dispersion but for radiation as well. At frequencies

where the phase velocity of the CPW mode is higher than the phase velocity of the substrate modes, mode coupling forces energy to radiate from the transmission line at an angle Ψ given by Rutledge *et al* [16]

$$\cos\left(\Psi\right) = \frac{k_w}{k_s} = \sqrt{\frac{\varepsilon_{eff}(f)}{\varepsilon_r}} \qquad (3.13)$$

where k_w and k_s are the propagation constants of the guided CPW mode and the substrate modes, respectively. The radiation emitted from the transmission line is given by

$$\alpha_r = \left(\frac{\pi}{2}\right)^5 \frac{\left(1 - \frac{\varepsilon_{eff}(f)}{\varepsilon_r}\right)^2}{\sqrt{\frac{\varepsilon_{eff}(f)}{\varepsilon_r}}} \frac{(S + 2W)^2 \varepsilon_r^{1.5}}{c^3 K(k) K'(k)} f^3 \left(mm^{-1}\right) \qquad (3.14)$$
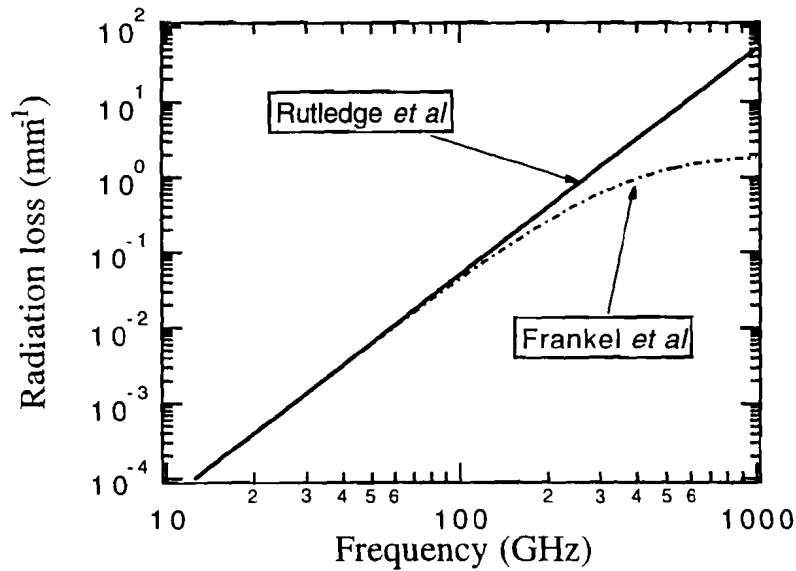
Fig. 3.6a Radiation loss as function of frequency according to Rutledge [16], and Frankel [17], for a CPW with $S = W = 50\ \mu m$ on a $500\ \mu m$ thick substrate with $\varepsilon r = 12.9$.

The formula for the frequency dependence of radiation (Eq. 3.14) was empirically modified by Frankel at al [17] to take into account the effect of the radiation angle Ψ. According to these authors the angle Ψ reduces the rate of increase
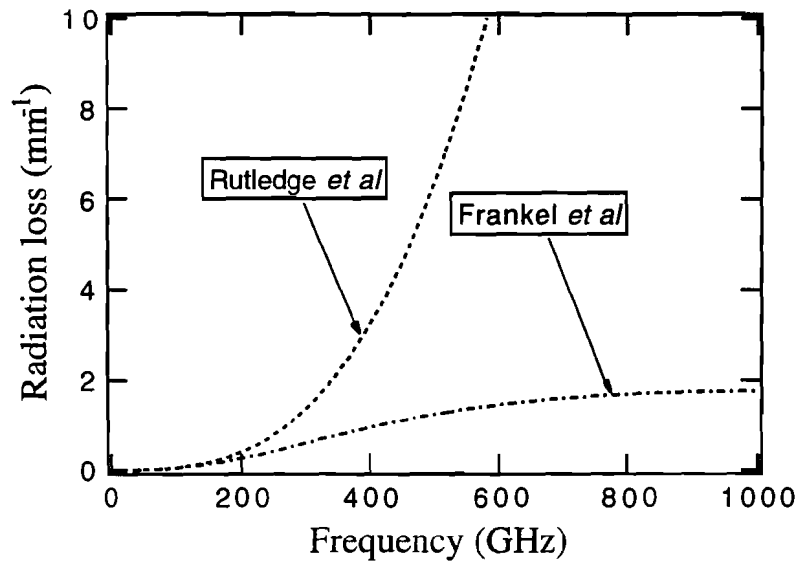
Fig. 3.6b   Same as in Fig. 3.6a but on a linear scale
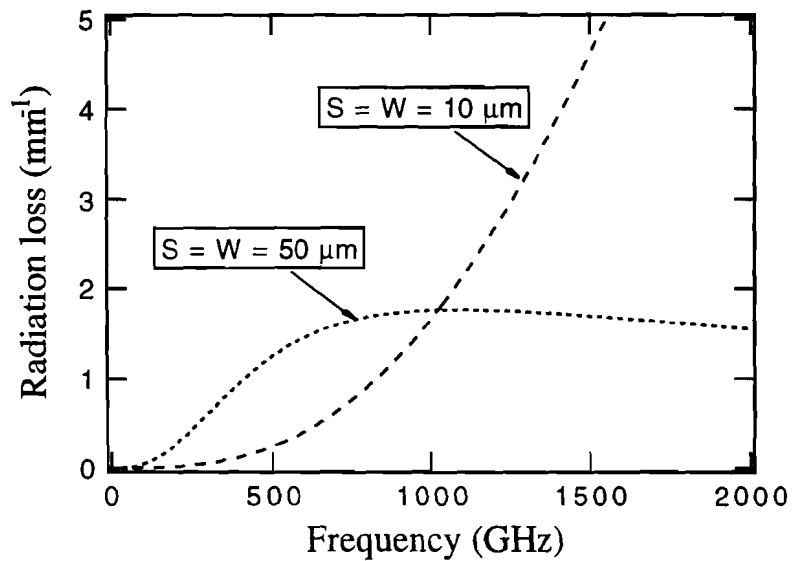
Fig. 3.7   The effect of the transmission line lateral dimensions on radiation loss for transmission lines on a 500 µm thick substrate with $\varepsilon r = 12.9$ according to Eq. 3.14.

of radiation loss below the f^3 dependence at high frequencies. As shown in Fig. 3.6, this effect can be dramatic at frequencies above the substrates cut-off.

As indicated by Eq. 3.14, transmission lines with larger lateral dimensions suffer greater radiation losses. In Fig. 3.7, where the radiation loss for 10 and 50 μm CPWs is compared, we see that the 10 μm lines are significantly superior for frequencies up to a terahertz. For even higher frequencies, the 50 μm lines suffer reduced loss because of the increase in the effective dielectric permittivity, but the validity of this result is questionable since Eq. 3.14 is valid only for wavelengths where $\lambda > S + 2W$ [17].
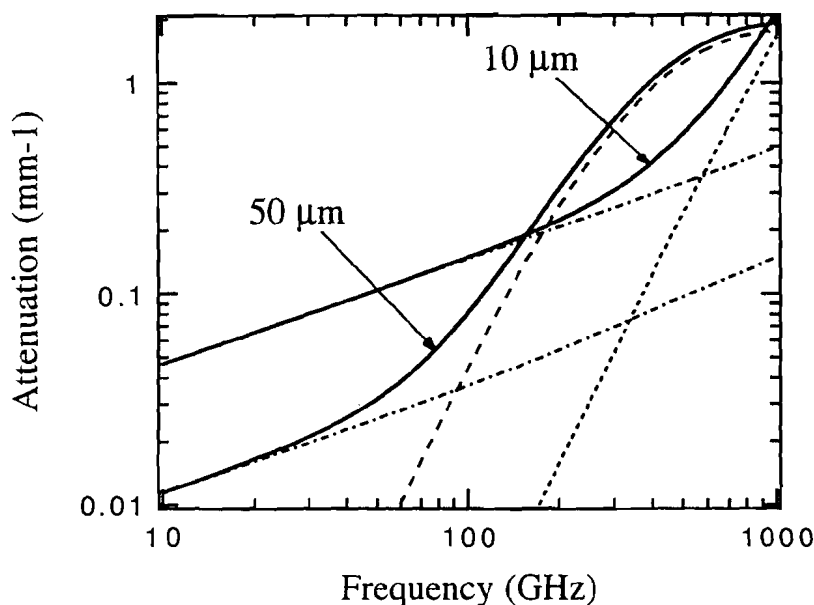
Fig. 3.8   Attenuation as a function of frequency for CPWs on a 500 μm thick substrate with $\varepsilon_r = 12.9$. The solid lines indicate the total loss for each line, while fine dotted lines show conductor loss and the coarse dotted lines radiation.

As we have just seen, radiation loss can be reduced by minimizing the lateral dimensions of the transmission line, but this inevitably leads to an increase of the conductor loss. In Fig. 3.8 we plot the radiation, conductor, and total losses for a pair of CPWs with different dimensions. For the 10 μm line, the total loss is dominated by conductor losses up to a frequency of 300 GHz but for the 50 μm lines, radiation is dominant for frequencies as low as 50 GHz. It is important to note that for low frequencies the 50-μm CPW is less lossy, but for higher frequencies the 10-μm line

becomes a better choice. Thus, depending on the particular frequency of operation, the lateral dimensions of the CPW can be engineered so that total loss is minimized. In contrast to the microstrip, this optimization can be readily carried out in CPWs without affecting the characteristic impedance of the line.

Radiation losses can also be lessened by a reduction of the ground plane width [18], which leads to reduced overlap between the substrate modes and the quasi-TEM CPW mode. Minimal mode overlap reduces dispersion as well. A study of CPS surrounded by a ground plane [19], which is the complementary structure of a CPW with finite grounds, also revealed that such a structure suffers reduced dispersion.

All losses in CPWs: dielectric, conductor, or radiation, depend on the dielectric properties of the substrate. In general, one can safely argue that a substrate with low dielectric constant is preferable. For high frequency applications, such as high speed monolithic microwave integrated circuits (MMICs) where this research is most relevant, semiconductors are the substrate of choice. Most semiconductors have an ε_r on the order of 10, much higher than air. The effective dielectric constant of a transmission line on a semiconductor substrate can be significantly lowered, however, by edging a part of the substrate between the electrodes [14]. This not only reduces all losses, but also increases the phase velocity and limits dispersion.

3.4 Discontinuities

Transmission line discontinuities, such as bends, T-junctions, dividers, open- and short-circuit ends to name a few, appear in almost all practical circuits. Most of the work involving the characterization of discontinuities was focused on microstrip elements and only at frequencies of few GHz [20-23]. From the limited work involving CPW elements [24-26], and the analogies that can be brought from the microstrip results, it seems that both reflections and losses increase with frequency. Thus, as the frequency of operation of microwave circuits approaches the subterahertz range, the characterization of discontinuities becomes more important. It has been suggested that increased coupling between the CPW mode the TM substrate modes at discontinuities leads to increased losses [26]. In straight lines coupling to the TM modes is weak because the electric field profile of the CPW mode is transverse.

Discontinuities also lead to another problem that is specific to CPWs. This transmission line is a three conductor system and as a result it can support two spatial modes of propagation. The analysis presented in this chapter refers to the preferred quasi-TEM CPW mode which is also known as the odd mode since its field profile is symmetric with respect to the center conductor (see Fig. 3.9). Alternatively, when the transverse electric field distribution in the line is antisymmetric, we have the much inferior even mode, which exhibits characteristics similar to a slotline with a slot width equal to $S+2W$. At some discontinuities, such as dividers and bends, the unwanted even mode is excited [27], and as a result the propagating signal suffers the increased loss and dispersion associated with this mode.

(a)   (b)
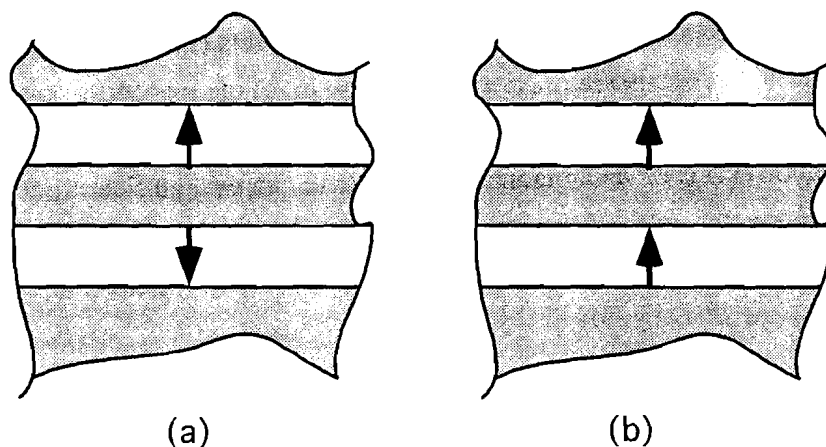
Fig. 3.9   (a) The odd CPW mode with both electric field vectors pointing away from the center conductor, and (b) the even mode with the electric field vectors pointing to the same direction.

As an example, let us consider the case of a transmission line bend shown in Fig. 3.10. The CPW is a symmetric structure but once a bend is introduced in the line its symmetry is broken. Inside a bend the signal has to travel a longer distance in the top slotline than the bottom one. Thus, the electrical transient emerging from this bend can not be symmetric, otherwise the propagation speed in the two slotlines would have to be different. This asymmetry leads to the separation of the transient into odd and even CPW modes. The even mode can be eliminated by airbridges (wirebonds) which connect the two grounds at discontinuities [24,28], or by a

dielectric overlay atop the short slot to much the delay between the signals in the two slots [24].

(a)   (b)
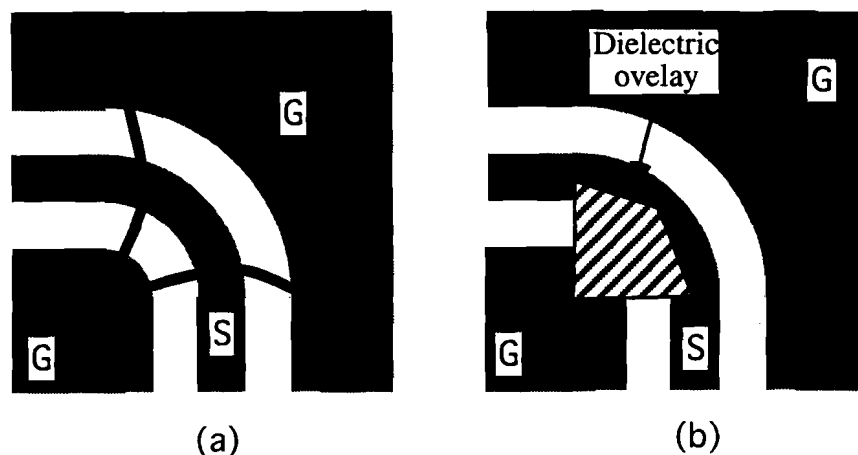
Fig. 3.10   The CPW even mode can be suppressed by airbridges (a), or by a dielectric overlay to delay the signal in the shorter slot (b)

Of these two methods the use of airbridges is more practical since they can easily be implemented by wirebonding. Dielectric overlays address the problem on a more fundamental level, but they can not be used at T-junctions or dividers and their implementation requires extra fabrication steps. At low frequencies, wirebonds can successfully prevent the excitation of the even mode because their inductance is low compared to the even mode impedance. However, their effectiveness in the subterahertz regime is a matter of debate since their inductance would increase dramatically at such frequencies.

Summary

This chapter focused on the theoretical aspects of CPW design. Starting from the conformal transformation, we described the parameters that influence characteristic impedance and phase velocity. The substrate modes and their influence on both attenuation and dispersion were also addressed, together with the role of discontinuities at subterahertz frequencies. It is important to remember that in this

frequency regime, the behavior of the transmission line is governed by the following parameters:

- Effective dielectric permittivity whose increase at high frequencies causes a reduction in both the phase velocity and Z_0.

- Modal dispersion which arises from the change in $\varepsilon_{eff}(f)$ and dominates dispersion.

- Radiation induced by the coupling of the CPW mode to the substrate modes and dominates losses.

- The even mode that is excited at discontinuities and degrades the performance of the transmission line.

References

[1] C.P. Wen, "Coplanar waveguide: A surface strip transmission line suitable for nonreciprocal gyromagnetic device applications," *IEEE MTT.*, vol. 17, No. 12, pp. 1087-1090, December 1969.

[2] K. C. Gupta, R. Garg, and I. J. Bahl, "Microstrip lines and slotlines," Norwood, MA, *Artech House*, 1979.

[3] T. Kitazawa, and T. Itoh, "Propagation characteristics of coplanar-type transmission lines with lossy media," *IEEE MTT.*, vol. 39, No. 10, pp. 1694–1700, October 1991.

[4] Y. C. Shih, and T,. Itoh, "Analysis of conductor backed coplanar waveguide," *Electron. Lett.*, vol. 18, No. 12, pp. 538-540, June 1982

[5] G. Goine and C. U. Naldi, "Coplanar waveguide for MMIC applications: effect of upper shielding, conductor backing, finite-extent ground planes, and line-to-line coupling," *IEEE MTT*, vol. 35, No. 3, pp. 260-267, March 1987.

[6] M. Kitlinski, and B. Janiczak, " Dispersion characteristics of asymmetric coupled slotlines on dielectric substrates," *Electron. Lett.* vol. 19, No. 3, pp. 91-92, February 1983.

[7] D. S. Phatak, N. K. Das, and A. P. Defonzo, "Dispersion characteristics of optically excited coplanar striplines: comprehensive full wave analysis," *IEEE MTT.*, vol. 38, No. 11, pp. 1719–1730, November 1990.
Also, D. S. Phatak, and A. P. Defonzo, "Dispersion characteristics of optically excited coplanar striplines: Pulse Propagation," *IEEE MTT.*, vol. 38, No. 5, pp. 654–661, May 1990.

[8] M. Riaziat, R. Majidi-Ahi, and I.-J. Feng, "Propagation modes and dispersion characteristics of coplanar waveguides," *IEEE MTT.*, vol. 38, No. 3, pp. 245–251, March 1990.

[9] G. Hasnain, A. Dienes, and J. R. Whinnery, "Dispersion of picosecond pulses in coplanar transmission lines," *IEEE MTT.*, vol. 34, No. 6, pp. 738-74, June 1986.

[10] B. C. Wadell, " Transmission line design handbook," Norwood, MA, *Artech House*, 1991.

[11]   J. F. Whitaker, R. Sobolewski, D. R. Dykaar, T. Y. Hsiang, and G. A. Mourou, "Propagation model for ultrafast signals on superconducting dispersive lines," *IEEE MTT.*, vol. 36, pp. 227–285, February 1988

[12]   J. F. Whitaker, "Ultrafast electrical signals: transmission on broadband guiding structures and transport in the resonant tunneling diode," Doctoral thesis, University of Rochester, Rochester, 1988.

[13]   S. Gupta, J. F. Whitaker, and G. A. Mourou, "Subpicosecond pulse propagation on coplanar waveguides: experiment and simulation," *IEEE Microwave and Guided Wave Letters*, vol. 1, No. 7, pp. 161-163, July 1991.

[14]   U. D. Keil, D. R. Dykaar, A. F. J. Levi, L. N. Pfieffer, S. B. Darack, and K. W. West, "High speed transmission lines," *IEEE J.Q.E.*, (Special issue on ultrafast electronics and optoelectronics), vol. 28, No. 10 , pp. 2333-2342, October 1992.

[15]   C. Shu, X. Wu, E. S. Yang, X.-C. Zhang, and D. H. Auston, "Propagation characteristics of picosecond electrical pulses on a periodically loaded coplanar waveguide," *IEEE MTT.*, vol. 39, No. 6, pp. 930-935, June 1991.

[16]   D. S. Rutledge, D. P. Neikirk, and D. P. Kasilingham, "Infrared and millimeter waves," vol. 10 , chapter 2, K. J. Buttton, Ed. New York: *Academic press,* 1983.
        Also, D. P. Kasilingham and D. B. Rutledge, " Surface wave losses of coplanar transmission lines," *IEEE Int. Sump. Digest*, pp. 113–116, 1983.

[17]   M. Y. Frankel, S. Gupta, J. A. Valdmanis, and G. A. Mourou, "Terahertz attenuation and dispersion of coplanar transmission lines," *IEEE MTT.*, vol. 39, No. 6, pp. 910-916, June 1991.

[18]   M. Tsuji, H. Shigesawa, and A. A. Oliner, "New coplanar leakage behavior on coplanar waveguides of finite and infinite widths," *IEEE MTT.*,, vol. 39, No. 12, pp. 2130-2237, December 1991.

[19]   J.S. McLean and T. Itoh, "Analysis of a new configuration of coplanar stripline," *IEEE MTT.*,, vol. 40, No. 4, pp. 772-774, April 1992.

[20]   W. P. Harokopus, and L. P. B. Katehi, "Electromagnetic coupling and radiation loss considerations in microstrip (M)MIC design," *IEEE MTT.*, vol. 39, No. 3, pp. 413-421, March 1991.

[21]   T.-S. Horng, W. E. McKinzie, and N. G. Alexopoulos, "Full wave spectral domain analysis of compensation of microstrip discontinuities using triangular

subdomain functions," *IEEE MTT.*, vol. 40, No. 12, pp. 2137-2147, December 1992.

[22]   A. Weisshaar, and V. K. Tripathi, "Perturbation analysis and modeling of curved microstrip bends," *IEEE MTT.*, vol. 38, No. 10, pp. 1449-1454, October 1990.

[23]   J. S. Roy, D. R. Poddar, A. Mukherjee, and S. K. Chowdhury, "Dispersion characteristics of curved microstrip lines," *IEEE MTT.*, vol. 38, No. 8, pp. 1366-1370, August 1990.

[24]   R. N. Simonns, G. E. Ponchak, K. S. Martzaklis, and R. R. Romanofsky, "Channelized coplanar waveguide; discontinuities, junctions, and propagation characteristics," *IEEE Int. Sump. Digest*, pp. 915–918, 1989.
Also, R. N. Simonns and G. E. Ponchak, "Modeling of some coplanar waveguide discontinuities," *IEEE MTT.*, vol. 36, No. 1796-1803, December 1988.

[25]   M. Naghed, and I. Wolff, "Equivalent capacitances of coplanar waveguide discontinuities and interdigitated capacitors using a tree-dimensional finite difference method," *IEEE MTT.*, vol. 48, No. 12, pp. 1808-1815, December 1990.

[26]   J. S. Mclean, A. D. Wieck, K. Ploog, and T. Itoh, "Fullwave analysis of open-end discontinuities in coplanar stripline and finite ground coplanar waveguide in open environments using a deterministic spectral domain approach," *21st European microwave conference proceedings*, Stuttgart, Germany, 1991.

[27]   T. Itoh, "Planar Transmission Line Structures", *IEEE Press*, p. 253, 1987.

[28]   R. Majiti-Ahi, C. K. Nishimoto, M. Riaziat, M. Glen, S. Silverman, S. Weng, Y. Pao, G. A. Zdasiuk, S. G. Bandy, and Z. C. H. Tan, "5-100 GHz InP coplanar waveguide MMIC distributed amplifier," *IEEE MTT.*, vol. 38, No. 12, pp. 1986–1992, Dec. 1990.

4. Sample fabrication and the photoconductive switch

In the last chapter we presented an overview of the CPW behavior with an emphasis on its ultrafast characteristics. Our formalism dependent primarily on theoretical analysis, and to a less extent on the experimental results, presented through the years by a number of researchers.

This chapter describes the logistics through which the experimental results presented in this thesis (chapters 5-7) were obtained. It is divided into two parts: A and B. Part A (sections 1 to 3) gives a description of the tested samples, and part B (sections 4 to 8) focuses on the various methods terahertz signals can be generated and subsequently be launched into such transmission lines.

More specifically, the first section focuses on the fabrication of the transmission lines. Two separate sets of samples that were fabricated with two different masks. Section 2 describes the layout of the first mask that was used to fabricate the samples whose characterization is presented in chapter 5. Section 3 concentrates on the features of the second mask which provided the samples for the pulse measurements in chapters 6 and 7.

Part B starts with a brief introduction on the principle of operation of photoconductive switches (section 4). Drift based switches in the recombination limit are described in the section 5, and in the transit time limit in section 6. The generation of electrical pulses by screening effects is presented in section 7. The last section (8) discusses the merits of the various pulse generation schemes and their compatibility to the transmission lines we want to test.

PART A
4.1 Fabrication

All samples were fabricated on semi-insulating GaAs wafers with a two inch diameter and a thickness of 500 μm. The substrate was not intentionally doped and it had a high resistivity of more than 10^7 Ω.cm. The mobility was ~5000 cm²/v.s and the substrate's orientation was (100). Some samples were also fabricated on intrinsic and doped Si, but for reasons that are beyond the scope of this research. All the results presented in this thesis were taken from samples fabricated on GaAs.

(i)

(iv)

(ii)

(v)

(iii)

(vi)
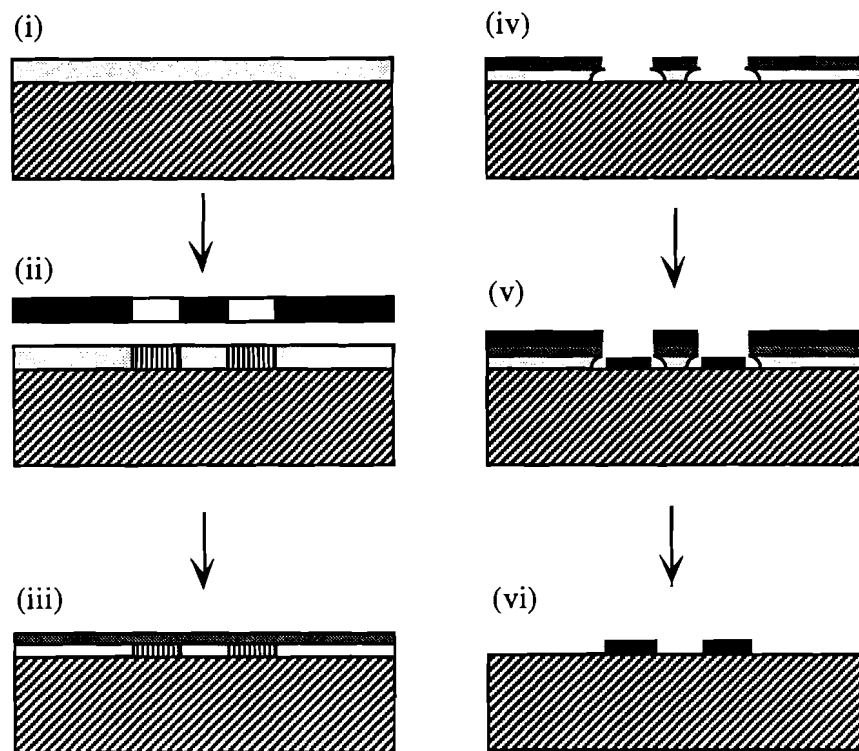
Fig. 4.1   The fabrication steps for the patterning of Gold transmission lines on GaAs using a lift-off process. See text for details

The transmission lines were fabricated with a "lift-off" process in the sequence shown in Fig. 4.1. Initially the GaAs wafers are edged in a buffer-oxide-edge solution to remove the thin oxide layer from the substrates surface. They were then coated with a 1.3 μm layer of positive photoresist as shown in diagram (i). After pre-baking and cool-down, the transmission lines were photolithographically

patterned on the wafers using a negative mask (diagram (ii)). Post-baking was avoided to prevent hardening of the photoresist. The samples were instead submersed into chlorobenzene which penetrates the top photoresist layer as indicated in the next diagram, and increases its resistance to developers. As a result when the photoresist is developed (actually over-developed) we observe the "overhanging" profile shown in diagram (iv). Subsequent gold evaporation results in islands on the substrates surface which are completely isolated from the rest of the metal film. Consequently, when the wafers are soaked in acetone, most of the metal film is washed away with the dissolved photoresist. What is left, is the island regions that are in direct contact with the substrate, and form the transmission line patterns, as shown in Fig. 4.1 (vi).

The contact of the metal lines on the substrate in improved by thermal annealing in inert argon atmosphere at a relatively low temperature (~350 ^{0}c for 20 minutes) to avoid diffusion of Au into the semiconductor. The thickness of the metal film (~1/4 μm) is coarsely monitored during growth, but it is subsequently verified on a subnanometer level with an Alpha stepper. It is preferable that the metal thickness is larger than the skin depth over the bandwidth of interest to minimize losses. Moreover, once the film thickness is known, its resistivity, which is a measure of film quality, can be extracted from four-probe measurements. For example, the samples fabricated with mask 2, had an as grown resistivity of 2.5 x 10^{-6} Ω.cm which increased to 3 x 10^{-6} Ω.cm after annealing.

After patterning, the wafers are diced and each unit cell is mounted on a sample holder to facilitate sampling measurements. The top surface was completely open to provide easy access for excitation and probing. Contacts for biasing and terminations are provided by wirebond connections.

4.2 The first mask.

The first mask was designed by Hiroyoki Nakano, a classmate and project partner of the author during their first year of study. Its purpose was to study the effect of bends in the propagation characteristics of CPW transmission lines. The main features of the transmission lines are shown in Fig. 4.2. The CPWs had a meander-like structure, so that the cumulative distortion of the signal propagated along many bends could be measured.

One set of CPWs was about 10-mm long and incorporated 20 bends over this distance as shown in the figure. The other set of lines, not shown in Fig. 4.2, had a length of ~6mm and a total of 12 bends over their length. Straight CPWs of the same dimensions were also included in the same cell for comparison. All lines had a 20 μm gap in the center conductor which formed a photoconductive switch in series with the transmission line, as indicated in diagram (a) of Fig. 4.2. The edges of the switch were tapered at 45^0 to reduce its capacitance. Seven bent CPW designs with different degree of bend smoothing were incorporated in the mask. Figure 4.2 presents only the extreme cases and shows the right-angle-bent line (b), and the lines with the bends smoothed by curving (c), or chamfering(d).
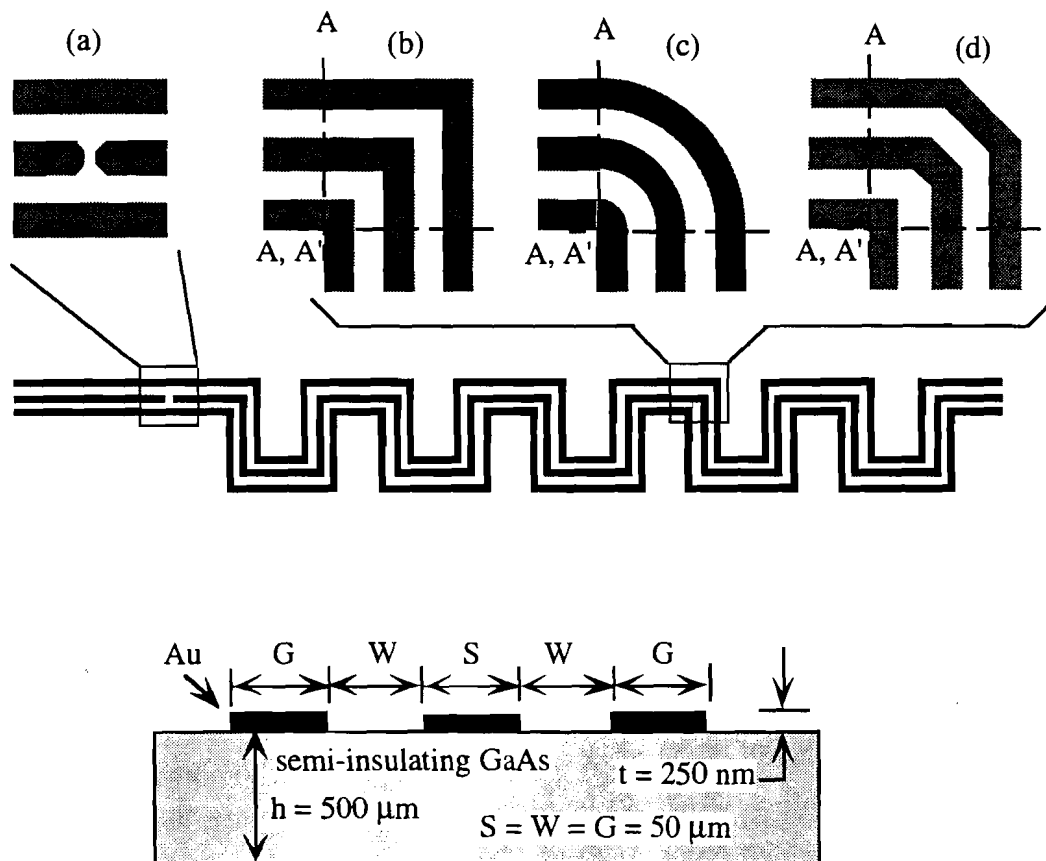
Fig. 4.2   The geometry of the CPWs fabricated with the first mask. The upper part of the figure shows the top view and the lower the line cross-section.

The mask's unit cell was relatively large with an area of 10.6x15.4 mm^2, and included a total of 16 transmission lines at two different lengths. Fourteen CPWs

were bent and two were straight. The 4-inch mask included 16 cells covering an area large enough to expose a 3-inch wafer.

The lateral dimensions of the transmission lines are shown in the lower diagram of Fig. 4.2. It is important to note that the width of the ground conductors is only 50 μm, the same as the center conductor. The finite width of the ground conductors increases the characteristic impedance from 58 to 64 Ω according to Gione and Naldi [1]. For the same reason, the quasi-static phase velocity is also increased, but only by a factor of 0.01.

The main purpose of the first mask was to address some fundamental questions about signal propagation through bent structures. For instance, what would the signal velocity be and how would it be influenced by the bends? Would the signal degradation be a strong function of bend geometry or only marginal? Since such transmission lines are full of discontinuities, would the even mode be excited and what would be its role? Could wirebonds improve signal propagation or not? The answers to these question lie in the analysis of the experimental measurements carried on these CPWs and is presented in chapter 5.

4.3 The second mask.

The second mask was designed with the results of chapter 5 in hand and had broader objectives. Like the first mask, it included some meander lines to study the effect of bends on the propagation characteristics. In addition, there were lines with different lateral dimensions and CPWs with wide ground planes. Some straight and bent CPSs were also added to the mask, together with other structures specifically designed to study the even mode.

The unit cell of the mask consisted of three separate frames. Each frame had an area of 8x4 mm^2, and could be diced individually since it was provided with separate external connections. The first frame, shown in Fig. 4.3, consisted of a total of five transmission lines, all of which had a conductor width S and separation W equal to 50 μm. The ground conductors of all transmission lines were connected to limit the number of wirebonds required to provide external connections.
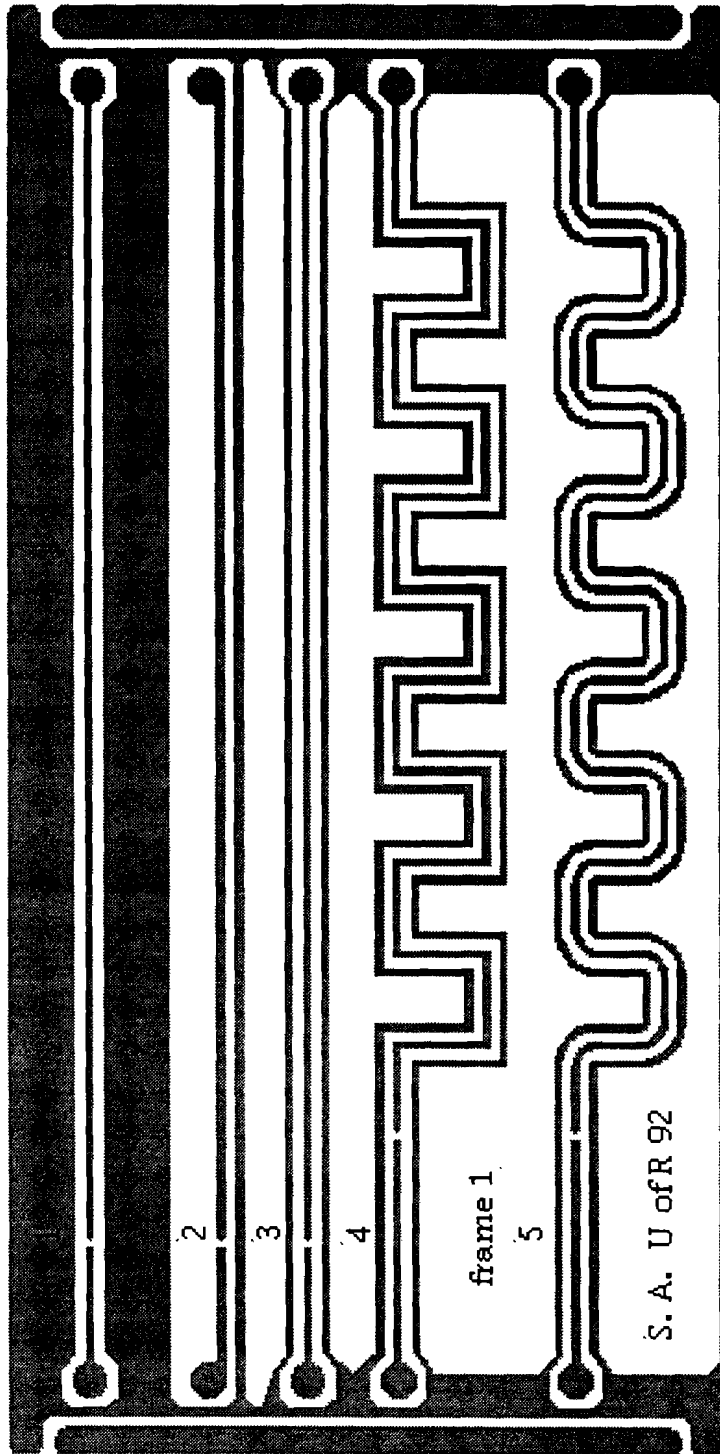
Fig. 4.3 A top view of frame 1 of mask 2. All lines have $S = W = 50$ μm and the frame size is 4x8 mm^2. The structure is actually very smooth, but some featurs may appear coarse because of the limited resolution of this image.

All signal lines incorporated a gap in their input site forming a photoconductive switch, seen in Fig. 4.4, and were terminated by wide circular bonding pats at each end. The width of the switch was increased from 20 to 30 μm to reduce its capacitance. A large rectangular pat was positioned at each end of the transmission lines to provide easy signal connections to the sample holder.
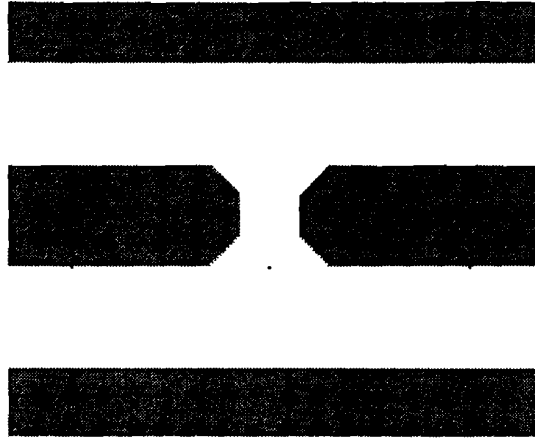
Fig. 4.4   A detailed view of the photoconductive switch configuration of the 50 μm transmission lines in mask 2. The black dots indicate the 100 μm grid.
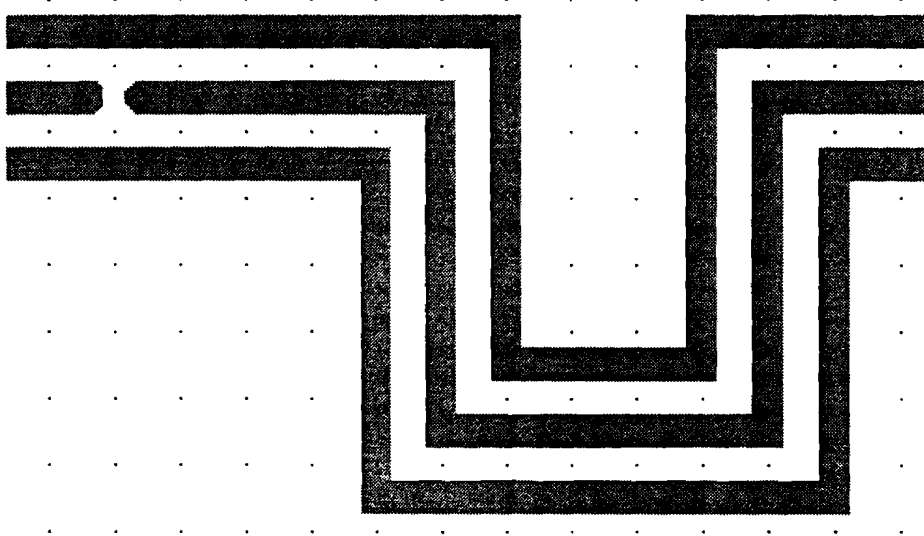
Fig. 4.5   A snapshot of a single meander from a 50 μm square bent CPW (transmission lines 4, frame 1). The black dots indicate the 100 μm grid.

Two of the lines in this frame (numbered 4 and 5), were bent CPWs with a reduced ground plane width of 50 µm. Like the transmission lines in the first mask, they had a meander period of ~2 mm (see~fig. 4.5). Approximately half of this distance was covered by the bends. Of the three straight lines, one was a CPS (line 2) and the other two CPWs. One straight CPW (line 1) had a relatively wide ground-plane width of 500 µm in contrast to line 3 which had a ground plane width of 50 µm, like the bent transmission lines. The purpose of this frame was to facilitate refabrication of the most important CPWs designed in the first mask (lines 3,4 and 5) and to enable the direct comparison of their characteristics with a wide ground CPW and its complementary CPS.
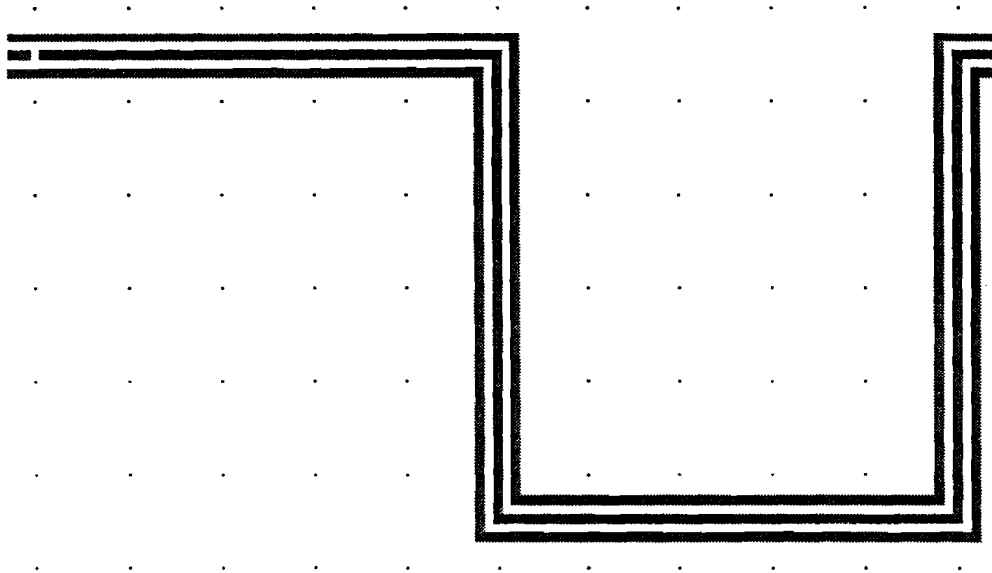
Fig. 4.6   A snapshot of a single meander from a 10 µm square bent CPW (transmission line 4, frame 2). The black dots indicate the 100 µm grid.

The second frame had a layout similar to the first, but consisted of transmission lines with lateral dimensions of 10 µm. There were six transmission lines in this frame, five of which were narrower replicas of the lines in frame 1. The sixth line was a meander type CPS with smooth bends. The photoconductive switches had the geometry shown in Fig. 4.4, but their dimensions were scaled down by a factor of five to match the reduction of the line lateral dimensions and keep the switch capacitance the same. The major difference between the 10 µm bent lines and the

ones in the first frame was the ratio of the bent area to the meander length. A comparison between Fig. 4.4 and 4.5 shows that the meander length was kept constant to ~2 mm, but the extent of the bends in the 10 μm lines was significantly reduced.

Frame 3 consisted of five 50-μm transmission lines as shown in Fig. 4.7. The meander lines (1, 5) belong to the same family of lines shown in frame 1, but were included in this frame to maintain uniform frame size. The characteristics of the wide ground CPW and the CPS would be directly compared to the smooth-bent CPW in the first frame (line 5). The narrow-ground CPWs (lines 2 and 3) had a single bend after the switch in order to provide for a sufficient straight path to study the excitation of the even mode. The two lines converged into one through a T-junction in the center of the frame in order to save space for the divider (line 4). The divider, seen in detail in Fig. 4.8, had wide ground planes and smooth bends. There was no close connection of the outside ground planes to the inner ground plane of the divider. The inner ground plane was only connected to the input port through the long inductive path around the output signal bonding pads. It would be of interest to know the extent the even mode can be excited and to what degree this effect could be minimized with wirebond connections.
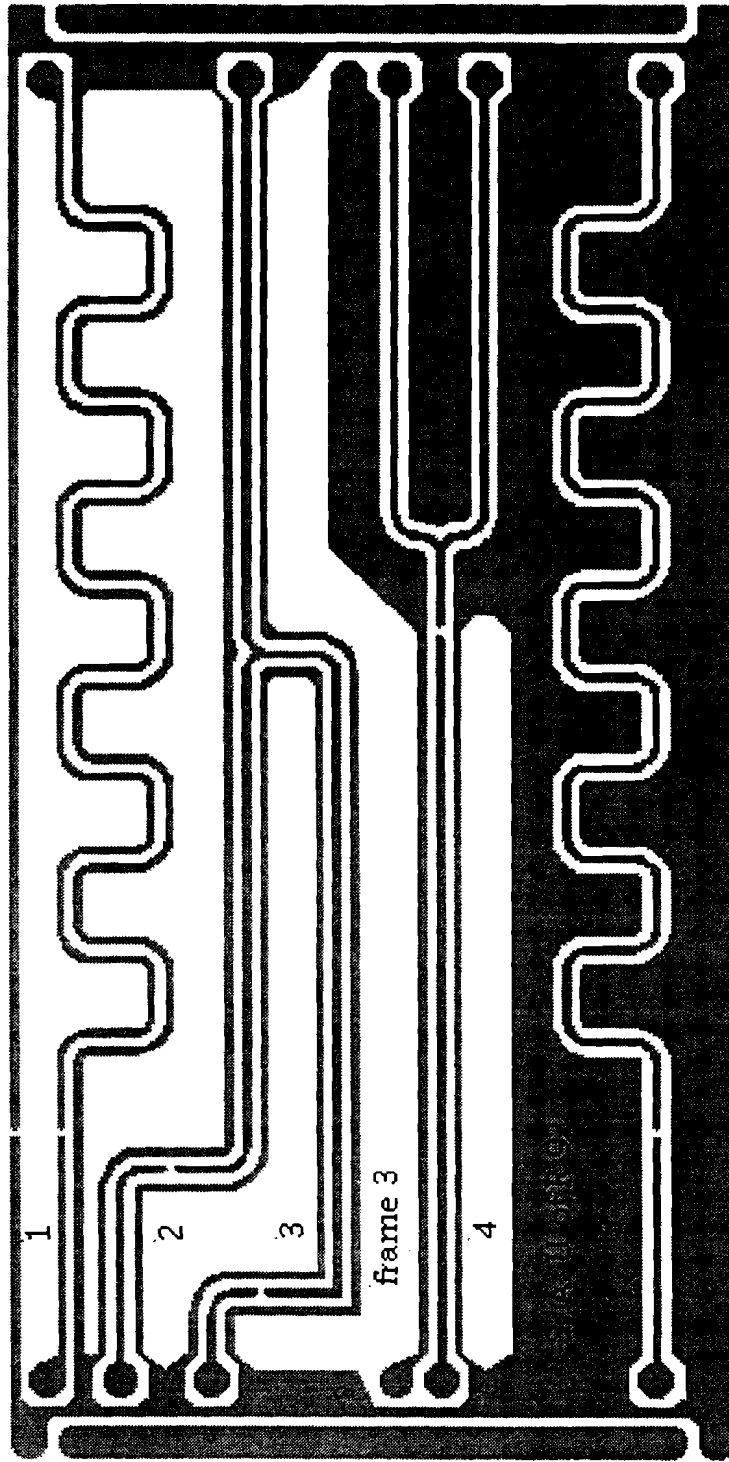
Fig. 4.7 A top view of frame 3 of mask 2. All lines have $S = W = 50$ μm and the frame size is 4x8 mm^2. The structure is actually very smooth, but some featurs may appear coarse because of the limited resoltution of this image.

Fig. 4.8   A detailed view of the 50 μm divider (line 4, frame 3). The black dots indicate the 100 μm grid. Again the actual layout of the structure is very smooth, but some features may appear coarse because of the limited resolution of the image.

PART B
4.4. The photoconductive switch

In its simplest form a photoconductive switch is a piece of photoabsorbing material, usually a semiconductor, placed between a pair of biased conductors. For high frequency applications, the switch is embedded into a transmission line, as shown in Fig. 4.9, so that the generated electrical signals can be guided.

The first requirement imposed on such a device is that its resistance in the absence of light is much smaller than the line impedance. This can be achieved with the use of semiconductors with low doping which increases the substrate resistivity. Another possibility is to choose a metal whose work function results in a high barrier Schottky contact at the metal-semiconductor interface. In the presence of bias, most of the voltage drop occurs across the switch.
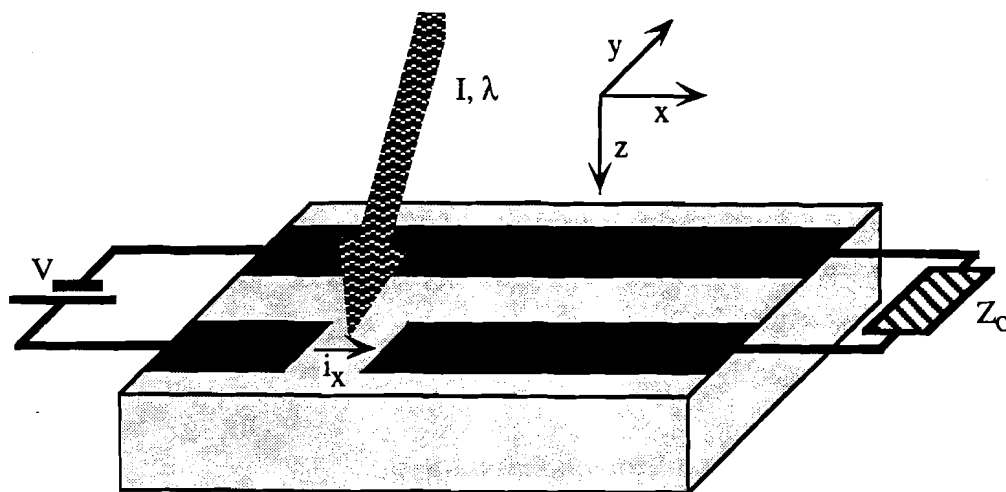
Fig. 4.9   A schematic representation of a photoconductive switch for high frequency applications.

When an optical pulse is incident on the switch it generates carriers and causes the flow of a current i_x, which travels on the transmission line in the form of an electrical pulse. The exact magnitude and temporal profile of this pulse depend on a range of parameters discussed below. In general, the current density J_x through a photoconductive switch can be expressed by,

$$J_x = \sigma\,E + \frac{\partial D}{\partial t} + q\left(D_p\frac{\partial p}{\partial x} - D_n\frac{\partial n}{\partial x}\right) + J_d \qquad (4.1)$$

$$\text{with} \quad \sigma = q\,(p\,\mu_p + n\,\mu_n) \qquad (4.2)$$

$$\text{and} \quad D = \varepsilon\,E \qquad (4.3)$$

where σ is the conductivity of the switch and E the electric field. The electron charge is denoted by q and the dark current density by J_d. n and p indicate the electron and hole concentrations, D_n and D_p their respective diffusion coefficients and μ_n with μ_p their mobilities. D is the electric flux density, and ε the dielectric permittivity of the substrate. This current flow is the result of four different processes each of which corresponds to a particular term in Eq. 4.1. The first term describes current drift and the second displacement current, while the third indicates diffusion

and the fourth the current in the absence of light. The first three terms are interdependent and are also functions of time and position in the switch. Moreover they are affected by recombination and transit time effects. As a result, the exact solution of this equation in its general form constitutes a challenging mathematical exercise. In practice, however, the switch only operates in either the drift, or the displacement current mode. The reason is that in such devices the carrier gradients are relatively small, and since the applied electric field is comparatively large, diffusion can safely be neglected.

4.5 Drift switches in the recombination limit

If the density of the photogenerated carrier is kept low, field screening effects which lead to displacement current can be neglected, and the photoconductive switch operates in the drift mode. The bias voltage is almost always high enough for the carriers reach saturation velocity and the drift current becomes independent of electric field. In this case the contacts between the metal-semiconductor barriers of the switch are Ohmic, the electron current is given by,

$$J_e = n \, q \, v_{sat} \tag{4.4}$$

$$\text{with} \quad n = \int_0^t \left(G - R_e \right) dt \tag{4.5}$$

where v_{sat} is the electron saturation velocity and G and R_e are the generation and recombination rates, respectively. The respective equations for holes have the same form, but their saturation velocity and recombination rate have different values. If we assume that the generation rate is a delta function and the recombination rate a single decaying exponential the electron concentration becomes

$$n = n_0 \, e^{-t/\tau_{re}} \tag{4.6}$$

where n_o is the carrier density at t = 0 and τ_{re} is the electron recombination lifetime. Equation 4.4 then becomes,

$$J_e = q\ v_{sat}\ n_o\ e^{-t/\tau_{re}} \tag{4.7}$$

In the case where the main recombination mechanism is electron-hole interactions the electron concentration would deviate from a single exponential dependence but it would still be a monotonically decreasing function with a characteristic decay time of the order of the recombination lifetime.
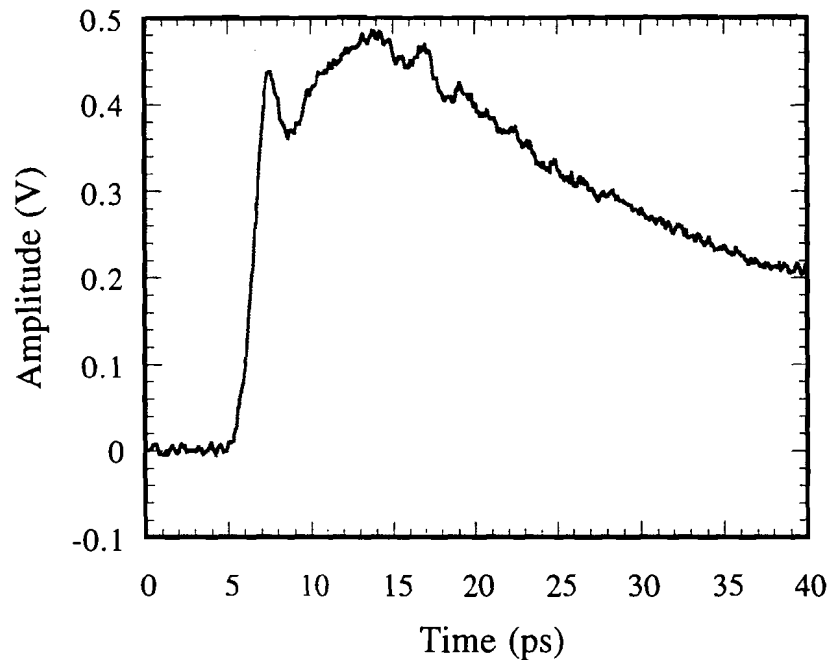
Fig. 4.10   Electrical waveform generated by a photoconductive switch on a semi-insulating GaAs substrate when excited by a femtosecond optical pulse.

The current described in Eq. 4. 7 is dampened by the RC time constant of the circuit, which in the microwave range reduces to the product of the switch capacitance and characteristic impedance of the line. A switch with dimensions of a few tens of microns, like the one shown in Fig. 4.4, has a capacitance of a few femtofarads which coupled to a line impedance of the order of 50 Ohms, gives a

subpicosecond RC time constant. As a result, the onset of the propagating current has a finite rise time even if the exciting optical pulse is infinitely short (delta function generation rate). The fall time, on the other hand, is dominated by the recombination lifetime if the substrate is a crystalline semiconductor. Even in GaAs, which has a direct bandgap, the recombination lifetime is of the order of several tens of picoseconds. For silicon, recombination lifetime is several orders of magnitude larger and falls well into the microsecond regime. Under these conditions, the pulses generated by photoconductive switches have fall times that are orders of magnitude larger than the corresponding rise times. Such a waveform generated by the excitation of a photoconductive switch on a GaAs substrate, is shown in Fig. 4.10. The asymmetry between the rise and fall time is strongly evident. In fact this waveform can be approximated by a step function rather than a pulse.

Historically, efforts to reduce the fall time of photogenerated pulses focused strongly on reducing the recombination lifetime [2]. This can be achieved by increasing the number of recombination centers in the substrate. Among the available alternatives is the introduction of traps in the substrate by doping (Cr in GaAs, As in low temperature grown (LT) GaAs [3,4]) or damaging (oxygen implantation of Si [5]), the implementation of polycrystalline photoconductive layers (CdTe [6]) or even amorphous substrates (a-Si) [7]. Once the recombination lifetime is reduced to a value comparable to the RC time constant, subpicosecond symmetrical pulses can be generated. Of these methods the most popular appears to be LT GaAs because it combines high resistivity with high breakdown voltage. The problem is that all the above procedures also reduce carrier mobility and therefore degrade the switching efficiency. Moreover, these processes are incompatible with high frequency device and circuit applications which nominally require high quality substrates.

4.6 Transit time effects

An alternative approach is to try to limit the duration of the photogenerated electrical pulse with Schottky barriers at the metal semiconductor interfaces of the switch. Such a device is frequently referred to as a metal-semiconductor-metal (MSM) photodiode. In this case carrier injection from the metal contacts is prohibited and the electrical pulse has to end when all the photocarriers reach the metal

electrodes. Mathematically, this process can still be described by Eq. 4.5 by replacing the recombination rate R_e with a transit time function T_{re} which dependents on geometry. To a first order approximation, the fall time of such a device at high fields is given by,

$$\tau_r = \frac{L}{2\ v_{sat}}$$

(4.8)

where L is the gap length. In the limit the gap length much shorter than the carrier mean free path, the photocarriers can move ballistically to the electrodes and the speed of the device can be greatly enhanced. In order to achieve fall times of few picoseconds in common semiconductors like Si or GaAs, it is required that the gap length has submicron dimensions. This requirement has been a severe drawback in the past, but with the evolution of modern UV photolithography which can achieve submicron dimensions even on large scale commercial integrated circuits, this obstacle has been overcome.
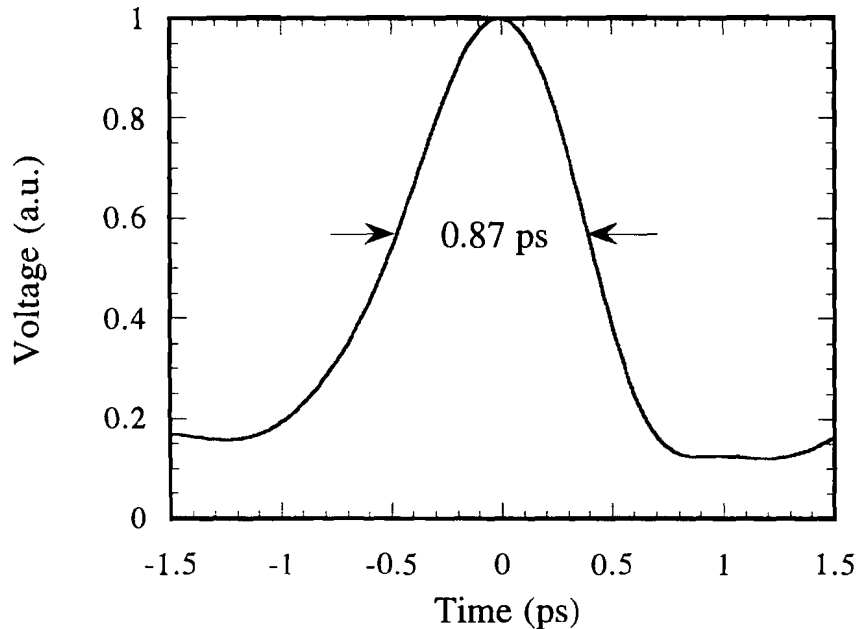
Fig. 4.11   An electrical waveform generated by the excitation of a 300 nm LT GaAs MSM photodiode with 620 nm photons.

Because the transit time devises require submicron switch lengths to achieve short fall times, they are usually fabricated with an interdigitated configuration which increases their area to enhance sensitivity and facilitate excitation by light beams of reasonable diameter. A number of such devises fabricated on GaAs , LT GaAs, Si and Si on insulator substrates have been tested in our lab [8-10]. Figure 4.11 shows the response of an interdigitated LT GaAs MSM photodiode which has a finger spacing (i.e. gap length) of 300 nm [8]. The electrical pulse has a subpicosecond duration with a 3 dB bandwidth in excess of 500 GHz and significant signal energy for frequencies up to a THz. The fall time of this pulse is actually shorter than it rise— an indication of signal dispersion as the signal traveled from the excitation spot to the measuring site. Measurements of devises on semi-insulating GaAs revealed ultrafast responses as short as 1.4 ps for a finger spacing of 100 nm [8].
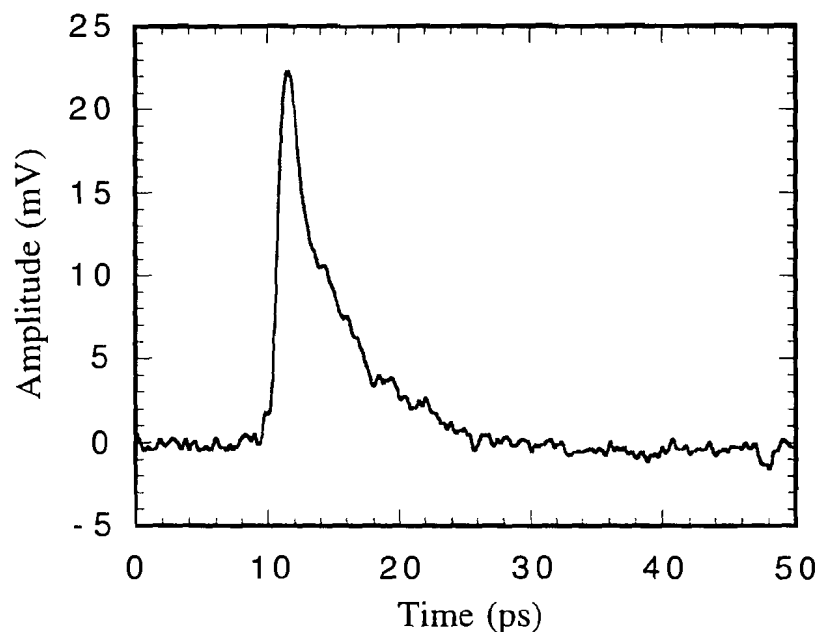
Fig. 4.12   The electrical response of a 200 nm crystalline Si MSM photodiode when excited by 400 nm photons.

The implementation of MSM structures on crystalline silicon enabled the generation of ultrashort pulses on this substrate for the first time [9]. In Fig. 4.12 we can see the response of a 200 nm device when excited by 400 nm photons. This waveform has a full width at half maximum (FWHM) of 3.7 ps. By shortening the

distance the photocarriers have to travel to reach the electrodes, the fall time of the electrical pulse was reduced by more than six orders of magnitude compared to the case the response is recombination limited.

The submicron separation of the interdigitated finger tends to confine the electric field close to the surface of the substrate and the response of the photodiode becomes sensitive to the carrier absorption depth. This means that response of the device is wavelength dependent, and can degrade for long light wavelengths which have long absorption depths. This problem can be solved by limiting the thickness of the absorption layer [10], but since not all photons are absorbed sensitivity may be compensated.

4.7 Pulse generation by field screening

All drift based photosensitive devises operate best at excitation levels where the density of the generated carriers is low and screening of the applied electric field is avoided. In the presence of field screening the carriers slow down, and the electrical response degrades [11, 12]. Another possibility to generate an ultrafast electrical pulse, is to use field screening itself rather than current drift. In this case a well focused beam only illuminates a part of the switch [13]. A large number of carriers are generated in the illuminated region and screen the electric field. However, since a large part of the switch's area is under dark, its resistance remains high and current drift is limited [14, 15]. Because the current drift is primarily limited by the dark resistance of the switch, the requirements on the metal-semiconductor contacts are very relaxed. Under these conditions the generated current is given by,

$$J_x = \varepsilon \frac{\partial E}{\partial t} \qquad (4.9)$$

If the carriers are generated by a femtosecond source, the rate of field screening is extremely fast, and the current pulse can have a subpicosecond duration [13,14]. Such a waveform, generated by the non uniform illumination of a switch on semi-insulating GaAs, is shown in Fig. 4.13. The generated pulse is only partly guided by the transmission line. A significant portion of energy is radiated from the

excitation site into the substrate. In fact with optimal geometry, field screening can be utilized for the generation of terahertz transients [16]. The secondary oscillations seen after the main pulse in Fig. 4.13, represents the portion of the radiation signal that was reflected from the back site of the substrate.
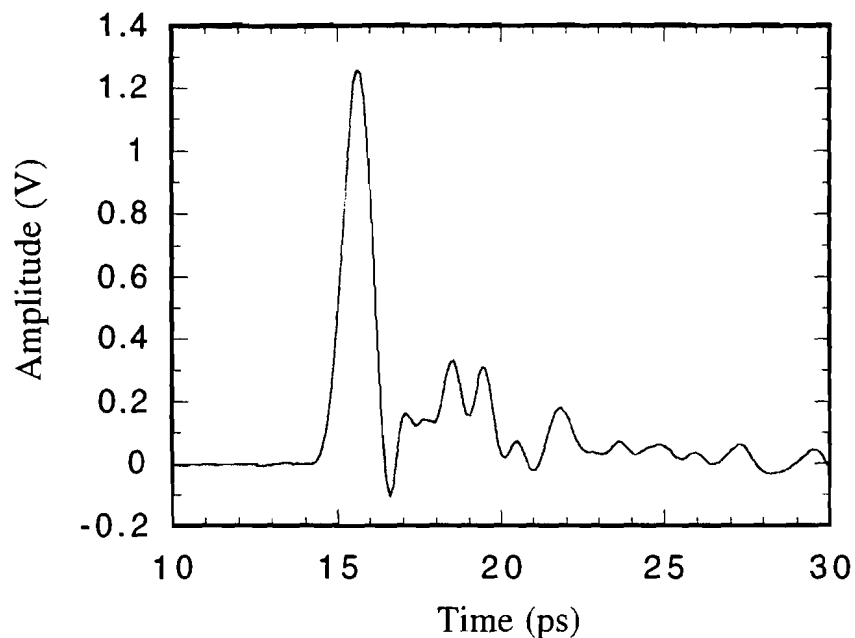
Fig. 4.13   A picosecond electrical pulse generated by the nonuniform illumination of a photoconductive switch.

4.8 Discussion

In the previous sections (4-7) we focused on range of methods that provide the picosecond pulses required for the high frequency analysis of our transmission lines. It would be fair, however, to mention some other possible alternatives. For example, ultrafast pulses can also be generated by a pair of switches on a high carrier mobility substrate if they are properly "gated". Depending on the relative timing of the light excitation beams, two step-like transients can be generated with different turn-on times. In this mode, one transient can be used to shut out the other and form a pulse [17]. Such a method was success fully implemented on microstrip lines [18]. Also,

insertion of capacitive or inductive discontinuities in the transmission line the signals are propagated on [19], can filter out the low signal frequencies and form a pulse. The main disadvantage of these methods is that the require additional chip area and extra hardware, and in practice, they are difficult to implement and function reliably.

Perhaps the most interesting method of all it the one that does not use photoconductive switches or ultrafast lasers [20]. Instead, a non linear transmission line is fed with a sinusoidal microwave signal at a moderate frequency of a few GHz. The transmission line nonlinearity is inducing amplitude dependent dispersion that distorts the sinewave signal to a picosecond shock wave. Unfortunately, the non linear transmission line has a complex design and requires a lot of chip area to implement, making direct integration with the circuit under test difficult.

Of the methods that we have already described in the last section, the use of a recombination limited device based on LT GaAs is very attractive since sensitivity is not a major issue in our measurements. However, LT GaAs has to be grown by MBE complicating the fabrication process. MSM photodiodes can in principle be integrated with the transmission lines in a single fabrication step. However, in order to generate subpicosecond pulses, electron beam lithography is required to pattern fingers with spacing less than 0.5 μm. Nonuniform gap illumination, on the other had, which can generate pulses through field screening is the most attractive method because its requirements are very relaxed. All that is needed is a simple gap an the transmission line. The contacts of the switch can be Schottky or Ohmic without much effect on the generated pulses. The amplitude of such pulses typically has a value of a few volts, making signal detection trivial even after the long propagation distances when the waveforms degrade. The only disadvantage of this method is the secondary radiative oscillations that follow the main pulse.

For the reasons we just described it was decided to use nonuniform gap illumination to generate pulses on the transmission lines. All the results presented in chapters 6 and 7 were extracted from pulses generated by this process.

Summary

In this chapter we a gave a description of the actual samples that were used for the picosecond measurements. We also discussed the ways through which picosecond

transients can be propagated on the transmission lines. More specifically, it is important to remember that:

- All samples were fabricated with a lift-off process on semi-insulting GaAs wafers.
- The first mask focuses heavily on bends, while the second also facilitates the study of the effects of lateral dimensions, ground plane width, and even mode excitation.
- The results presented in chapter 5 were extracted from samples fabricated with mask 1 using step-like transients.
- Samples fabricated using the second mask, were excited with picosecond pulses using nonuniform gap illumination, and the results are presented in chapters 6 and 7.

References

[1]   G. Goine and C. U. Naldi, "Coplanar waveguide for MMIC applications: effect of upper shielding, conductor backing, finite-extent ground planes, and line-to-line coupling," *IEEE MTT.*, vol. 35, No. 3, pp. 260-267, March 1987.

[2]   D. H. Auston, "Picosecond photoconductors: physical properties and applications," Picosecond optoelectronic devices edited by C. H. Lee, Academic press, 1984

[3]   O'Brien and Correlli, "Photoconductivity of Cr Compensated GaAs after Implant," *J. Appl. Phys.*, vol. 44, pp. 1921-23, 1973.

[4]   F. W. Smith, H. Q. Le, V. Diadiuk, M. A. Hollis, A. R. Calawa, S. Gupta, M. Frankel, D. R. Dykaar, G. A. Mourou, and T. Y. Hsiang, "Picosecond GaAs-Based Photoconductive Optoelectronic Detectors", Appl. *Phys. Lett.*, vol. 54, pp. 890–892, March 1989.

[5]   M. B. Ketchen, D. Grischkowsky, T. C. Chen ,C-C. Chi, I. N. Duling, N. J. Halas, "Generation of Subpicosecond Electrical Pulses on Coplanar Transmission Lines," *Appl. Phys. Lett.*, vol. 48, pp. 751–753, March 1986.

[6]   M. C. Nus, D. W. Kisker, P. R. Smith, and T. E. Hartvey, "Efficient Generation of 480 fs Pulses on Transmission Lines by Photoconductive Switching in Metalorganic Chemical Vapor Deposited CdTe," *Appl. Phys. Lett.*, vol. 54, pp. 57–59, January 1989.

[7]   D. H. Auston, A. M. Johnson, P. R. Smith, and J. C. Bean, "Picosecond Optoelectronic Detection, Sampling, and Correlation Measurements in Amorphous Semiconductors," *Appl. Phys. Lett.*, vol. 37, pp. 371–373, August 1975.

[8]   Y. Liu, S.Y. Chou, T. Y. Hsiang, S. Alexandrou, "Ultrafast Nanoscale Metal-Semiconductor-Metal Photodetectors on Bulk and Low Temperature Grown GaAs," *Appl. Phys. Lett.*, vol. 61, pp. 819–1821, August 1992

[9]   S. Alexandrou, C.-C. Wang, T. Y. Hsiang, Y. Liu, and S. Y. Chou, "A 75 GHz Silicon Metal-Semiconductor-Metal Schottky Photodiode," *Appl. Phys. Lett.*, vol. 62, pp. 2507-2509, May 17, 1993.

[10]   C.-C. Wang, S. Alexandrou, and T. Y. Hsiang, "Picosecond Characteristics of Silicon-on-Insulator Metal-Semiconductor-Metal Photodiodes," submitted to

the SPIE International Symposium on Optoelectronics and Microwave Engineering, Los Angeles, California 94.

[11]   E. Sano, "Two-dimensional ensemble Monte Carlo calculation of pulse responses of submicrometer GaAs metal-semiconductor-metal photodetectors," IEEE Trans. Electron Devices, vol. 38, no. 9, pp. 2075-2081 September 1991.

[12]   C. Moglestue, J. Rosenzweig, J. Kuhl, M. Klingenstein, M. Lambsdorff, A. Axmann, J. Schneider, and A. Hülsmann, "Picosecond pulse response of GaAs metal-semiconductor-metal photodetectors," J. Appl. Phys., vol. 70, no. 4, pp. 2435-2448, August 1991.

[13]   D. Krokel, D. Grischkowsky, and M. B. Ketchen, "Subpicosecond Electrical Pulse Generation Using Photoconductive Switches with long carrier lifetimes," Appl. Phys. Lett., vol. 54, no 11, pp. 1046-1047, March 1989.

[14]   S. Alexandrou, C.-C. Wang, R. Sobolewski, and T. Y. Hsiang, "Generation of Subpicosecond Electrical Pulses by Nonuniform Illumination of GaAs Transmission Line Gaps," to appear in the IEEE J. Q.E.
Also S. Alexandrou, C.-C. Wang, R. Sobolewski, and T. Y. Hsiang, "Subpicosecond Electrical Pulse Generation in GaAs by Nonuniform Illumination of Series and Parallel Transmission Line Gaps," OSA Proceedings on Ultrafast Electronics and Optoelectronics, S. Shah and U. Mishra, eds., vol. 14, pp. 209-212, 1993.

[15]   Xing Zhou, S. Alexandrou, and T. Y. Hsiang, "Monte Carlo Investigation of Subpicosecond Pulse Generation by Nonuniform Gap Illumination," submitted to Appl. Phys. Lett.

[16]   N. Katzenellenbogen and D. Grischkowsky, "Efficient generation of 380 fs pulses of THz radiation by ultrafast laser pulse excitation of a biased metal-semiconductor interface," Appl. Phys. Lett. vol. 58, pp. 222-224, 1991.

[17]   R. A. Marshland, C. J. Madden, V. Valdivia, M. J. Rodwell, and D. M. Bloom, "Picosecond Pulse Generation and Sampling with GaAs Monolithic Integrated Circuits," OSA Proc. Picosecond Electronics and Optoelectronics, vol. 4, pp. 16-21, March 1989.

[18]   D. H. Auston, "Picosecond Optoelectronic Switching and Gating in Silicon," Appl. Phys. Lett., vol. 26, pp. 101-103, February 1975.

[19] M. Y. Frankel, S. Gupta, J. A. Valdmanis, and G. A. Mourou, "Picosecond Pulse Formation by Transmission Line Discontinuities," *Electr. Lett.*, vol. 25, no 20, pp. 1363-1364, September 1989.

[20] D. W. Van Der Weide, J. S. Bostak, B. A. Auld, and D. M. Bloom, "All-electronic generation of 880 fs, 3.5 V shockwaves and their application to a 3 THz free-space signal generation system," Appl. Phys. Lett., vol. 62, pp. 22–24 , 1993.

5. Step excitation results

The aim of this chapter is to present a comprehensive experimental study of the propagation characteristics of picosecond, step-like transients on bent CPWs. Because of the historic dominance of the microstrip line as an interconnection medium in microwave integrated circuits, there is very limited experimental work on CPW discontinuities in general, and in bends in particular. The few earlier experimental studies of bent coplanar transmission lines were primarily limited to the low-frequency regime, where the bends were treated as point discontinuities. This work, on the other hand, concentrates on the sub-THz range where we will show that such treatment is no longer valid.

The presented results were measured electro-optically in samples fabricated on semi-insulating GaAs substrates with the first mask set, which consisted primarily of 50-μm meander-type CPWs, as described in Ch. 4 (sections 1 and 2). The propagated electrical waveforms presented here, were generated with the uniform illumination of photoconductive switches in the manner described in section 5 of Ch. 4. As a result, these waveforms had a step-like shape because of the long recombination lifetime of the substrate. The waveforms were probed at consecutive points along the CPWs in order to study their temporal evolution and velocity as they propagated on the transmission lines.

The chapter is basically an overview of three publications by the author [1-3] and is divided into three sections. The first is dedicated to the signal velocity in the CPWs and the temporal distortion of the propagating waveforms. Section 2 concentrates on the logistics of the even mode excitation induced by the bends, and discusses ways to avoid it. The third section gives a brief discussion of the experimental results together with the motivation for the pulse measurements which follow in chapters 6 and 7.

5.1 Propagation velocity and signal distortion in bent CPWs

Figure 5.1 shows the measured step-like electrical transients as they propagate along the right-angle bent CPW. The waveform (a) shows the input signal, while the waveforms (b), (c), (d) and (e) show the same signal after it propagated through 2, 4, 10, and 20 bends, respectively. Only the rising edges of the transients are shown for clarity. Similar waveforms were also observed in the other bend lines, as well as the straight CPWs. The results show that the transient's rise time became longer as it propagated along the line. This increase in rise time is the dominant effect in all the results presented in this section. The measured transients suffered no significant decrease in amplitude in the flat portion of the step-like signal. The reason is that for such a step-like waveform, the power spectrum is dominated by low frequencies which suffer comparatively low loss over a propagation distance of the order of 10 mm.
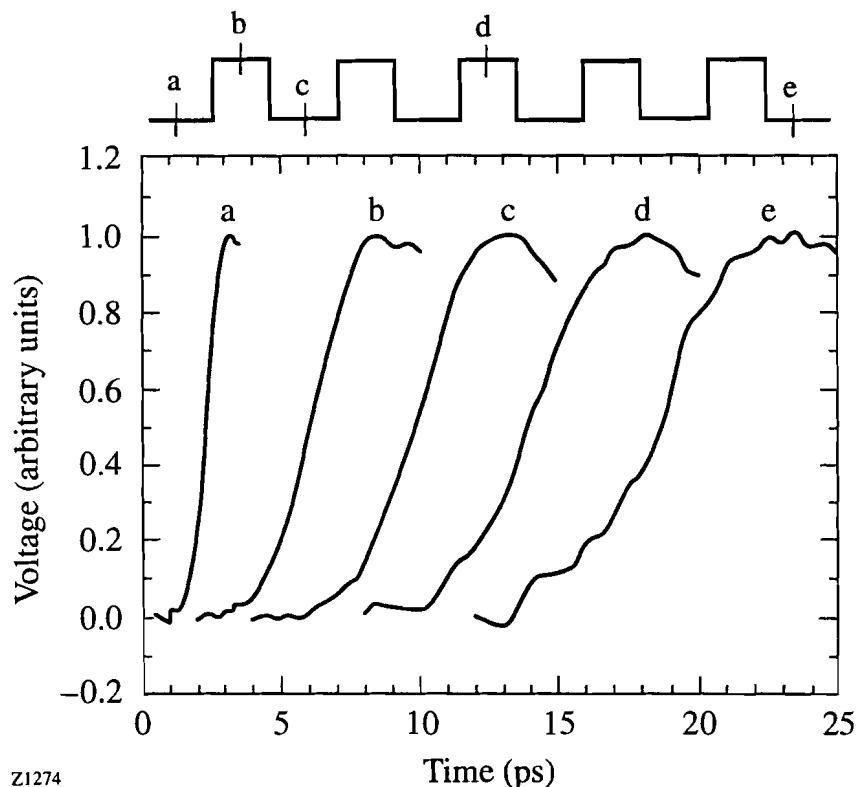
Z1274

Fig. 5.1 Measured waveforms propagating on right-angle bent CPW. (a) Input transient. (b),(c), (d), and (e) propagated signals after 2, 4, 10, and 20 bends. The waveforms are normalized with respect to input, and the arrival times are arbitrarily shifted. Each bend corresponds to an approximate propagation distance of 0.5 mm.

The dependence of propagation distance on arrival time for the transients propagated on several bent CPWs is presented in Fig. 5.2. We note that all the bent lines, as well as the straight CPW, exhibit the same propagation velocity, v, which is practically constant over the entire propagation distance. All data points (including the ones for the CPWs not presented in this figure) lay on the same straight line, which corresponds to the value of $v = 0.38\ c$ given by the quasi-static approximation (Eq. 3.2). The above result is in an excellent agreement with Ref. 4, and suggests that within our frequency range, the propagation velocity depends very weakly on the number of bends, or their shape. The observed nonlinear variations in v for different CPWs were so small that they are not visible in Fig. 5.2.
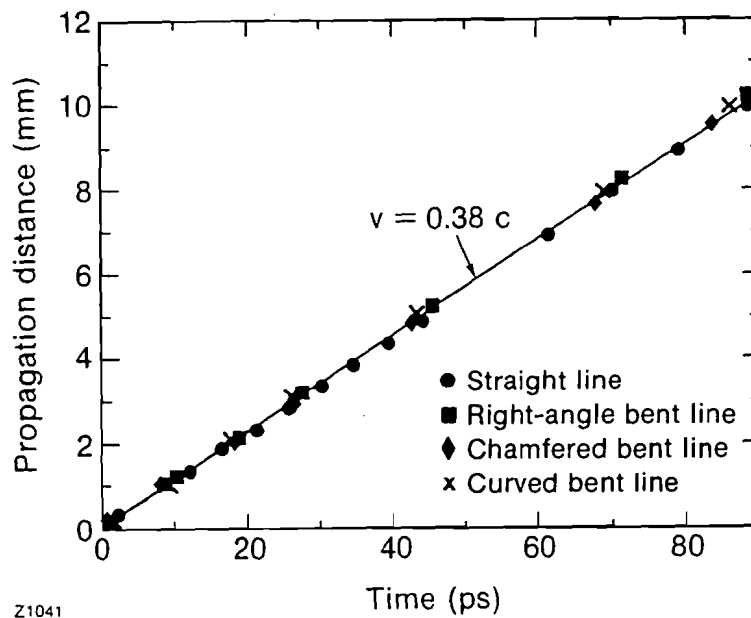
Fig. 5.2 Propagation distance versus time for the picosecond transients propagating on the straight and bent CPWs. The straight line corresponds to the signal velocity within the quasi-static limit.

Figure 5.3 presents more accurate measurements of v on the right-angle bent line. We see that a straight (constant velocity) line still fits well our propagation distance versus arrival time data. However, a more detailed analysis shows (see inset in Fig. 3) that for the right-angle bent line there is a ~4% difference between the initial (Region I) and final (Region II) propagation velocities. Smaller velocity differences were observed for the smooth-bent lines, and for the straight line (inset in Fig. 5). These results

indicate that when the transient looses most of its energy content at frequencies above f_{te} [see Fig. 3.4; 50 μm lines and f_{te} = 43 GHz], its propagation velocity increases. We believe that this is the first reported observation of modal dispersion seen as a direct difference in the velocity of the transients as they propagated on a long transmission structure.
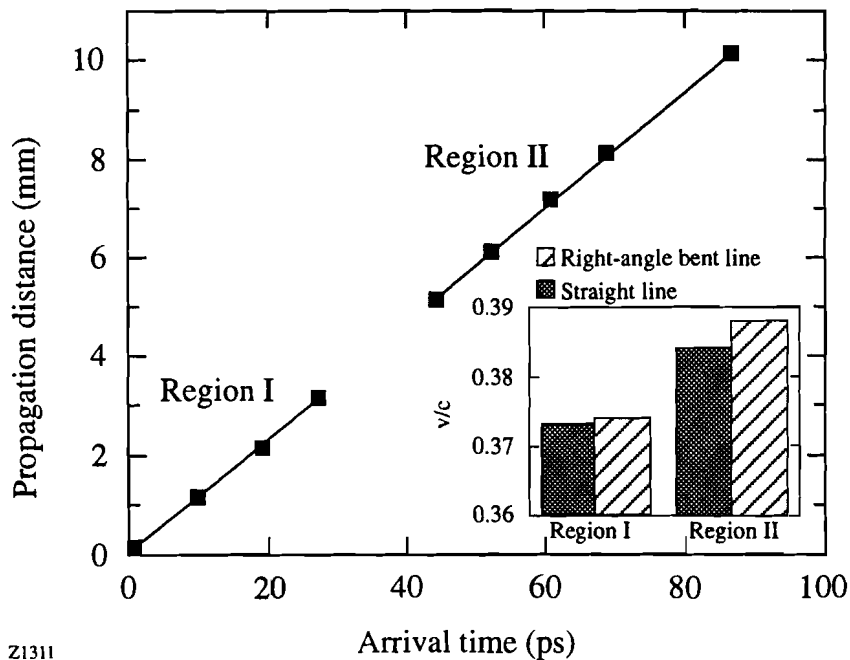
Fig. 5.3 Propagation distance versus arrival time for the picosecond transients propagated on the right-angle bent CPW. The inset shows the comparison between the initial (Region I) and final (Region II) propagation velocities extracted from the figure. The data for the straight line (not shown in the figure) are also added.

The impact of bends on the signal propagation quality in the CPW line is clearly visible in Fig. 5.4, which presents the dependence of the transient's rise times on the propagation distance for three bent-CPWs. We see that the signals exhibited considerably longer rise times in the initial propagation distance (0–3 mm; Region I in Fig. 3), compared to the straight line. The rise times are the longest for the right angle bent line. We associate this effect with extra high-frequency distortion and loss induced by the bends. For longer distances, the rise times continued to increase only for the right-angle-bent line, while for the smooth-bent lines, the values of the rise times leveled off to ~5 ps after 4 mm of propagation. In this regime (Region II in Fig. 3), the bent CPWs behaved almost like the straight line.
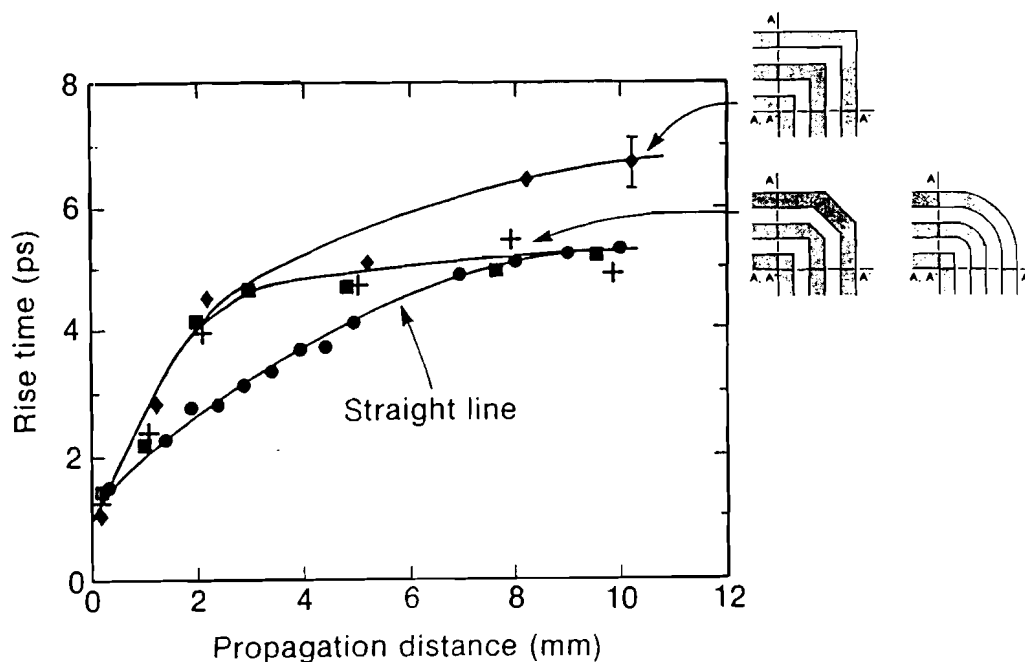
Fig. 5.4 Comparison of rise time versus the propagation distance between the right-angle bent, smooth-bent, and straight CPWs. The error bar on the last data point of the right-angle bent line represents the maximal error of our measurements. The solid lines are only to guide the eye. Note that a propagation distance of about 1 mm corresponds to 2 bends.

The overall change in the signal's rise time for each tested CPW is in good agreement with the corresponding change in the transient's velocity shown in Fig. 3. Thus, one could safely argue that transients with rise times that are fast enough to have significant spectral content at frequencies above f_{te}, will have a lower velocity compared to transients which have rise times with a spectrum confined to frequencies below f_{te}. Alternatively, for a given CPW, it is the rise time of the propagating waveform that determines its velocity on the line.

It must be noted that the propagation distance, plotted in Fig. 3 and 4, represents the full, physical length of the CPW, defined as the path along the center of the CPW signal line (see Fig. 5.5). The above observation supports an intuitive expectation that, at the sub-THz frequency range, the effect of propagation of the electrical signal along the bend must be fully taken into account. Thus, at these frequencies, one cannot follow the analysis given by Simons *et al.* [5], where the bend (defined as the region of the CPW between A–A and A'–A' cross sections in Fig. 5.5)

was treated as the point discontinuity with a small, frequency dependent length correction.

5.2 Excitation of Odd and Even Modes in the CPW Bend
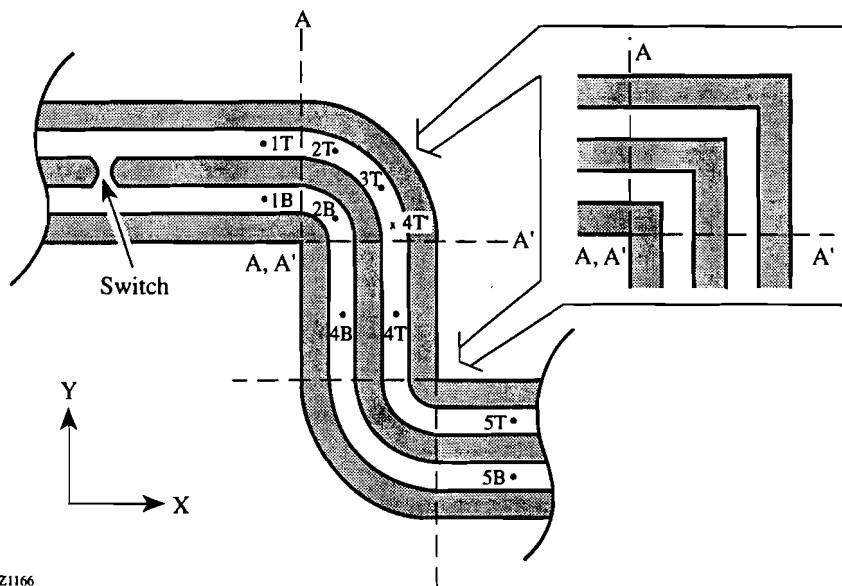
Fig. 5.5 Geometry of the section of the CPW transmission lines used to study the evolution of the even mode. The dots indicate the measurement positions.

The signal propagation measurements we have just discussed demonstrate that in the bend area there is a strong connection between the physical length of the transmission line and its velocity. The evident asymmetry between the two slots in the bend area is excepted to lead to the excitation of the even mode (as we have discussed in Ch. 3). In order to examine the manner this even mode is excited, we performed a series of measurements on a section of the CPW , shown in Fig. 5.5, consisting of a single pair of bends with opposite orientations. Two sets of bends with the most different characteristics were studied in detail, namely the right-angle and the smooth-bent shown in the figure. The numbered dots labeled on the transmission line in Fig. 5.5 (e.g., 1T and 1B), indicate the points where the waveforms were measured (T and B refer to the top and bottom slotlines, respectively).
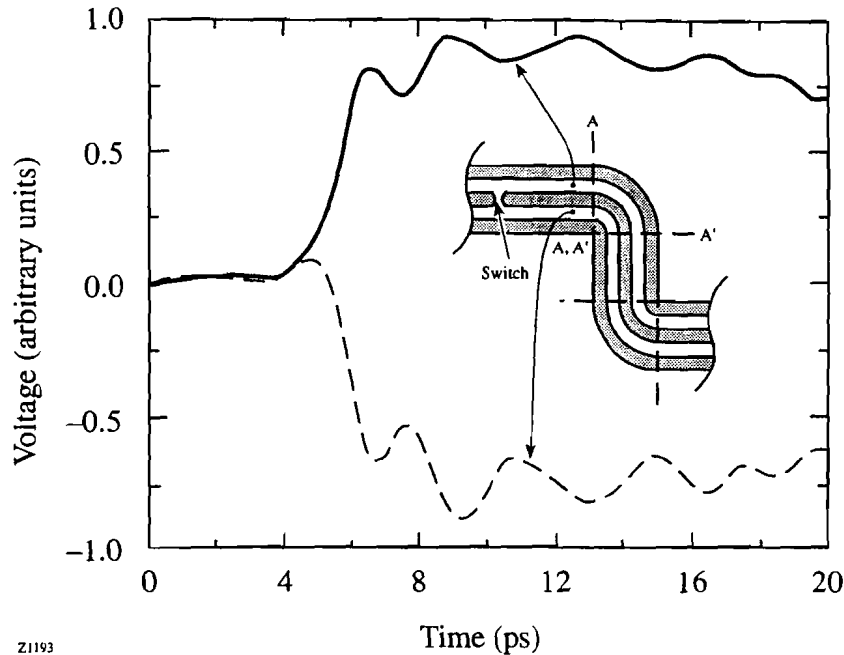
Fig. 5.6 The input signals measured before the first bend, indicated by section A-A.

Figures 5.6–5.15 present the time evolution of the picosecond transients as they propagate along our test structures. In Fig. 5.6 we show the input electrical transient, about 100 μm before it enters the first bend. It is evident that the waveforms in the top and bottom sides of the transmission line are essentially mirror images of each other—a fact that demonstrates the odd CPW mode propagation. The difference in the signal arrival times, defined as the time difference between the mid-points in rising edges of the two waveforms is effectively zero.

As soon as the transient enters the bend (Fig. 5.7; points 2T and 2B in Fig. 5.5), the picture changes dramatically. The transient at the top half of the line suffers a strong ringing and its amplitude is reduced. Simultaneously, the transient at the lower half, probed well inside the bend, is fundamentally different to the input and appears to be essentially balanced with respect to ground. These changes in the shape of the observed waveforms are attributed to the following factors: (1) The electro-optic crystal detects the presence of an electric field only in the Y direction. As the transient enters the bend, however, the wavefront stops being parallel to the Y axis and consequently, the X-axis component (undetected by the probing crystal) becomes substantial. (2) The reflections from the bend itself interfere with the incoming transient, changing its

overall shape. (3) The electromagnetic radiation emitted from the line [6,7] becomes an important contributor in the overall signal amplitude since the Y component of the signal is reduced. It should be mentioned that the transient probed at point 3T in Fig. 1 (waveform not shown) strongly resembles the one probed at 2B. Similar behavior is also seen in the right-angle bent CPW.
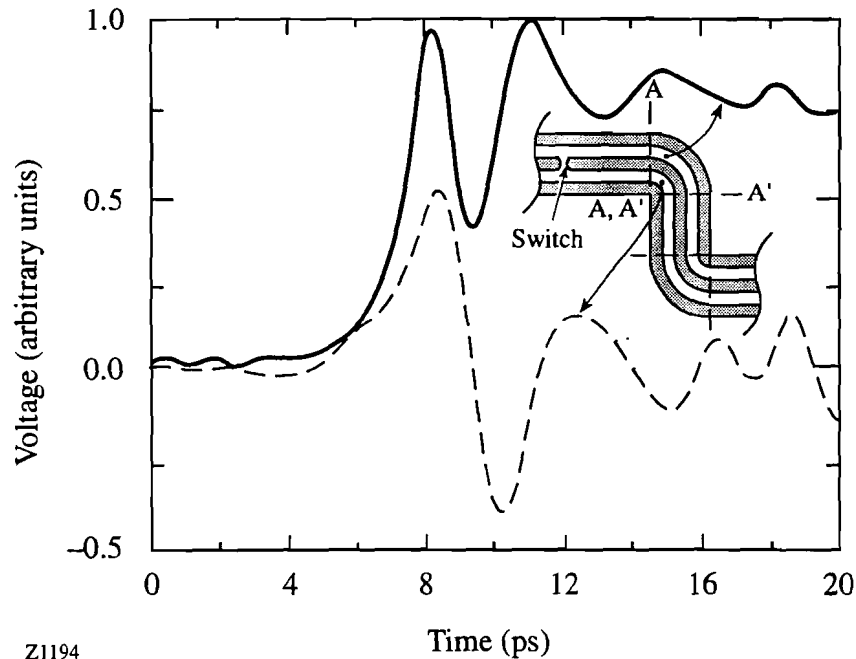
Fig. 5.7 The electrical transients measured inside the curved bend (points 2T and 2B). Only the Y component of the electrical field is recorded.

After the first bend, the electro-optic crystal was rotated by 90° and the measured transients are shown in Fig. 5.8 and 5.9. There is now a 1.4-ps time separation in the arrival times of the signals in the smooth-bent line [Fig. 5.8], which exactly corresponds to the geometrical path difference between the two sides of the bend. For the right-angle bend [Fig. 5.9], the behavior is identical and the measured delay has a value of 1.65 ps, close to the expected 1.75 ps. These observations indicate that inside the bent CPW the signals travel at the same speed in both slot lines and, consequently, they arrive first in the branch with the shorter geometrical length. It is interesting to note that the bend-induced delay corresponds to a significant space separation of the wavefronts. In other words, after one transient had exited the bend, the other was 160–190 μm behind. For example, in the case of the curved CPW, when

one transient arrives at point 4B, the other is still at point 4T' (shown as an "x" in Fig. 5.5), well inside the bend.
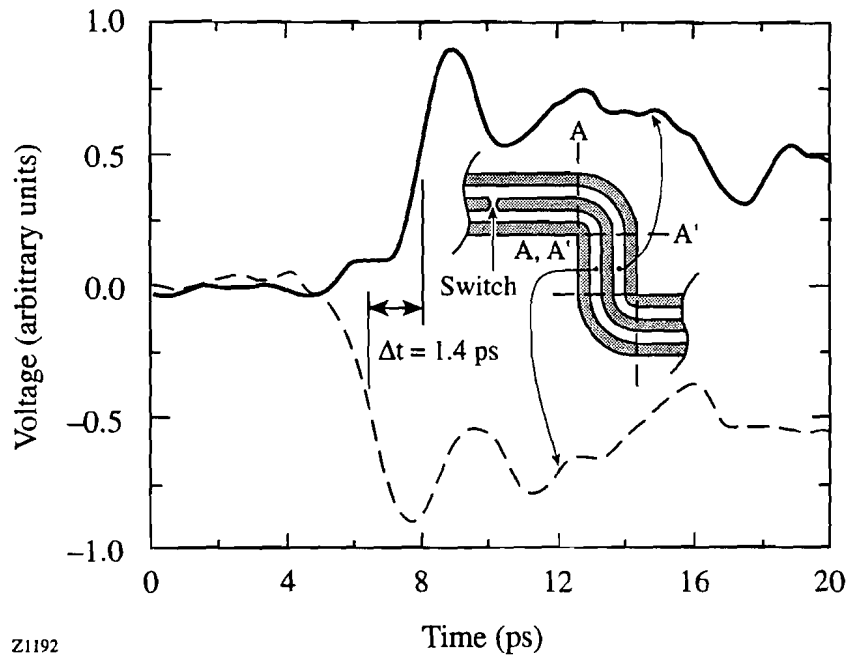
Z1192

Fig. 5.8 The propagated electrical transients measured after the curved bend (points 4T and 4B). There is a clear relative delay between the two signals
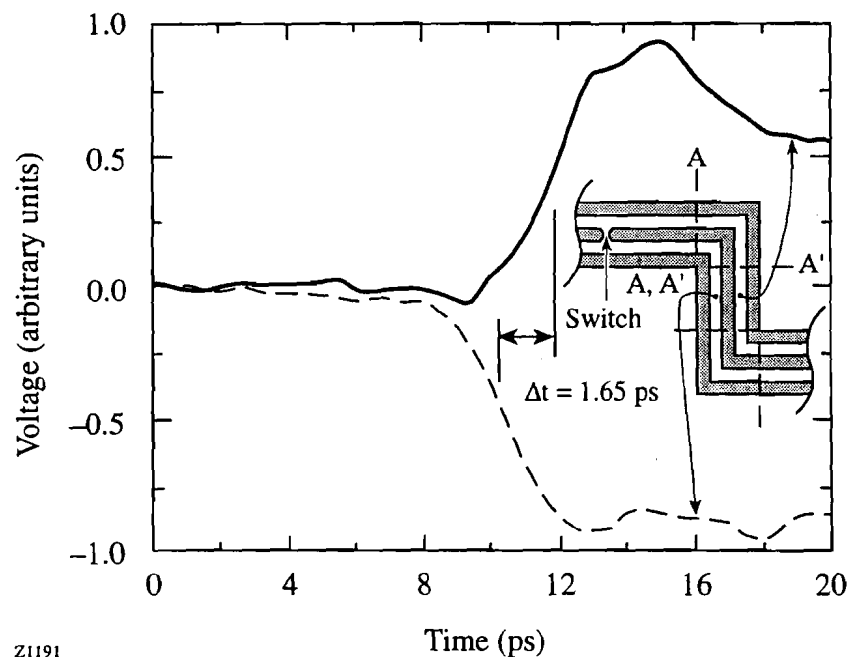
Z1191

Fig. 5.9 The propagated electrical transients measured after the right-angle-bend (points 4T and 4B). Again, there is a clear relative delay between the two signals.

The measured time delay between the waveforms shown in Fig. 5.8 and 5.9, demonstrates that the electric fields in the two slots do not correspond to a single odd propagational mode and must be expressed as the superposition of both the odd and the even mode. The presence of the even mode is an undesirable feature in practical applications, as this mode exhibits higher radiation loss [8] and dispersion [9,10].

Z1190
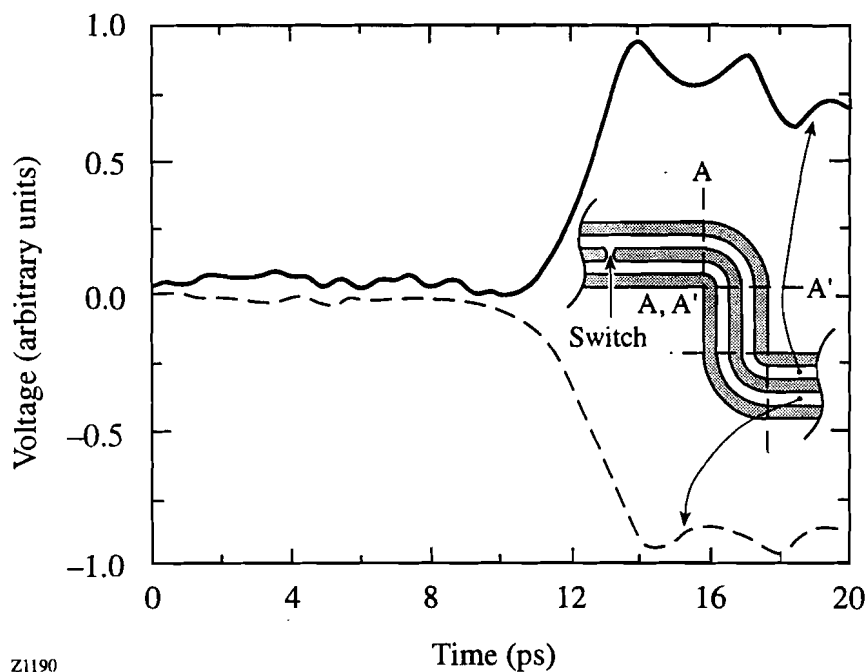
Fig. 5.10 The waveforms measured after propagating through a pair of curved bends.

Figures 5.10 and 5.11 present the waveforms after they traveled through a pair of oppositely oriented bends. For both bend geometries the waveforms are again timed and antisymmetrical. Thus, a second bend, placed adjacent to the first one, re-establishes the odd-mode propagation. Unfortunately, this method can be implemented only if there is enough room on the chip; and, as we have shown in the previous section, it inevitably leads to additional signal distortion because of the added propagation length.
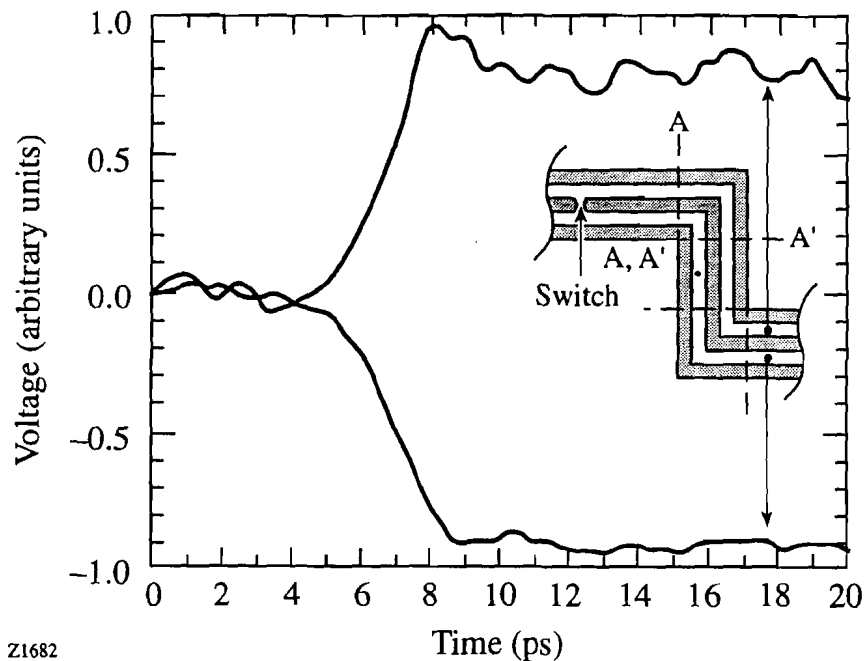
Fig. 5.11 Electrical transients measured after propagating through a pair of right-angle bends.

It is known that the excitation of the even CPW mode can be suppressed by ensuring that the two ground conductors are at the same potential [11]. This can be accomplished by the implementation of a "ground strap" connecting the two grounds of the CPW. We have fabricated such structures by wirebonding the two ground lines of a bend along the cross-section A'-A' (see insets in Fig. 5.12). The signals were again probed after the first bend [see Figs. 5.12 and 5.13] and, indeed, no time separation between the signals in the two slots was observed. Thus, the local grounding successfully suppressed the even-mode excitation inside the CPW bend.
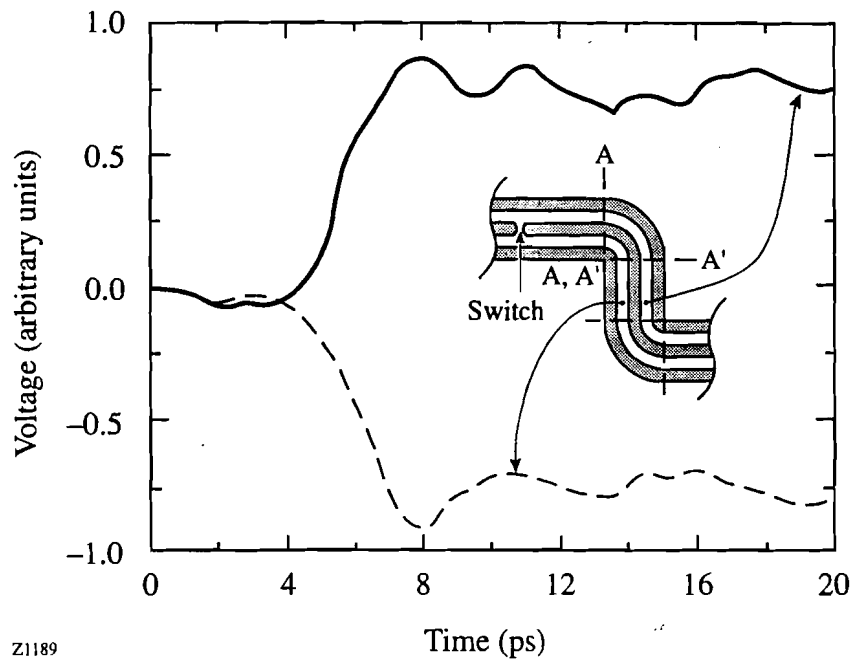
Fig. 5.12 The waveforms probed at points after the curved bend, with wirebonds connecting the two grounds at sections A'-A'.

Z1189
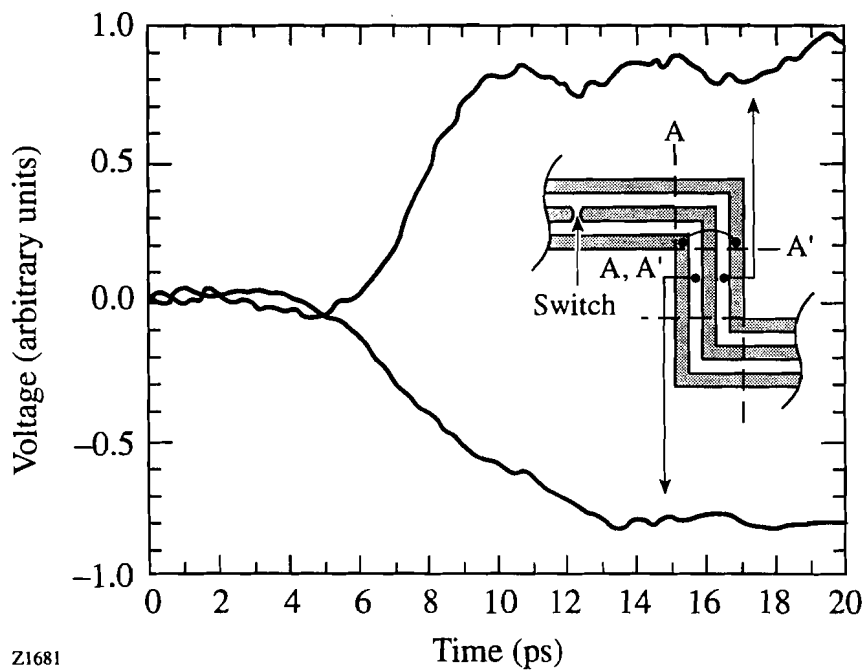
Fig. 5.13 The waveforms probed at points after the right-angle bend, with wirebonds connecting the two grounds at sections A'-A'.

Z1681

A comparison of the transients shown in Fig. 5.8 & 9 (no wirebonds) and Fig. 5.12 & 13 (with wirebonds) demonstrates that in both geometries the wirebonds caused the same (about 40%) relative increase in the signal rise times (2.7 ps versus 1.9 ps for the smooth bend and 3.3 ps versus 2.3 ps for the right-angle bend). This would indicate additional dispersion and, perhaps, attenuation due to the application of the ground straps. This is true only if the signals in the individual slots are considered separately. A different perspective can be seen in Fig. 5.14, where we compare the data in Fig. 5.12 with the arithmetic average of the two transients shown in Fig. 5.8. The two signals are now closely similar to each other, and the small difference observed is within the experimental error (note that these are separate, independent measurements). A similar comparison on the right-angle bends arrived at the same conclusion.
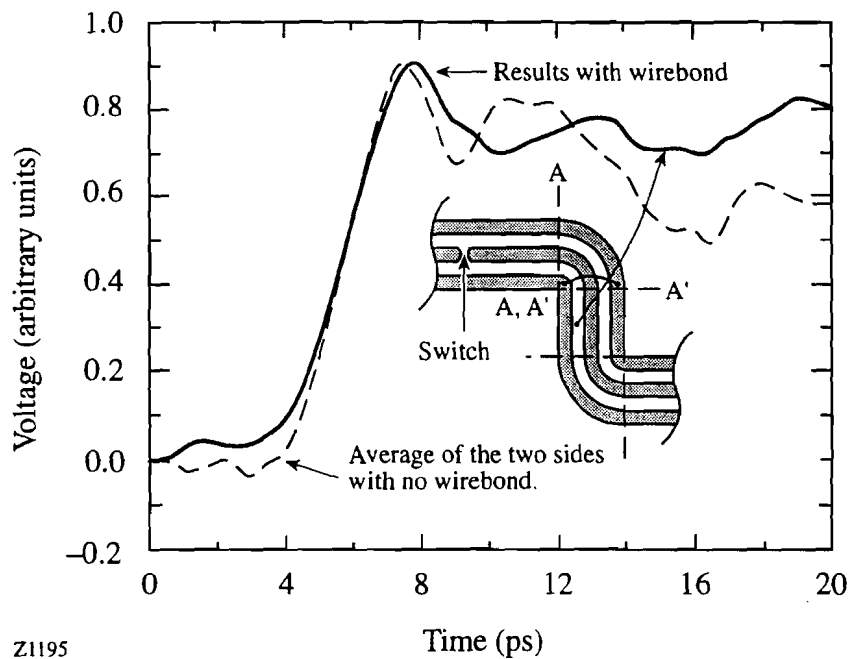
Fig. 5.14 The waveform from Fig. 5.12 compared to the arithmetical average of the two waveforms from Fig. 5.8. The difference in the rise times of the waveforms is only 0.2 ps.

One can understand the above observations by a consideration of the impedance of the ground strap. The wirebond used for the strap had a diameter of 35 μm and a length of ~150 μm, corresponding to an inductance of ~60 pH. At the dominant

frequency of our transient, around 130 GHz, this wire-bond should represent an impedance of ~50 Ω, comparable to the CPW characteristic impedance. However, the characteristic impedance for the even-mode propagation is actually approximately determined by the two ground conductors only [11], which in this case is about 130 Ω (coplanar stripline width S = 150 μm, W = 50 μm), much larger than the wirebond impedance. Thus, the results in Fig. 5.14 are consistent with the intuitive notion that the ground strap effectively "shorts out" the even mode.

It would be interesting to observe the effect of the ground strap at even higher frequencies. For example, at 1 THz, the strap impedance would become ~400 Ω, much larger than the stripline impedance (which would further decrease at such a high frequency because of the increase in the effective dielectric permittivity of the line), and one would expect the even modes to be unaffected by the ground strap. This effect will be discussed in the following chapters.

ZI188
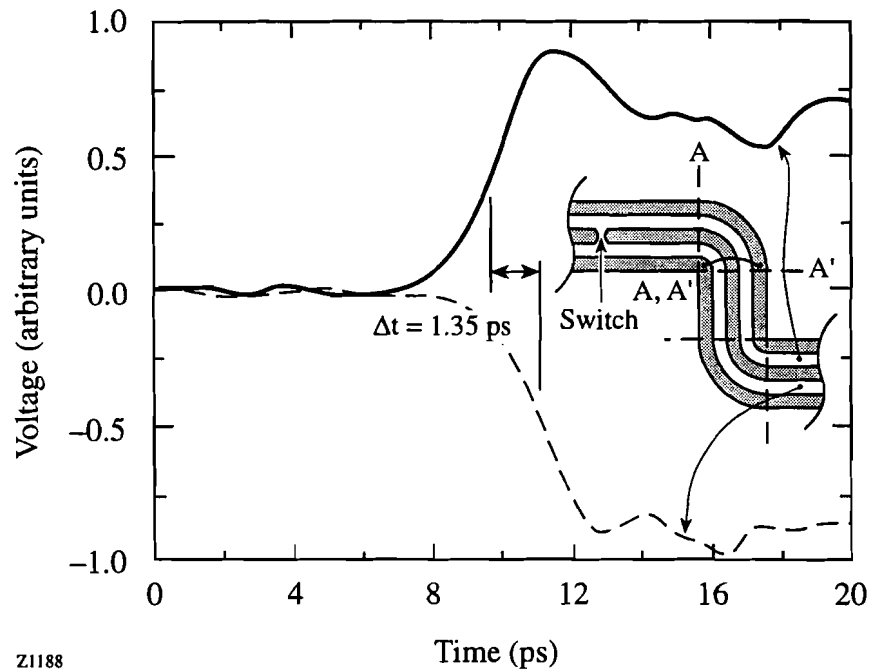
Fig. 5.15 The waveforms measured after propagating through a pair of oppositely oriented curved bends. The first bend has a ground strap but the second does not, and consequently there is a relative delay between the two transients.

We further note that the effect of the wirebond grounding is local. When the transients passed the second bend (see Fig. 5.15), their arrival time separation

reappeared, and its value was 1.35 ps—almost the same as in Fig. 5.8. Thus, in order to keep the signal timed on both sides of the bent CPW, grounding must be implemented after every bend of the line. Exactly the same phenomenon was also observed for the right-angle bent lines.

5.3 Discussion and Summary

We have measured the propagation characteristics of picosecond step-transients on 20 bent CPWs over a distance of about 10 mm. Our results demonstrate that picosecond transients, having a bandwidth in excess of 100 GHz, can propagate over a large number of bends with limited signal distortion. We found that the physical length of the bent CPW had to be taken into account in order evaluate the signal propagation velocity correctly. In this manner, the signal velocity is primarily determined by the spectral content of the propagating waveform rather than the geometry of the bends. Also, we showed that smoothing of the bends considerably improves the high frequency performance of the bent CPWs.

Moreover, we observed a time separation larger than 1 ps between the electrical transients propagated on the two slots of a CPW bend. The separation was due to the bend-induced excitation of the even CPW mode. We found that the even mode could be suppressed by connecting the two ground lines of the bend with a ground strap. This action restored the antisymmetry of the electric field vectors in the signals propagated in the two sides of the CPW. Another way to eliminate the even CPW mode was to implement a pair of oppositely oriented bends into the transmission line.

Our results with the step-excitation pulses have provided useful information on the performance of the bent CPWs at sub-THz frequencies. Important parameters, such as the propagation speed, signal distortion, and even-mode excitation were measured. They are of primary interest for very high-speed digital circuits, where the pulse shape and the signal arrival time are the main parameters of interest. However, for analog (microwave) applications direct results on attenuation and dispersion, measured in a wide-frequency domain, are important. In this case, measurement time windows in excess of the transient's duration are required in order to provide information about the signal distortion parameters. For the step-function excitations presented in this chapter, such measurements are difficult since the pulses are long and reflections always interfere with the main transient degrading the accuracy of the measurement. The latter

problem can be eliminated by studying propagation of very short pulses (about a picosecond wide) on the bent CPW. The short duration of such δ-function-like pulses provides the required bandwidth and confines all the useful information in a relatively short time interval. This facilitates a frequency-domain analysis of attenuation and dispersion in the bent CPW. Such experiments picosecond pulses are presented in Chapters 6 and 7.

References

[1] S. Alexandrou, R. Sobolewski, H. Nakano, B. C. Tousley, and T. Y. Hsiang, "Picosecond Characterization of Bent Coplanar Waveguides," *IEEE Microwave and Guided Wave Lett.*, vol. 1, pp. 236–238, September 1991.

[2] S. Alexandrou, R. Sobolewski, and T. Y. Hsiang, "Bend-Induced Even and Odd Modes in Picosecond Electrical Transients Propagated on a Coplanar Waveguide," to appear in *Appl. Phys. Lett.*, vol. 60, pp. 1836–1838, April 1992.

[3] S.Alexandrou, R.Sobolewski, and T.Y.Hsiang, "Time-domain characterization of bent coplanar waveguides," *IEEE J.Q.E.*, vol. 28, pp. 2325-2332, October 1992.

[4] D. R. Dykaar, A. F. J. Levi, and M. Anzlowar, "Ultrafast coplanar air-transmission lines," *Appl. Phys. Lett.*, vol. 57, pp. 1123–1125, September 1990.

[5] R. N. Simons, G. E. Ponchak, K. S. Martzaklis, and R. R. Romanofsky, "Channelized coplanar waveguide; discontinuities, junctions, and propagation characteristics," *IEEE MTT-S International Microwave Symposium Digest*, pp. 915–918, 1989.

[6] D. P. Kasilingam and D. B. Rutledge, "Surface-wave losses of coplanar transmission lines," *IEEE MTT-S Int. Microw. Symp. Dig.*, pp. 113–116, 1983.

[7] D. Grischkowsky, I. N. Duling, III, J. C. Chen, and C.-C. Chi, "Electromagnetic shock waves from transmission lines," *Phys. Rev. Lett.*, vol. 59, pp. 1663–1666, October 1987.

[8] M. Riaziat, R. Majidi-Ahy, and I.-J. Feng, "Propagation modes and dispersion characteristics of coplanar waveguides," *IEEE MTT.*, vol. 38, pp. 245–251, March 1990.

[9] R. Majidi-Ahy, K. J. Weingarten, M. Riaziat, D. M. Bloom, and B. A. Auld, "Electrooptic sampling measurement of dispersion characteristics of slot line and coplanar waveguide (coupled slot line) even and odd modes," *IEEE MTT-S Int. Microw. Symp. Dig.*, vol. 1, pp. 301–304, May 1988.

[10] P. Singkornrat and J. A. Buck, "Picosecond pulse propagation in coplanar waveguide forward directional couplers," *IEEE MTT.*, vol. 39, pp. 1025–1028, June 1991.

[11] T. Itoh, Ed., *Planar Transmission Line Structures.* New York: IEEE Press, 1987, p. 253.

[12] G. Goine and C. U. Naldi, "Coplanar waveguide for MMIC applications: effect of upper shielding, conductor backing, finite-extent ground planes, and line-to-line coupling," *IEEE MTT.*, vol. 35, No. 3, pp. 260-267, March 1987.

6. Pulses in the time domain

In this chapter we present the experiments through which picosecond pulses were used to investigate the characteristics of our transmission lines. These pulses were generated with the method of nonuniform illumination of a photoconductive switch, in the manner described in chapter 4 (section 7), on samples fabricated on semi-insulating GaAs substrates using the second mask. Our analysis is carried out in the time domain and is primarily qualitative in nature. Quantitative analysis in the frequency domain will be presented in the next chapter.

Three separate sets of geometrical structures were tested in order to provide a well rounded description of the transmission line characteristics. The first section in this chapter is dedicated to 50 µm straight lines. CPWs with wide and narrow ground conductors, as well as, CPS were investigated. The effect of the line lateral dimensions is addressed in section 2 with emphasis on the characteristics of the 10 µm lines. Fifty micron bent-lines with characteristics similar to the transmission lines in section 1, are described in section 3. Similarly, 10 µm bent-lines are investigated in the fourth section. The remaining 2 sections are primarily dedicated to the study of the even mode excitation. Starting with section 5, we study the odd and even modes after a single curved bend together with the influence of wirebonds. Section 6 addresses the excitation of these modes after the two ends of an asymmetric T-junction.

6.1 Straight lines—50 μm technology

For the proper characterization of the straight CPWs we have to ensure that the generated signal travels in the odd CPW mode. This means that the signals in the two slots of the transmission line need to have the same amplitude and shape. Because of the symmetry of straight lines, this is usually easily achieved as seen in Fig. 6.1. The oscillatory waveform that follows the main pulses represents radiation [1] which is emitted from the excitation site and subsequently reflected by the back side of the substrate [2]. Even though the signal-to-noise ratio in these measurements is excellent, the weak multiple-order reflections of the radiation signal add an extra noise on the measured waveforms after the main pulse.
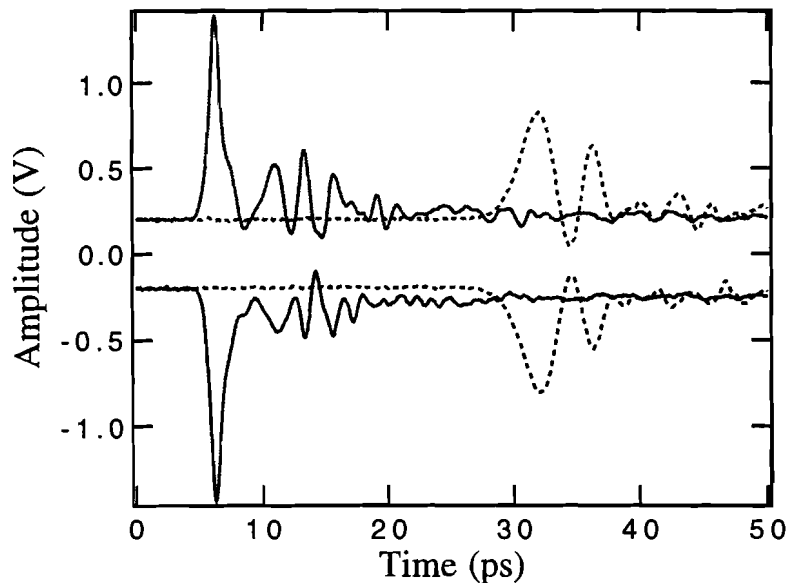
Fig. 6.1   Electrical pulses generated by the nonuniform illumination of a photoconductive switch on a 50 μm CPW with a narrow ground. The waveforms are measured in each slot of the line after propagating 250 μm and 3 mm, respectively.

For the correct characterization of each CPW we use the average of the waveforms measured in each slot of the line—the odd mode signal. In this manner, we can compensate for any small amplitude uncertainties that may arise from the signal amplitude calibration. The rejected signal, which represents the even mode, is usually an order of magnitude smaller and has a strong resemblance to the radiation signal measured on an adjacent CPS (see fig. 6.2). This evidence prompts us to

believe that in straight lines most of the even mode energy comes from radiation. Thus, by only including the odd-mode signal in the analysis of the straight lines, we can limit the interfering radiation and take advantage of signal averaging to give a better description of the CPWs.
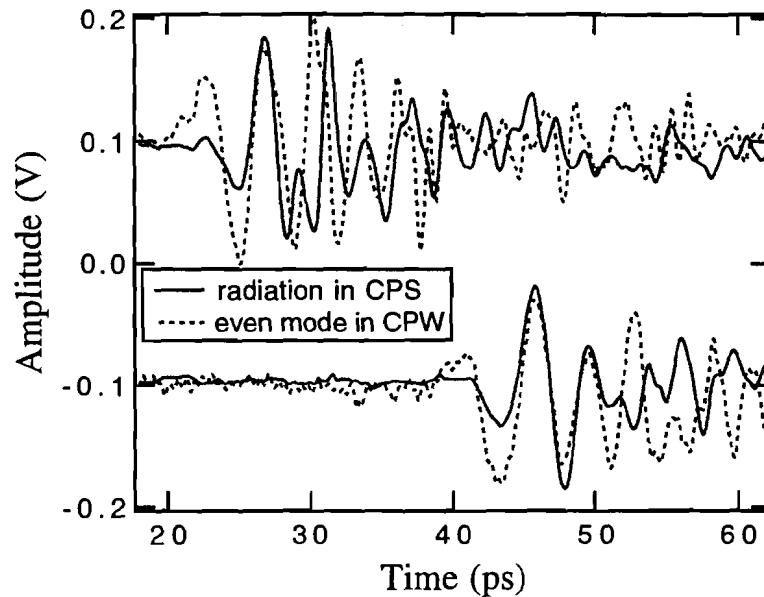
Fig. 6.2   Even mode signals, measured after propagating approximately 2 and 4 mm on a 50 μm CPW with a narrow ground, compared to the radiation signals on a nearby CPS at the same distances.

Some representative pulses, extracted by the method we have just described, are shown in Fig. 6.3. They were measured at identical positions on two 50 μm CPWs, one of which had a ground conductor width of 500 μm and the other 50 μm (lines 1 and 3 of frame 1; Fig. 4.3). In both transmission lines, the pulses become broader and their peak amplitude is reduced as they travel away from the excitation site. If we briefly concentrate our attention on the narrow-ground line, we notice that after propagating a distance of almost 5 mm the peak amplitude reduction is small. Further, the high frequencies, which are visibly delayed and show as dispersive ringing after the main pulse, do not contribute to the main peak. This observation suggests that the loss on this CPW over a distance of few millimeters is limited, and that the pulse shape and amplitude is primarily determined by dispersion.
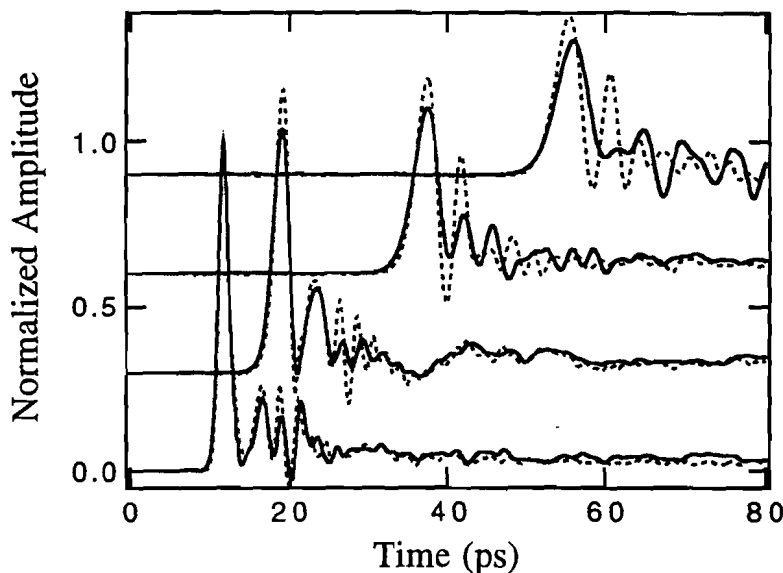
Fig. 6.3   Electrical pulses probed at 250 μm, 1, 3, and 5 mm on two straight CPWs with a ground-plane width of 500 (solid) and 50 μm (dotted).

A comparison of the waveforms on the two transmission lines in Fig. 6.3 reveals the clear superiority of the narrow ground CPW. Although the shape of the initial pulses on both lines is surprisingly similar, the signals on the wide-ground CPW suffer a larger reduction in peak amplitude, have a broader temporal width, and show reduced ringing. All three effects are evidence of increased loss, especially in the high frequency region. The fact that the last waveform on the wide-ground CPW shows no ringing is not due to reduced dispersion, but rather large high-frequency loss. When the high frequencies from the spectrum of the initial pulse are heavily attenuated, ringing disappears and the final pulse becomes wider. These findings are in agreement with the predictions of [3] where they suggest that a reduction of the ground plane width limits the leakage from the CPW mode to the substrate modes.

A close look of the measured waveforms, at propagation distances of 3 and 5 mm in Fig. 6.3, shows a small difference on the time at which each pulse peaks. If for the sake of simplicity, we assume that the pulse's peak specifies the arrival time of the signal at the measuring point, we can conclude that the wide-ground CPW is marginally slower. When the propagation distance in the narrow-ground line is plotted as function of arrival time (see Fig. 6.4—left axis), the familiar linear relationship is observed [4, 5]. However, the forward difference time-derivative of

propagation distance (Fig. 6.4—right axis) reveals that velocity is actually increasing as the signal travels along the line. This is consistent with the results in chapter 5.

The increase in the signal velocity *does not* imply that the transmission line exhibits nonlinear behavior. As we shall see in chapter 7 such lines can readily simulated by a linear model. The change in the signal velocity arises from the fact that the spectrum of the propagated pulse is getting progressively narrower. The reason is that high frequencies suffer comparatively higher losses, and as the signal travels down the CPW, its spectral content is confined to lower frequencies which travel at a higher speed. Because high frequency losses are higher in the wide-ground CPW, the propagation velocity increases at a faster pace, but as suggested by the results in Fig. 6.3, it levels off to a lower value. This is qualitatively consistent with the results of Gioni and Naldi [6] which suggest that a reduction of the ground plane width in a CPW causes a decrease in the quasistatic value of the effective dielectric permittivity which translates to an increase in signal velocity. However, the observed difference in speed is much larger than their prediction for CPWs such as ours.
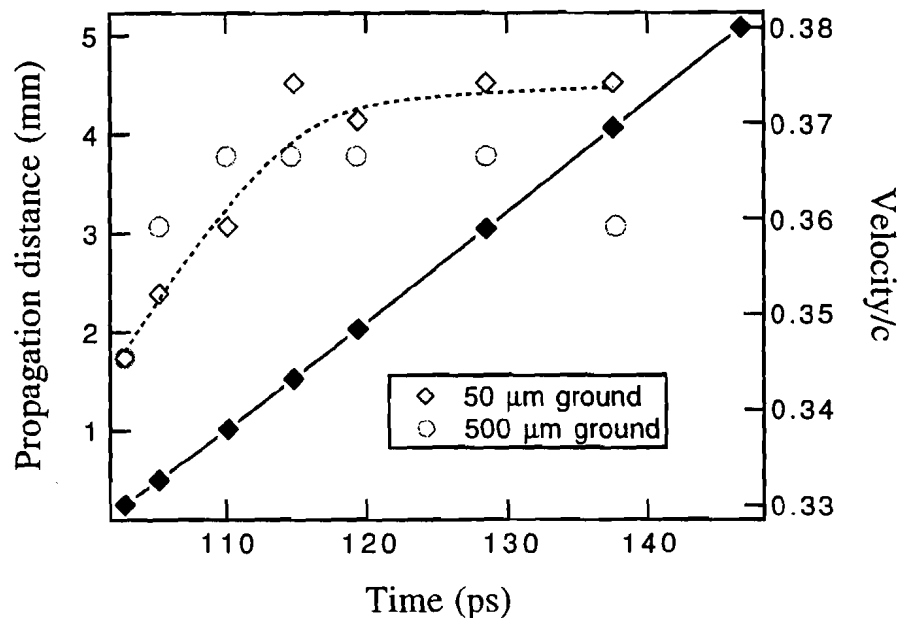
Fig. 6.4   Propagation distance as a function of arrival time for the pulses measured on a straight CPW with a ground plane width of 50 μm (solid line—left axis). The right axis shows the propagation velocity for this line and a wide-ground CPW. The dotted line is to guide the eye.

It would be of great interest to compare the propagation characteristics of a wide-ground CPW and a CPS, which quasistatically are reciprocal structures and

should exhibit identical behavior according to Gupta [7]. Figure 6.5 shows that when we overlay the waveforms measured on the two transmission lines, we observe strong similarities. In fact, the wide-ground CPW behaves more like the CPS rather than the
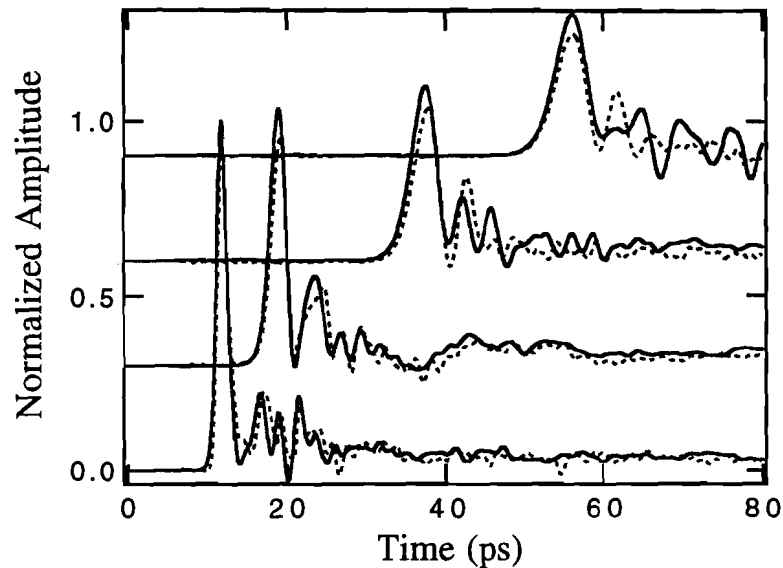
Fig. 6.5   Electrical pulses probed at 250 μm, 1, 3, and 5 mm on a 50 μm straight CPW with a ground-plane width of 500 (solid) and a 50 μm CPS (dotted).

narrow-ground CPW (see Fig. 6.3). There are some differences, since the spectrum of the propagated pulses far exceeds the substrate's cut-off frequency. The higher peak amplitude of the signal measured on the CPW suggests that low frequency losses are lower in this line. The stronger ringing on the waveforms measured on the CPS, on the other hand, indicates a better high frequency performance. Since the pulses on both lines have the same temporal width and exactly overlap with each other, it is safe to assume that their velocities are essentially the same.

6.2 Straight lines—10 μm technology

According to our analysis in chapter 3, a reduction of the transmission line lateral dimensions from 50 to 10 μm would reduce dispersion dramatically. High frequency loss, which is determined by radiation, should also be reduced, while low frequency loss, which is dominated by conductor losses, should increase. In order to test these assumptions, electrical pulses propagated on narrow-ground CPWs with line dimensions of 10 and 50 μm are overlaid in Fig. 6.6.
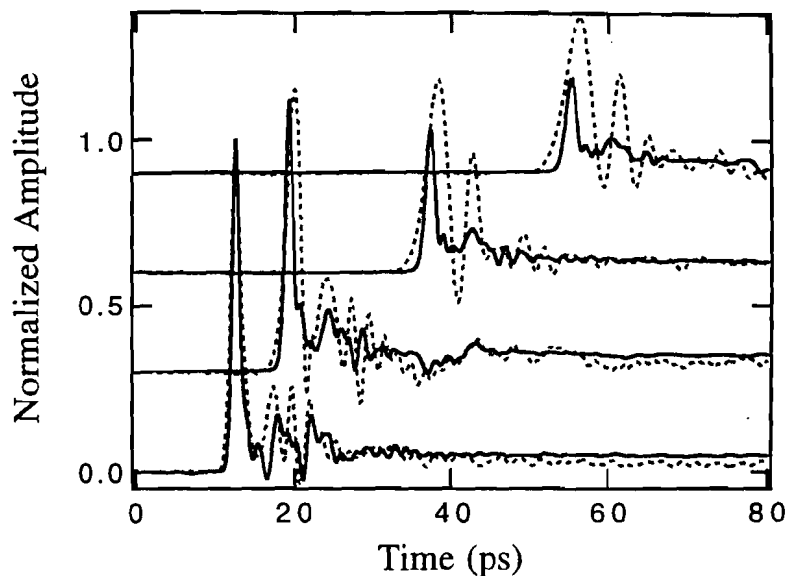
Fig. 6.6   Electrical pulses probed at 250 μm, 1, 3, and 5 mm on two straight CPWs with line dimensions of 10 (solid), and 50 μm (dotted). The ground plane width of each line is the same as its line dimensions.
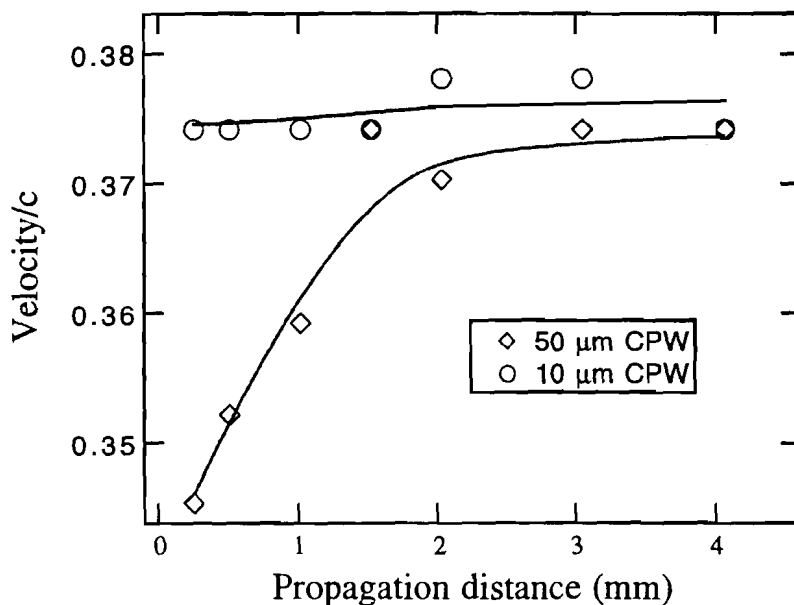
Fig. 6.7   Signal velocity as a function of propagation distance for two straight, narrow-ground CPWs with line dimensions of 10 and 50 μm. The ground plane width of each line is the same as its line dimensions.

The pulses probed at 250 μm from the switch are quite similar, with the waveform on the 10 μm line being slightly narrower. In contrast to the pulses on 50 μm line, the signals on the 10 μm CPW are only marginally broadened and show very

little ringing. This indicates that dispersion on this lines is much lower. The fact that the waveforms on the smaller line are faster even though they have a wider bandwidth further reinforces this conclusion. The evidence that dispersion in the 10 μm CPW is small can also be seen in Fig. 6.7. In contrast to the waveforms on the 50 μm CPWs, there is a very small change in velocity as the pulses travel along the 10 μm line. It then becomes clear that the characteristics of the signals on the smaller transmission lines are dominated by loss rather than dispersion.

For low-frequency loss, however, the situation is reversed. As the signals travel down the CPWs, their peak amplitude in the 10 μm line becomes substantially smaller. This difference is becoming more apparent after long propagation lengths where low frequencies become more important. For high frequency loss, the situation is less clear. Even though the narrower pulses in the 10 μm line indicate a large high frequency spectral content, the time-domain data can not at this point conclusively show that high frequency loss is indeed lower in this CPW.

A comparison between the waveforms propagated on 10 μm wide CPWs with narrow and wide ground plane widths of 500 and 10 μm, respectively (data not shown), indicates that the loss is substantially lower in the narrow-ground line. The velocity on this line is marginally higher while dispersion on both CPWs is limited.
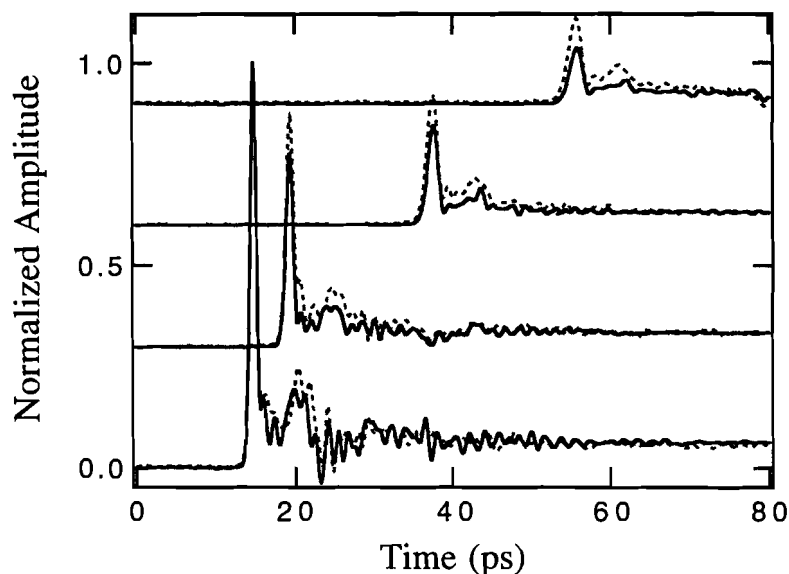
Fig. 6.8   Electrical pulses probed at 0.5, 1, 3, and 5 mm on a 10 μm straight CPW with a ground-plane width of 500 μm (solid), and a 10 μm CPS (dotted).

A similar comparison between the waveforms propagated on a 10 μm CPS and a CPW of the same dimensions, seen in Fig. 6.8, once more shows the strong similarity between the two transmission lines. The pulses are well timed at all measuring positions and their shape is almost identical. The main difference is that now the CPW shows stronger attenuation, in contrast to the 50 μm lines, where the CPS was more lossy.

6.3 Bent lines —50 μm technology
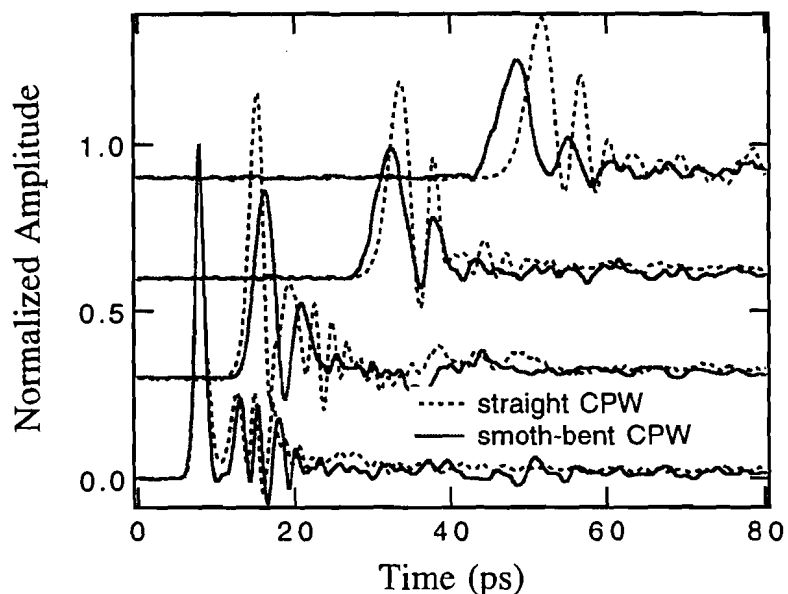
Fig. 6.9   Electrical pulses probed on a straight CPW at lengths of 0.25, 1, 3, and 5 mm, and a smooth-bent CPW after propagating through 0, 2, 6 and 10 bends. Each transmission line has lateral dimensions and a ground-plane width of 50 μm.

As we have seen from the straight line results, the ground-plane width of the CPW can affect the parameters of the transmission line significantly. The incorporation of bends in our lines is another parameter whose effect we would like to investigate. For this reason the pulses propagated on two CPWs, one straight—the other with smooth bents (lines 3 and 5 in Fig. 4.3), are plotted on Fig. 6. 9. The waveforms do not exactly overlap because the probing points are not identical. However, they are close enough to enable us derive conclusions about the

comparative performance of the lines. It is important to note that, because of the meander shape of the bent transmission lines, the radiation signal can now directly interfere with the main pulse and distort its shape. This effect can barley be seen on the two last waveforms in this figure but as we shall see further on it can become significantly more apparent.

Of course, everyone would expect that bends would degrade the propagation properties of the transmission lines. Figure 6.9 shows that the pulses propagated on the bent line are comparatively wider, have smaller peak amplitude and show less ringing. These observations show that the bends cause additional loss in the CPW. It seems, however, that as the propagation distance increases and the spectrum of the pulses becomes narrower, the signal on the two lines tend to become more similar. This suggests that the bends primarily affect the high frequencies.
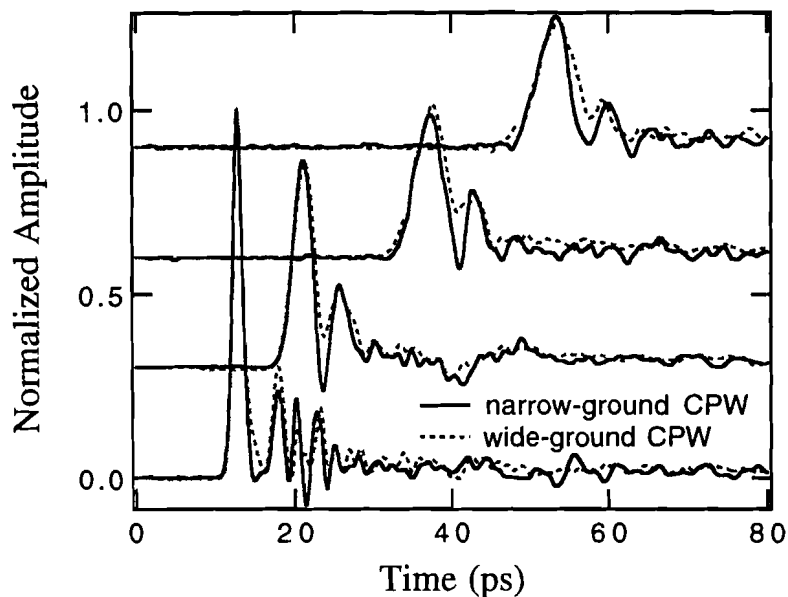
Fig. 6.10   A comparison of the electrical pulses probed on two smooth-bent CPWs after propagating through 0, 2, 6 and 10 bends. One transmission line has a ground-plane width of 50 and the other 500 μm (line 5 in Fig. 4. 3 and 4.7).

We have studied the effect of the ground plane width in 50 μm CPWs in the first section of this chapter (Fig. 6.3). If the same comparison is carried out for the smooth-bent lines, as shown in Fig. 6.10, we note some important differences. First, the waveforms propagated on the bent lines exactly overlap and have the same peak amplitude. This indicates that the low frequency loss is in this case dominated by the

bends. The width of the ground plane seems to dominate the high frequency end of the spectrum. The stronger ringing and the slightly narrower pulses on the narrow-ground transmission line suggest that the high frequency loss in this CPW is lower—a conclusion we also reached with the straight lines.
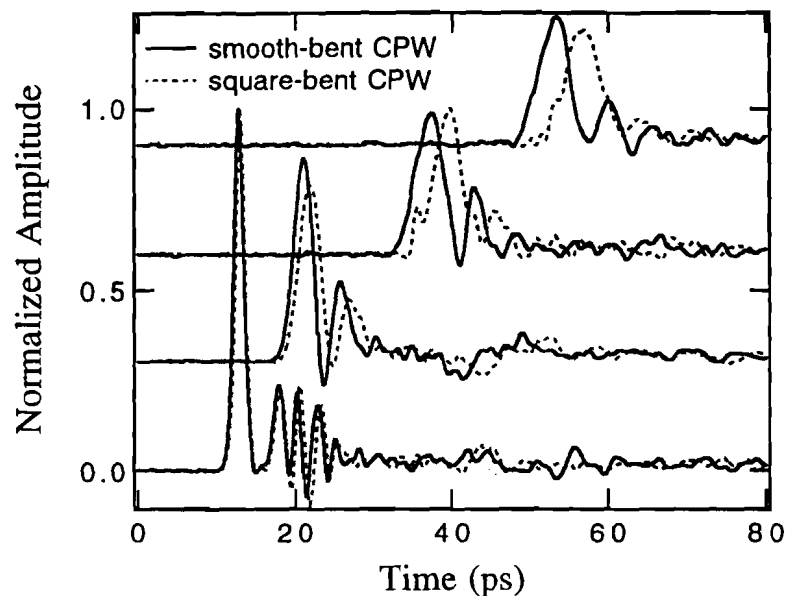
Fig. 6.11   Electrical waveforms measured on two bent CPWs after propagating through 0, 2, 6 and 10 bends. Both transmission lines have a ground-plane width of 50 μm (lines 4 and 5 in Fig. 4. 3).

The bend geometry also has an effect on the propagation characteristics of the CPWs. Figure 6.11 shows that the smooth bends allow comparatively larger pulses to propagate, indicating lower loss. As the pulses move away from the excitation site, the difference between the two bend geometries gets progressively smaller, and only high frequency ringing distinguishes the two sets of waveforms. These results suggest that both bends are indistinguishable to low frequency signals and only at high frequencies do the benefits of the smooth bend become clear.

A similar comparison between the waveforms propagated on a 50 μm CPS with smooth bends and a wide-ground CPW with the same dimensions (data not shown) demonstrates that there is only a small difference in the behavior of these lines. Like the corresponding straight lines shown in Fig. 6.5, the bent CPW suffers less loss, but now this difference is more apparent. In addition, the signals in the bent

CPS carry a relatively large amount of radiation since in this line it is not possible to reduce the radiation content by considering the odd mode signal only.

6.4 Bent lines —10 μm technology

Before shifting our analysis to the 10 μm bent lines, we have to bring to our attention that in these transmission lines the bends only cover a tenth of the total propagation length. For the 50 μm lines, this ratio is 0.5, eventhough the meander period is the same. For this reason, the characteristics of the 10 μm bent lines are excepted to deviate less from the performance of the corresponding straight lines.
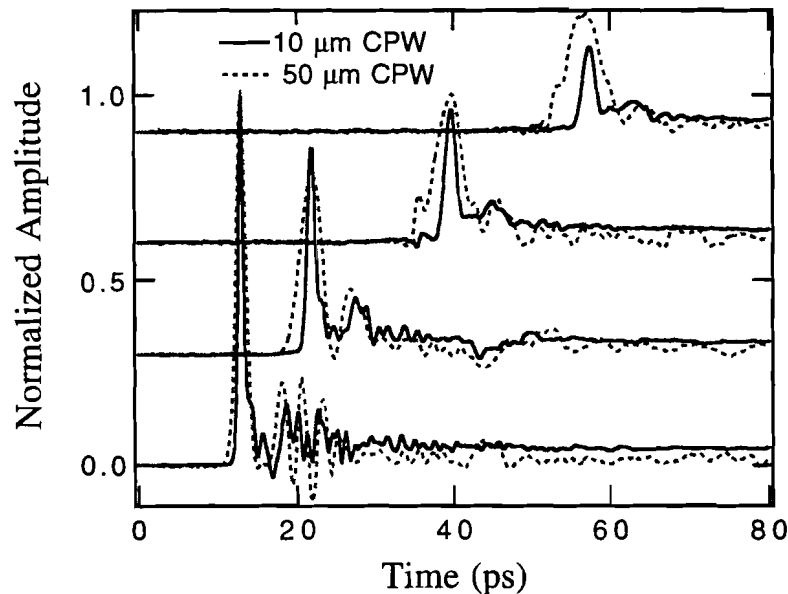
Fig. 6.12   Electrical waveforms measured on two square-bent CPWs with narrow ground planes after propagating through 0, 2, 6 and 10 bends (lines 4 in Fig. 4.3, and Fig. 4.6).

Figure 6.12 shows the pulses propagated on two meander type CPWs with square bends and narrow ground planes. The pulses on the 10 μm line are readily distinguishable, since having suffered much less dispersion, they have a significantly shorter temporal width. At long propagation distances, where the signal bandwidth deteriorates and the bends become less important, the 50 μm line may still have more dispersion but it is clearly less lossy. Closer to the excitation site, on the other hand,

attenuation is lower in the 10 μm line. This effect was also observed in the straight lines (Fig. 6.6), but now it is further enhanced by the presence of the bends which primarily influence the high frequency end of the spectrum. A similar comparison between 10 and 50 μm CPS reveals almost identical results.
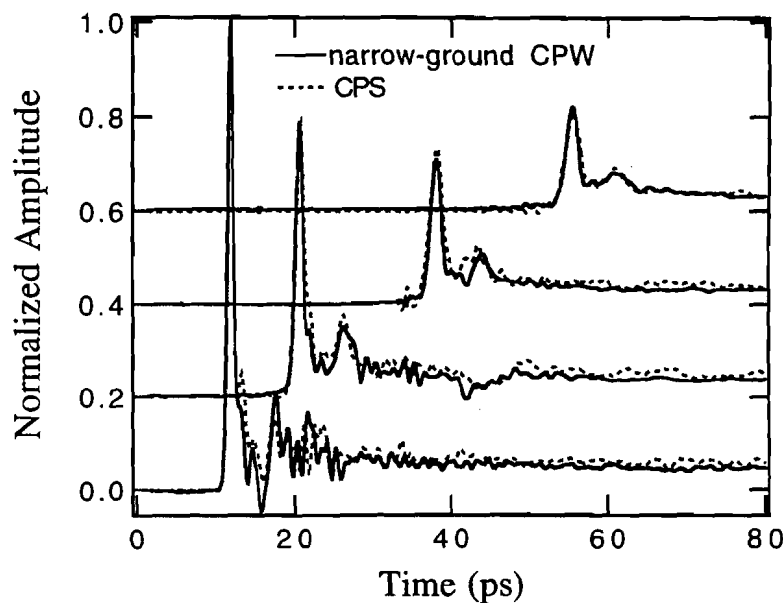
Fig. 6.13   A comparison of the waveforms probed after propagating through 0, 2, 6 and 10 bends on smooth-bent CPW and CPS with 10 μm lateral dimensions.

Since a 10 μm CPW with smooth bends and a wide ground was not included in our mask set, in Fig. 6.13 we compared a narrow-ground line to a CPS of the same geometry. The plots show an impressive similarity between the two transmission lines. The two sets of pulses exactly overlap, indicating identical velocities. Moreover the peak amplitude and pulse width are almost exactly matched. One would expect the CPS to have higher loss, since quasistatically its performance is comparable to a wide-ground CPW which so far has exhibited inferior characteristics. Nevertheless, this appears not to be true for the 10 μm bent lines. The waveforms sampled on the square-bent CPW (see Fig. 6. 14) are also strongly similar to the two sets of pulses displayed in Fig. 6. 13. This suggests that for 10 μm lines, the bend geometry has a little effect on the properties of the transmission lines. This evidence is further enhanced by the waveforms in Fig. 6. 14.
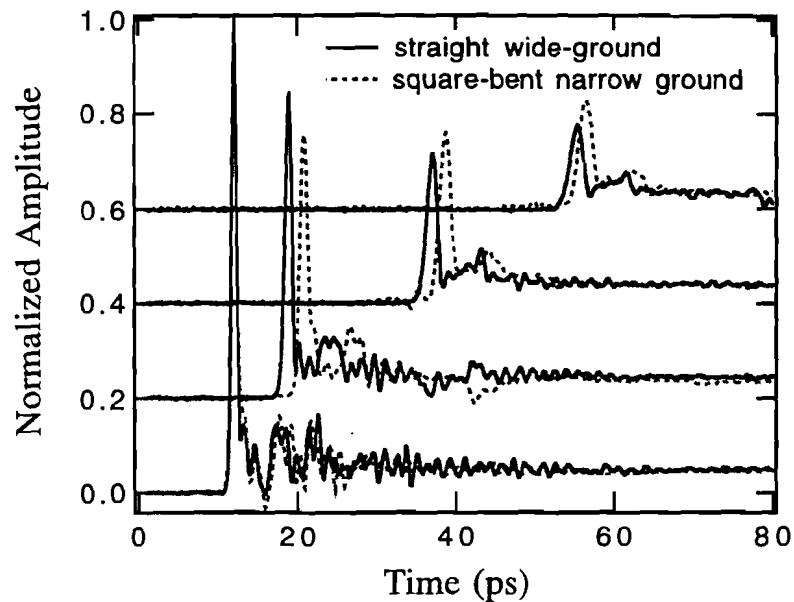
Fig. 6.14   Electrical pulses sampled on a smooth-bent CPW with a narrow ground and a straight CPW with wide ground. The waveforms have traveled 0.25, 1, 3, and 5 mm on the straight line and 0, 2, 6 and 10 bents on the meander line.

In order to demonstrate which geometrical feature dominates the transmission line characteristics, the waveforms measured on two 10-μm CPWs with distinctly different geometries, are displayed in Figure 6.14. One line is straight and has a narrow ground plane width of 10 μm, while the other is a meander-type line with smooth bends and a ground plane width of 500 μm. The waveforms in this figure show that for short propagation distances the straight line has lower attenuation. However, as the signals travel away from the excitation site, the situation is reversed and the bent line demonstrates superior performance. It then seems reasonable to conclude that the bends dominate the very high frequency behavior of the 10-μm CPWs, while the ground plane width is more important for lower frequencies. What is really surprising from this analysis is that, if one wishes to propagate signals for more than 2 mm in these lines, she is better off using the narrow-ground bent-line rather than the straight line with the wide ground, because the bent line also relaxes the layout requirements and requires less chip area.

It is relatively easy to compare the signal velocities in the straight lines because the measuring points are exactly matched. For the bent lines, this is not always possible because of the different bent geometries used. In order to give a more

rounded description of speed in our transmission lines it would be more convenient to focus our attention to table 6.1 which gives the average signal propagation velocity in all transmission lines discussed in this chapter.

Transmission line	Geometry	Velocity % of c
50 μm CPW	straight, narrow-ground	36.9
50 μm CPW	straight, wide-ground	36.4
50 μm CPS	straight	36.4
10 μm CPW	straight, narrow-ground	37.6
10 μm CPW	straight, wide-ground	37.2
10 μm CPS	straight	37.2
50 μm CPW	square bent, narrow-ground	38.7
50 μm CPW	smooth bent, narrow-ground	37.4
50 μm CPW	smooth bent, wide-ground	37.3
50 μm CPS	smooth bent	37.5
10 μm CPW	square bent, narrow-ground	37.8
10 μm CPW	smooth bent, narrow-ground	37.7
10 μm CPS	smooth bent	37.7

Table 6.1   The propagation velocity in each transmission line depends on its lateral dimensions and geometry. The figures on velocity represent its average value on each line.

As we have already seen in Fig. 6.4 and 6.7, the propagation velocity in each line depends both on its features and the bandwidth of the traveling signals. For the 50 μm lines, which are far more dispersive, velocity increases significantly as the propagation distance is increased and the high frequency part of the spectrum is lost. This effect is much less evident in the 10 μm lines. The presence of the bents in the transmission lines forces the signal velocity to increase at a faster pace since the high frequency loss is enhanced. Further, the speed on the bent lines was measured for pulses that propagated longer distances (more than 9 mm compared to ~5 mm in the straight lines). For these reasons, the velocity on the bent transmission lines is

generally expected to be higher. The velocity in all lines is still a bit lower than the quasistatic value of 37.9 % of c (Eq. 3.2 with $\varepsilon_r = 12.9$) mainly because most of the pulse's spectrum is above the substrate's cut-off frequency.

However, the above observation is not true for the 50 μm square-bent CPW whose velocity is by more than 1 % of c higher than the corresponding smooth-bent CPW. Moreover, the observed value of velocity is even higher than the quasistatic value. These findings supports the idea that the effective length of the square bent is shorter than the actual geometrical length [8]. If we assume that the speed of the square and smooth-bent lines is the same, then the difference between the actual and effective bend length is about 6 %. This small difference is a refinement of our initial conclusion [4, 5] that the effective length of the bend is given by its geometrical length.

The straight line results have shown that a reduction of the ground-plane width is causing an increase in the signal velocity by 0.5% of c. As we have already mentioned in section 1, this is qualitatively in agreement with Ref. 6, but the observed difference is much larger than their predictions. No such difference in speed is observed in the bent lines, however. This may have to do with the way we define the arrival time (location of the pulse's peak) for the calculation of propagation velocity. Spectral analysis, which treats each frequency separately, could refine the conclusions extracted from the time domain results.

.

6.5 Odd and even modes after the curved bend

In chapter 5 we have seen that as the signal travels trough a bend the even mode is excited [9]. This effect is observed as a temporal difference between the waveforms in the two slots. Since the geometry of the meander lines did not provide sufficient length after each bend for these measurements, the study of the evolution of the odd and even modes was not practical. For this reason we fabricated the structure shown in Fig. 6.15. This CPW enables the study of the even mode under three separate conditions. The first is the well known excitation of the even mode by the bend just after the switch, and will be investigated in this section. As the signals travel down the line and reach the asymmetric T-junction, they can either continue in the same direction, or turn right, pass through the second bend, and propagate in the

opposite direction. The two cases are distinctly different because the signal in the in top slot sees only a discontinued path, while in the signal in the bottom slot sees both a discontinued path and an extra propagation length. The latter cases are examined in the next section.
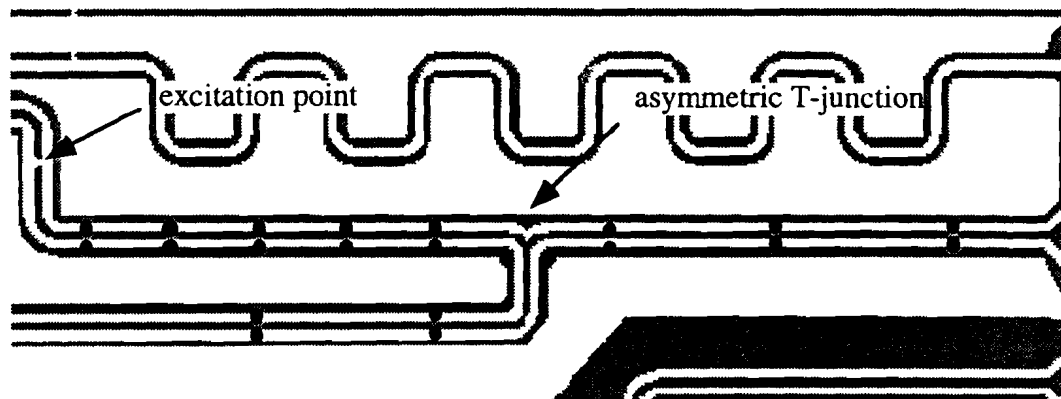
Fig. 6.15   In order to study the odd and even modes, the signals propagated on a CPW were measured after a single smooth bend at the indicated positions. For some measurements the grounds were connected with wirebonds at the edges of the bend. Some the transmission line features may appear coarse because of the limited resolution of this image.
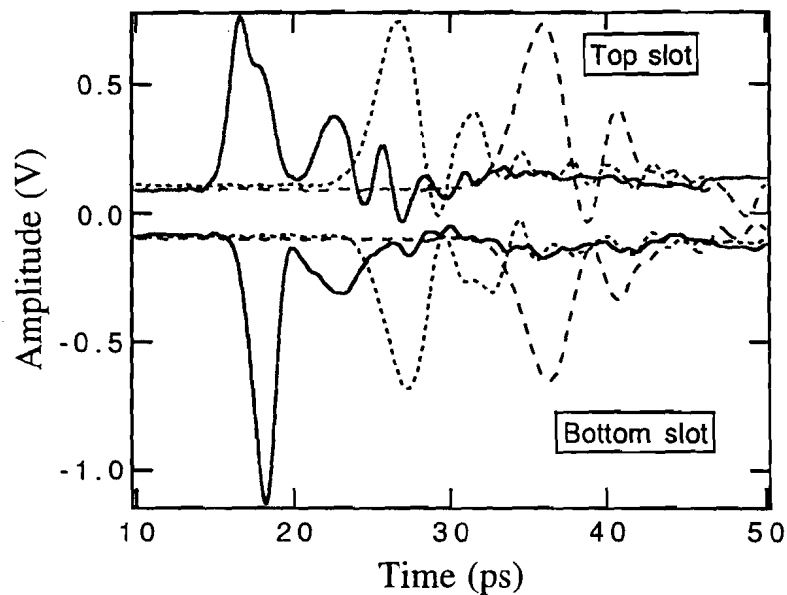
Fig. 6. 16   Electrical waveforms probed in the two slots of the 50 µm CPW after propagating through a smooth bend with no wirebonds. The propagation distances are approximately 0.15, 1 and 2 mm and are measured from the end of the bend.

In chapter 5 we have seen that the connection of the ground planes with wirebonds at the vicinity of the bend, reduces the even mode excitation significantly. The influence of wirebonds will also be studied in detail, in the structure shown in Fig. 6.15, and the results will be compared to the case no wirebonds were used.

In Fig. 6.16 we display the pulses that were measured after the signals traveled through the first bend, but before they reached the T-junction. These measurements were taken with no wirebonds between the grounds of the bend. The pulses are distinctly different from the ones sampled on the straight lines. The first pulse in the bottom slot is visibly delayed because of the longer slot length, and its amplitude is much larger than the corresponding pulse in the top slot. Moreover, the first pulse in the top slot has a small, secondary peak which is timed with the delayed pulse in the bottom slot. However, the difference between the signals in the two slots is quickly smoothed-out and they appear surprisingly similar after propagating a distance of approximately 2 mm. Alternatively, it appears that the pulse amplitude reduction is very high in the bottom slot and almost nonexistent in the top slot.
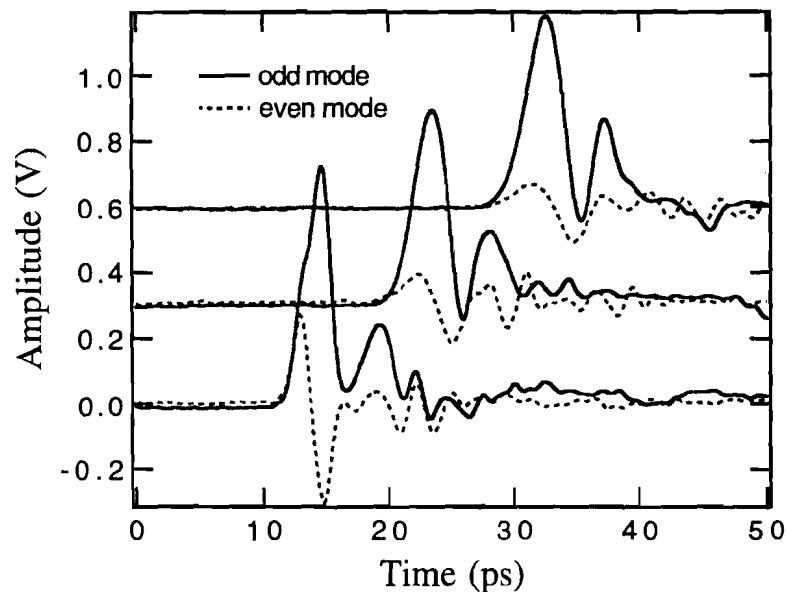
Fig. 6. 17   The signals in Fig. 6.16 resolved to their odd and even mode content.

If the odd and even mode signal (i.e. the sum and difference between the waveforms in each slot, respectively) are considered separately, the situation becomes far simpler. As can be seen in Fig. 6.17, the odd-mode signal is much larger. In close

agreement with the straight line results seen in Fig. 6.3, the peak amplitude reduction is low. Ringing is less evident now, but as we have seen in the previous section, this is primarily because the bend is especially lossy at high frequencies. The even-mode signal, on the other hand, behaves very differently. The reduction in peak amplitude is very strong, especially between the first and second waveforms. Over a distance of 1 mm, the even mode signal is reduced by more than 50 % and quickly becomes about a tenth of the odd-mode signal. This is primarily due to the fact that the even-mode signal has a proportionally larger high frequency content. Moreover, since this signal is bipolar in nature, the very low frequencies, which suffer little loss, are completely absent. In addition, the even-mode signal has a propagation mode which corresponds to a CPS defined by the two ground conductors [4, 10]. Because this line is 100 μm wider than the CPW, the radiation loss for the even mode is enhanced by a factor of 2. The large attenuation of the even mode-signal is decreasing the even to odd mode ratio of the signal in each slot, and as the waveforms in each slot travel down the straight section of the line, they become almost identical.
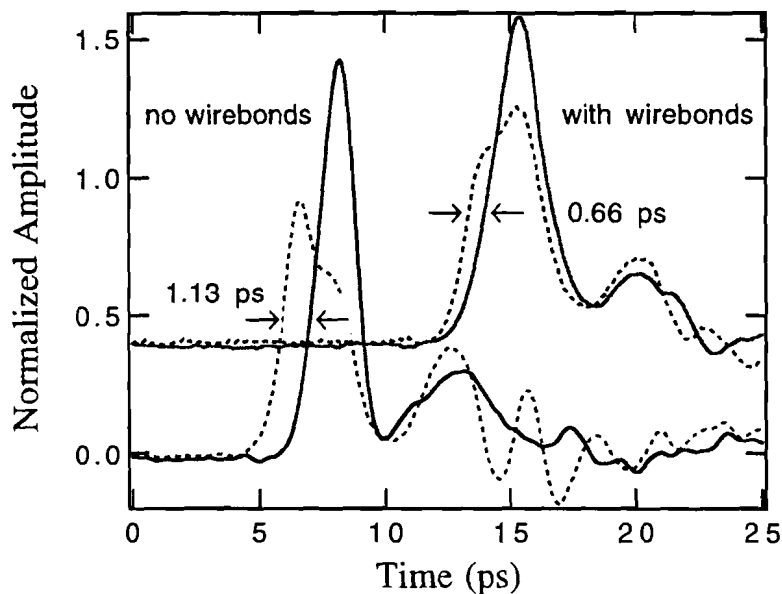
Fig. 6.18   The signals in the two slots of the CPW are significantly affected by the wirebonds. The pulses are sampled 150 μm from the bend and are normalized with respect to the odd-mode signal at that location. The time axis is shifted.

If wirebonds are used to connect the CPW grounds at the boundaries of the bend, the pulses measured immediately after are changed significantly (see Fig. 6.18).

However, as the pulses propagate on the straight section of the line, they again become increasingly symmetric (waveforms not shown). The wirebonds seem to reduce the relative time delay between the signals in each slot substantially. The small secondary peak in the leading waveform timed with the lagging pulse, is now visibly enlarged and becomes the main pulse peak. The difference in amplitude is also reduced, but only at the expense of bandwidth, since the waveforms are broadened. It seems that the wirebonds have an "averaging effect" on the waveforms in both amplitude and time. Thus, the signals in each slot become more similar, but also wider. Alternatively, this means that the even mode signal is reduced.
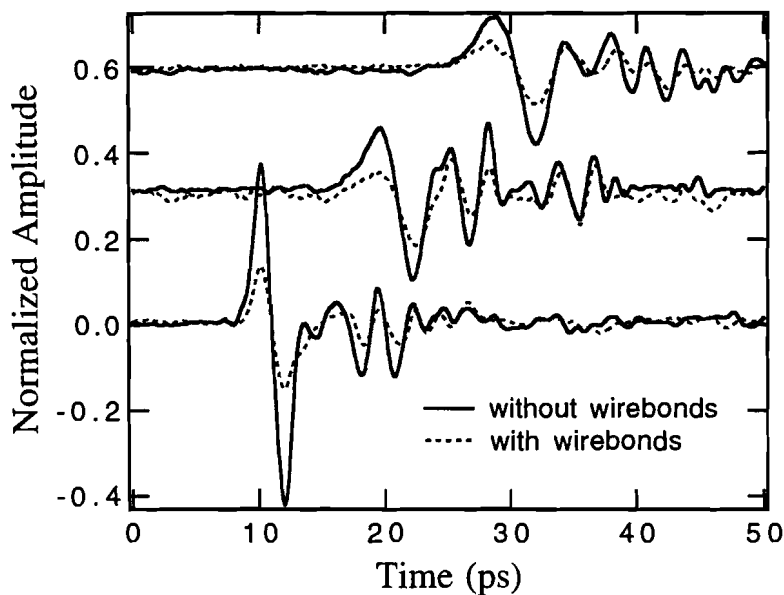
Fig. 6.19   The effect of wirebonds on the evolution of the even-mode signals. The waveforms were extracted from pulses measured at 0.15, 1, and 2 mm from the bend, and are normalized with respect to the odd-mode signal.

The effect of the wirebonds on the even mode signal is shown in Fig. 6.19. A comparison between the two sets of signals clearly demonstrates that the wirebonds reduce the even mode signal drastically. The reason the even mode is not completely eliminated, is that frequencies in the neighborhood of a 100 GHz and above, the wirebond impedance has a value of several Ohms. In either case however (wirebonds, or no wire bonds), the even-mode signal quickly becomes a small fraction of the odd-mode signal.

It seems that the velocity of the odd-mode signals is not affected by the wirebonds and closely matches the velocity of the straight CPW with narrow grounds. The velocity of the even-mode, on the other hand, depends on the reference point we use to define the arrival time. If the minimum of the waveforms in Fig. 6.19 is chosen, the speed appears to be significantly lower (by ~3 % of c). If the maximum of the waveforms is used the velocity is only 0.5 % of c lower. The reason is that the minimum of the waveforms is dominated by high frequencies which are even slower for even mode propagation.

6.6 Odd and even modes after the T-junction
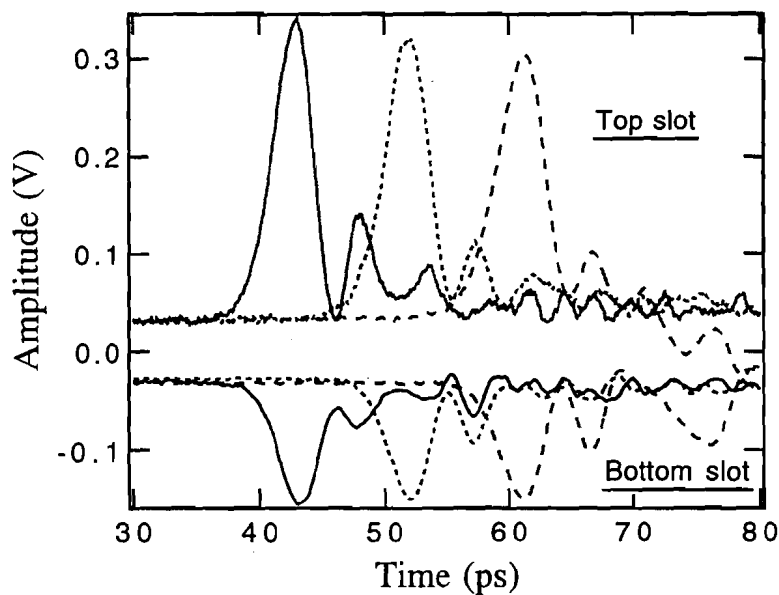
Fig. 6.20   Electrical waveforms probed in the two slots of the 50 μm CPW after propagating through the asymmetric T-junction (right site in Fig. 6.15).

A study of the signals propagated through the T-junction (measurement positions to the right site of the junction in Fig. 6.15) reveals larger differences in the amplitude of the pulses in each slot, as shown in Fig. 6.20. Eventhough the pulses in each slot are timed and have the same shape, the signal amplitude is much larger in the top slot because it is continuous over the length of the T-junction. In contrast to the signal measured immediately after the bend, these pulses preserve their

asymmetry for large propagation lengths. In order to understand this apparent change in the evolution of the waveforms we consider the odd and even mode signal separately in Fig. 6.21.
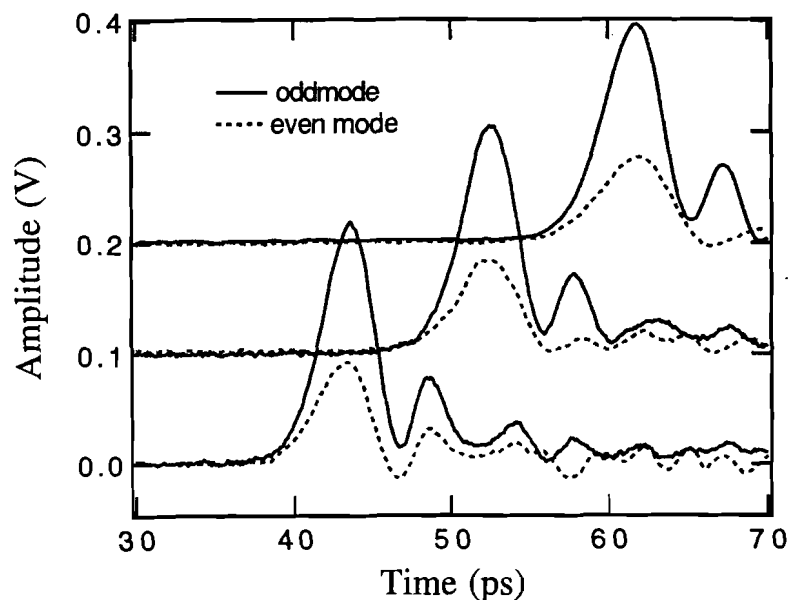
Fig. 6.21   The odd and even mode content of the signals shown in Fig. 6.20.

In spite of the fact that the top slot of the T-junction is completely discontinued, the amplitude of the odd-mode signal is still larger than the even-mode signal by more than a factor of 2. This is another indication of the strong coupling between the two slots of the transmission line—it is after all a CPW. A comparison between Fig. 6.17 and 21 shows that, apart from the added dispersion, there is a little difference between the odd-mode signals before and after the T-junction. The even-mode signals, however, are very different after the junction. Since there in no delay between the signals in each slot, the even mode in now unipolar and its frequency content is similar to the odd mode. The even-mode signal can now persist for long distances because its unipolar shape contains a lot of energy at very low frequencies which suffer little attenuation. Only ringing is drastically reduced, because it is dominated by high frequencies which are experience larger loss. The even to odd mode ratio in Fig. 6.21 is still reduced as the propagation distance is increased because the odd mode is still less lossy, but this difference is now only marginal. For

this reason in Fig. 6.20, the signals in the two slots of the transmission line retain their amplitude asymmetry.

The discontinuities that were used to excite the even mode in the two geometries, are relatively mild compared to the combination of the T-junction and the second bend. As we have already mentioned in the beginning of section 5, the signals not only have to phase a discontinued path, but also a large temporal shift arising from the difference in the path length of the two slots. The waveforms measured in this region (left-bottom section in Fig. 6.15) are shown in Fig. 6.22. The radiation emitted from the excitation site is a much bigger problem for these signals because the reversal in the propagation direction is causing a direct overlap. Another interesting point to remember is that the first radiation signal (between 30 and 35 ps in Fig. 6.22) is clearly common mode, reinforcing the our observations in the beginning of the first section of this chapter.
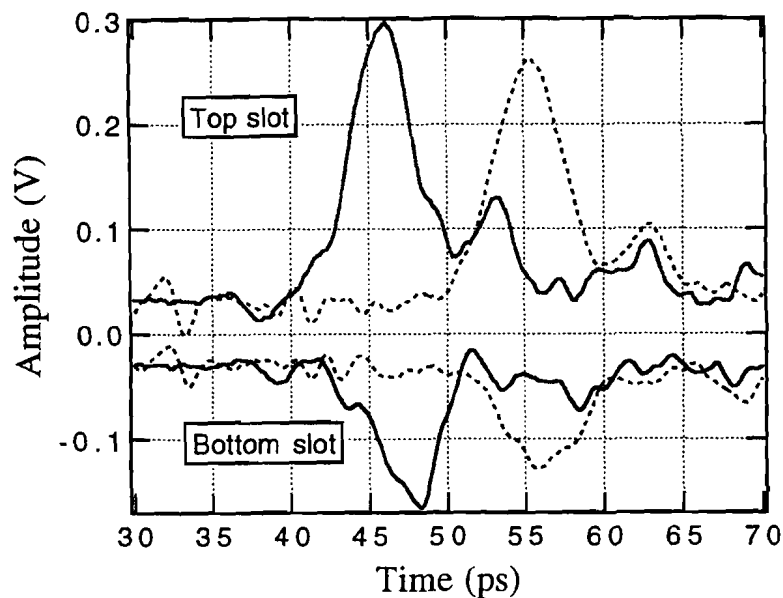
Fig. 6.22   Electrical waveforms probed in the two slots of the 50 μm CPW after propagating through the asymmetric T-junction and a second smooth bend with no wirebonds (bottom-left site in Fig. 6.15).

The main signals in the two slots are, as expected, very asymmetric in amplitude. Moreover, there is initially a large time difference between the time the pulses in each slot peak. The time difference is more than 2.2 ps between the first set of pulses but reduces to about 0.6 ps between the second set. This gives the

impression that the signal in the top slot waits for the signal in the bottom slot to catch up. In order to better understand this effect we resolve these waveforms to their odd and even mode content in Fig. 6.23.
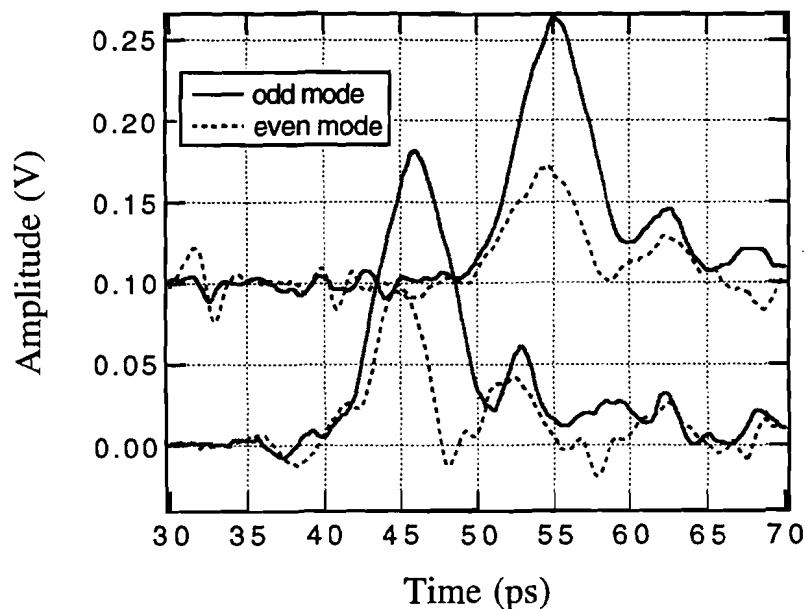
Fig. 6.23   The signals shown in Fig. 6.22 resolved to their odd and even mode content.

The noise in the odd-mode signals in Fig. 6.23 is substantially reduced compared to the waveforms in Fig. 6.22. The even-mode signals, however, still include some peculiar features induced by radiation. All waveforms are significantly dispersed but high frequency ringing is limited. It appears that the peak of the even-mode signal travels faster than the odd (by ~0.5 ps over a distance of 1 mm). This is much less than the 1.6 ps difference between the signals in the two slots, nevertheless, it is clearly an artifact induced by radiation because the even mode signal should actually be slower. The reason that the signals in the two slots tend to approach each other, is not that they travel at different speeds, but rather that the amplitude of the even-mode signal is significantly reduced while the odd-mode signal is practically unchanged.

Summary

This chapter presented a primarily quantitative analysis of the propagation of picosecond pulses on a family of wide bandwidth coplanar transmission lines. The characteristics of straight and bend lines with various geometries were studied in detail. The excitation of the even mode at various discontinuities was thoroughly investigated for the first time. Our analysis enabled us to reach a number of important conclusions given below.

- For initial electrical pulses of picosecond duration and over a distance of several millimeters, the 50 μm lines are dominated by dispersion and the 10 μm lines by loss.

- A reduction of the ground plane width in CPWs reduces both loss and dispersion significantly.

- The characteristics of CPWs and CPSs are comparable up to very high frequencies.

- The bends degrade the performance of the transmission lines but only at very high frequencies where a smooth geometry becomes advantageous.

- All transmission lines, straight and bent, have approximately the same propagation velocity, but small differences do occur.

- In 10 μm lines, the very high frequencies are dominated by the bends but for rest of the spectrum the ground plane width is more important.

- The excitation of the even mode at discontinuities can effectively be eliminated by wirebonds, but only at low frequencies.

- Because the even mode suffers dramatically increased losses, the high frequency signal asymmetries are only important at very short distances.

- Unipolar even-mode signals are far more persistent than bipolar signals because of their large low frequency content.

References

[1] D. Grischkowsky, I. N. Duling, III, J. C. Chen, and C.-C. Chi, "Electromagnetic shock waves from transmission lines," *Phys. Rev. Lett.*, vol. 59, pp. 1663–1666, Oct. 1987.

[2] S. Alexandrou, C.-C. Wang, R. Sobolewski, and T. Y. Hsiang, "Generation of Subpicosecond Electrical Pulses by Nonuniform Illumination of GaAs Transmission Line Gaps," to appear in the *IEEE JQE*.

Also S. Alexandrou, C.-C. Wang, R. Sobolewski, and T. Y. Hsiang, "Subpicosecond Electrical Pulse Generation in GaAs by Nonuniform Illumination of Series and Parallel Transmission Line Gaps," OSA Proceedings on Ultrafast Electronics and Optoelectronics, S. Shah and U. Mishra, eds., vol. 14, pp. 209-212, 1993.

[3] M. Tsuji, H. Shigesawa, and A. A. Oliner, "New coplanar leakage behavior on coplanar waveguides of finite and infinite widths,"*IEEE MTT.*, vol. 39, No. 12, pp. 2130-2237, December 1991.

[4] S.Alexandrou, R.Sobolewski, and T.Y.Hsiang, "Time-domain characterization of bent coplanar waveguides," *IEEE JQE.*, vol. 28, pp. 2325-2332, October 1992.

[5] S. Alexandrou, R. Sobolewski, H. Nakano, B. C. Tousley, and T. Y. Hsiang, "Picosecond Characterization of Bent Coplanar Waveguides," *IEEE Microwave and Guided Wave Lett.*, vol. 1, pp. 236–238, September 1991.

[6] G. Goine and C. U. Naldi, "Coplanar waveguide for MMIC applications: effect of upper shielding, conductor backing, finite-extent ground planes, and line-to-line coupling," *IEEE MTT.*, vol. 35, No. 3, pp. 260-267, March 1987.

[7] K. C. Gupta, R. Garg, and I. J. Bahl, "Microstrip lines and slotlines," Norwood, MA, *Artech House*, 1979.

[8] R. N. Simonns, G. E. Ponchak, K. S. Martzaklis, and R. R. Romanofsky, "Channelized coplanar waveguide; discontinuities, junctions, and propagation characteristics," *IEEE Int. Sump. Digest*, pp. 915–918, 1989.

Also, R. N. Simonns and G. E. Ponchak, "Modeling of some coplanar waveguide discontinuities," *IEEE MTT.*, vol. 36, No. 1796-1803, December 1988.

[9]   S. Alexandrou, R. Sobolewski, and T. Y. Hsiang, "Bend-Induced Even and Odd Modes in Picosecond Electrical Transients Propagated on a Coplanar Waveguide," *Appl. Phys. Lett.*, vol. 60, pp. 1836–1838, April 1992.

[10]   T. Itoh, Ed., *Planar Transmission Line Structures*. New York: IEEE Press, 1987, p. 253.

7. Spectral analysis

In chapter 6 we presented a primarily qualitative, time-domain analysis of our test transmission lines based on a study of the evolution of picosecond pulses. In this chapter the same experimental data will be used to extract the frequency dependent parameters of each line through spectral analysis. In contrast to the time-domain studies, the spectral analysis will be provide a complete, *quantitative* description of the transmission lines.

Much has been said in recent years about the prospects of using time-domain pulse experiments to carry out broad-band spectral analysis. The results presented in this chapter, however, is the first time that comprehensive frequency domain analysis is demonstrated in the THz range. The convenient availability of picosecond electrical pulses (as opposed to step-like waveforms) in conjunction with electro-optic sampling is instrumental in the realization of broad-band analysis. The third element — proper processing of the experimental data, is also essential. For this reason this chapter begins with the fundamental aspects of frequency-domain analysis.

The following sections focus on the description of the three separate sets of geometrical structures. Sections 2 and 3 were dedicated to the study of the straight lines. Different lines, such as CPWs with wide and narrow ground conductors, as well as, CPS were investigated, together with the effect of lateral dimensions on the transmission line characteristics. The influence of bends on the behavior of the lines was addressed in sections 4 and 5. Finally, sections 6 was dedicated to the study of the even mode excitation.

7.1 Fundamentals of spectral analysis

In order to carry out the spectral analysis for each transmission line we first have to convert our data from time domain to frequency domain. This can be done with the use of Fourier transform (see Eq. 7.1) which gives the frequency domain description, $V(f)$, of the time domain function $v(t)$. The two functions are, of course, equivalent representations of the data in each domain.

$$V(f) = \int_{-\infty}^{\infty} v(t)\, e^{-i2\pi f t}\, dt \qquad (7.1)$$

Once the data are expressed as functions of frequency, the results at each measurement position can be used to calculate the complex propagation factor γ given by equation 7.2. Since the transmission line is a linear system, γ can give a complete description the line. The real part of γ represents the attenuation of the signal as it travels along the transmission line (in the z direction), and the imaginary part β is inversely proportional to the phase velocity. As we have seen in chapter 3, the phase velocity depends on the effective permittivity of the transmission line, $\varepsilon_{eff}(f)$. The increase of $\varepsilon_{eff}(f)$ with frequency leads to signal dispersion. Our analysis in this chapter will focus on the experimental determination of α end ε_{eff} for each transmission line.

$$V(f,z) = V(f,0)\, e^{-\gamma(f)\, z} \qquad (7.2\ a)$$

$$\gamma(f) = \alpha(f) + j\, \beta(f) \qquad (7.2\ b)$$

$$v_{ph}(f) = \frac{2\pi f}{\beta(f)} = \frac{c}{\sqrt{\varepsilon_{eff}(f)}} \qquad (7.2\ c)$$

The experimental time-domain data, however, are discrete and consist of a given number of points which span a finite time window. For this reason, we used the Fast Fourier Transform (FFT) [1], instead of Eq. 7. 1, to convert the data into the frequency domain. The discrete nature of our data enforces a number of considerations which have to be taken into account for the correct implementation of spectral analysis. Lets first consider the example in Fig. 7.1, where a time domain

function is transformed to its spectral content. The width of the time window, Δt, determines the spacing between consecutive points in frequency domain, δf, through the relation $\delta f = 1/\Delta t$. Similarly, the spacing between consecutive points in the time domain, δt, defines the span of the spectral widow Δf, by the expression $\Delta f = 2/\delta t$. The latter equation is commonly referred to as the "Sampling theorem." It is of critical importance that the spectrum of the data falls well inside the frequency window Δf, otherwise the energy of frequencies outside Δf is transferred into the measuring window and the spectrum is distorted. For this reason the experimental time domain data consist of 1024 points spanning a window of 100 ps. This translates to 513 points in the frequency domain covering a bandwidth of 5 THz. Since the whole spectrum of the propagating waveforms is limited to frequencies less than 1.5 THz, frequency spilling is avoided. In some cases additional zeros have been attached to the experimental data to increase the total time span to 400 ps. This was done to reduce the truncation error on the phase function.
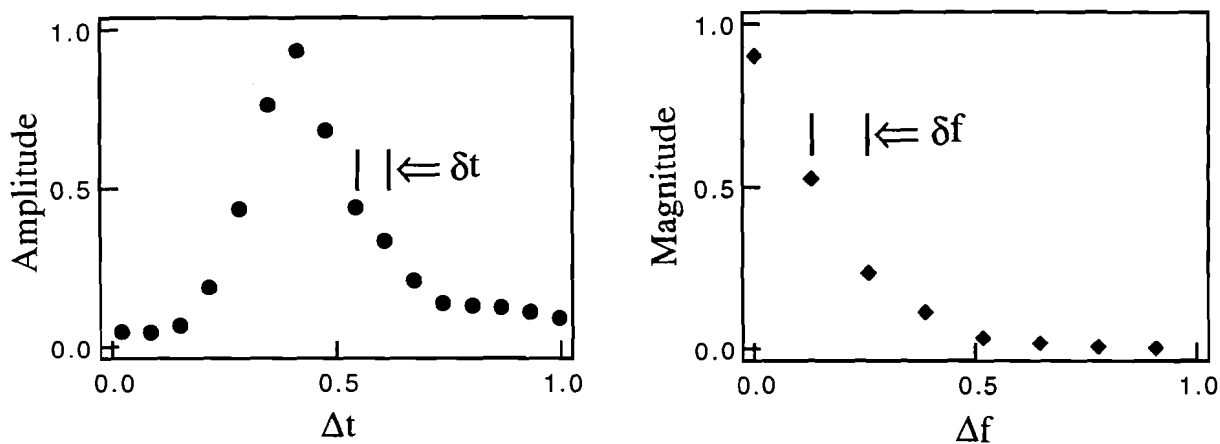
Fig. 7.1   An FFT transformation of a discrete function from the time domain (left) to the frequency domain (right). For simplicity, only the positive frequencies are included and the phase of the spectrum is omitted.

Another issue that has to be addressed is the shape of the gating time window. In the example above a square pulse, with an amplitude of 1 inside the time interval Δt and zero outside, is used to gate the time domain data. However, the steep rise and fall of a square gating function can distort the transformed spectrum and cause "frequency spilling" [1]. This problem can be solved with the choice of a smoother gating function, such as a Gaussian or a Hanning window.

Top plot: Amplitude (V) vs Time (ps)

Legend:
- data
- $e^{-(t/30)^4}$
- $e^{-(t/150)^4}$

Bottom plot: Magnitude (rel. units) vs Frequency (GHz)

Legend:
- spectrum of gated pulse
- spectrum of gating function
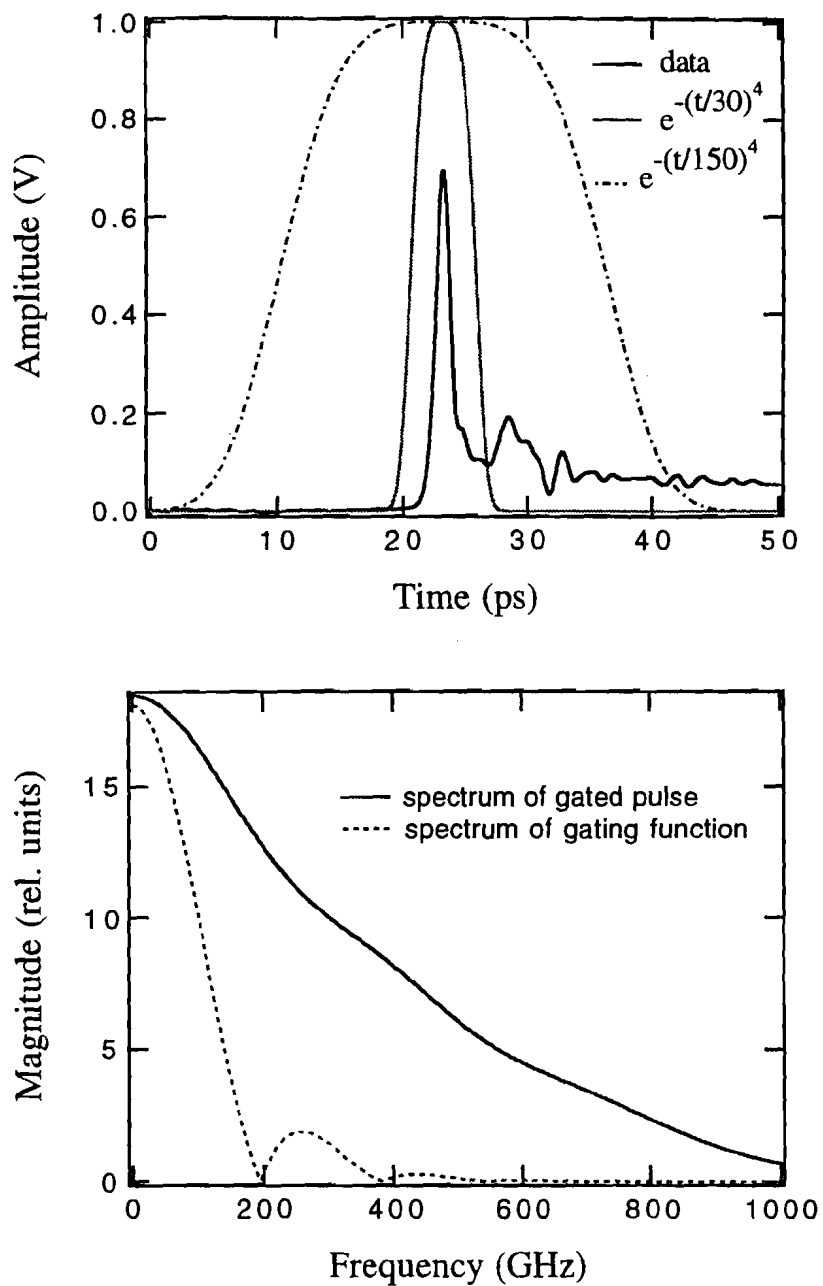
Fig. 7.2   Top—Experimental data probed on a 10 μm CPW together with a wide and a narrow gating function.

Bottom— A comparison of the spectrum of the experimental data above with the spectrum of the narrow gating function [$e^{-(t/30)4}$]. This was the narrowest function used in our analysis and it represents a worst case scenario.

A visual inspection of the experimental results in chapter 6, a representative sample of which can be seen in Fig. 7.2, shows that apart from the stray radiation

signal there is also a small shoulder that follows the propagating pulse. A smooth gating function can take care of the shoulder but the problem of radiation still remains. Radiation can be limited with the use of a narrower gating function which selects only the picosecond pulse from the time domain data. Such a function, however, has a broader spectrum which not only increases frequency spilling, but also limits low frequency information. For this reason a compromise has to be reached which also has to account for the characteristics of the variables we are trying to measure (α, ε_{eff}). In the following sections we will show that the 10 μm lines have properties that vary slowly with frequency. This enables us to use narrow gating functions and limit the radiation problem when necessary, without much concern about frequency spilling. Square Gaussians with a temporal width as short as of a few ps have been used for these lines in some cases. However, as shown in Fig. 7.2, these narrow functions can limit the useful information to frequencies above 100 GHz.
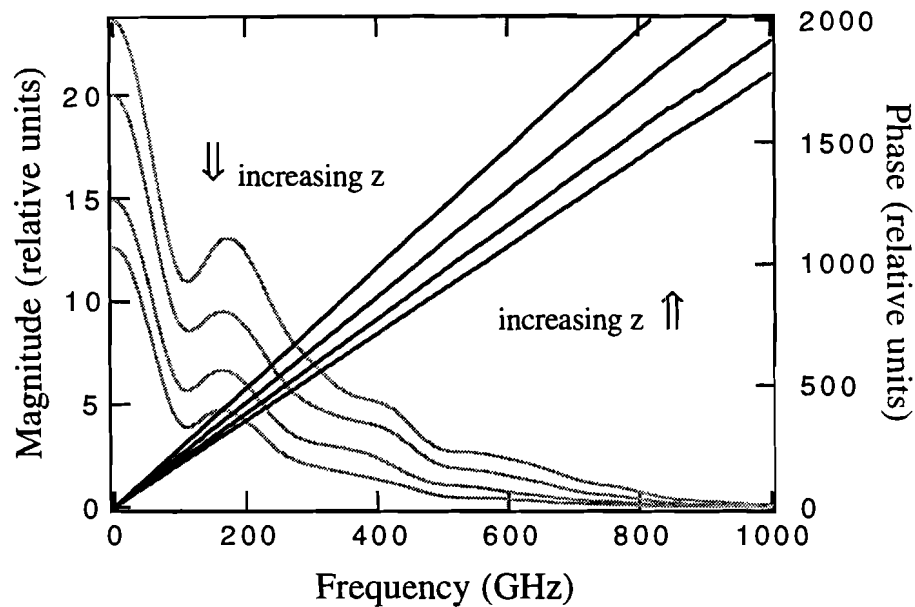
Fig. 7.3   A spectral representation of some time-domain data measured on a 10 μm CPW with narrow ground. The gating function is $e^{-(t/150)4}$.

Figure 7.3 shows the frequency domain representation of some experimental data measured on a 10 μm CPW with narrow ground. As the waveforms travel on the transmission line, the magnitude of the signal at each frequency is reduced while its phase is increased. By considering the signal magnitude and phase as functions of propagation distance, we can use Eq. 7.2 to extract the values of α and ε_{eff} for each

frequency. The availability of data at several measurement positions enables us to use a least square fit for the calculation of α and ε_{eff} and improve the accuracy of the measurement.

7.2 Straight lines—50 μm technology

The results presented in this section were obtained from the spectral analysis of the time domain data discussed in section 6.1. Figure 7.4 shows the resulting values of attenuation and ε_{eff} for a pair of 50 μm CPWs (for time domain data, see Fig. 6.3). The theoretical predictions according to Frankel et al, and Hasnain et al [2, 3] are also plotted for comparison.
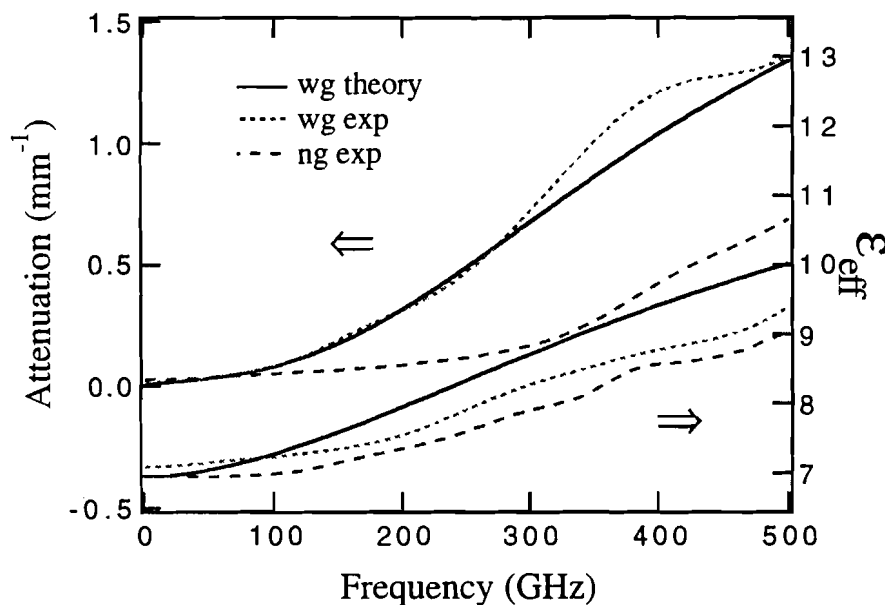
Fig. 7.4   Attenuation and effective permittivity for 50 μm CPWs, with ground-planes widths of 50 and 500 μm. The experimental results are compared to theoretical predictions for a wide-ground CPW. "ng" stands for narrow ground, and "wg" stands for wide ground conductors

The experimental results on effective dielectric permittivity show that dispersion on the two CPWs is comparable, but significantly less than the theoretical predictions. It has been suggested [4, 5] that dispersion is reduced if a narrow ground plane is used, but our results do not show any significant differences. However, there seems to be a small offset between the value of ε_{eff} in the two transmission lines

which in good agreement with the time domain velocity measurements in chapter 6—table 1. This is in qualitative agreement with the formalism of Goine and Naldi [6]. Even though the observed difference small, it is still much larger than their predictions.

In contrast to dispersion, the results on attenuation show a large difference in the performance of the two CPWs. While the wide-ground line has a loss characteristic that is well described by theory, the attenuation of the narrow-ground line is surprisingly lower. This difference is more dramatic in the frequency region between 100 and 300 GHz where radiation starts to dominate. On a millimeter scale, the narrow-ground line is essentially lossless up to 300 GHz. For higher frequencies, attenuation in this line starts to increase at a higher pace, but is still significantly lower than the traditional wide-ground CPW.
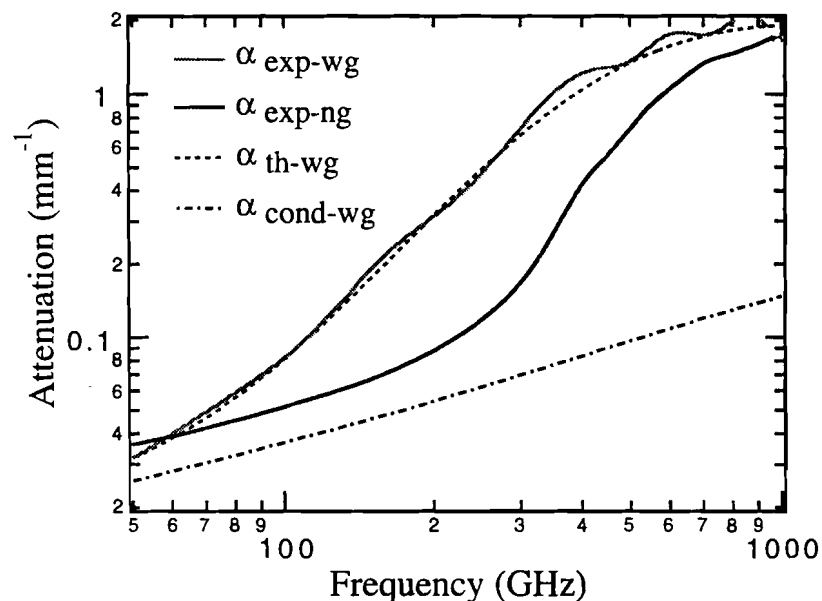
Fig. 7.5   Attenuation for 50 μm CPWs, with wide and narrow ground planes of 50 and 500 μm, compared to theoretical predictions for conductor and total loss.

In order to understand the processes which are responsible for loss in the two CPWs the signal attenuation on the transmission lines is plotted on a logarithmic scale in Fig. 7.5. Again the close agreement between the theoretical predictions and the wide ground CPW is clearly visible (the validity of the experimental results for the wide-ground CPW above 600 GHz is questionable because the fast loss of the signal energy at these frequencies). On the other hand, the loss on the narrow-ground line

initially has the same square-root frequency dependence as conductor loss. This implies that for low frequencies, the narrow ground planes cause a strong reduction of radiation, perhaps trough reduced coupling between the CPW mode and the substrate modes [7,8]. As a result the range the transmission line is only limited by conductor loss is extended form less than 100 to 300 GHz (see fig. 3.8). Around the frequency of 200 GHz, and for more than 150 GHz bandwidth, the attenuation in the narrow-ground CPW is by half an order of magnitude smaller. This is a drastic difference is well beyond experimental uncertainties and indicates a fundamental difference between the narrow and wide-ground CPWs. It has to be noted that apart from a recent theoretical study [4], this effect has been completely overlooked.

For frequencies higher than 300 GHz, radiation dominates attenuation in the narrow-ground CPW as well. Above 600 GHz, the behavior of the two transmission line converges and the width of the ground plane has little influence on their loss characteristics.
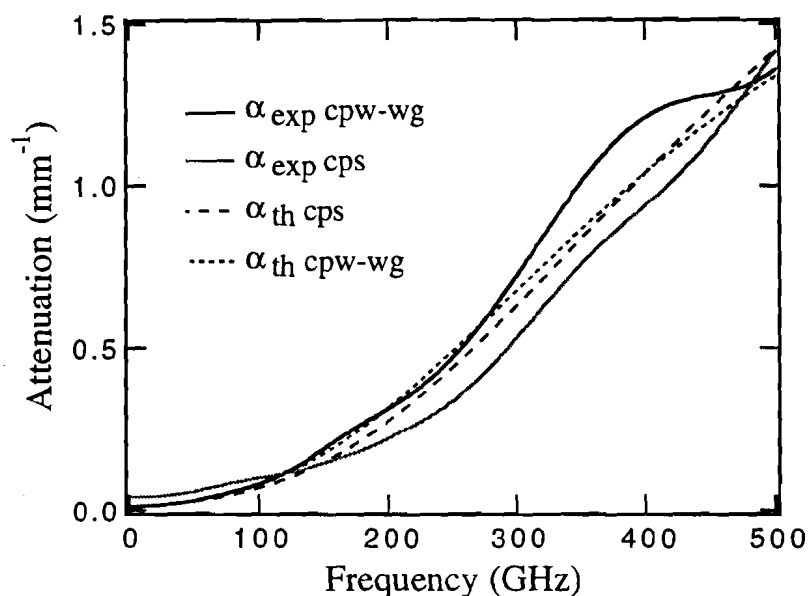
Fig. 7.6   The experimental loss characteristics of a 50 μm CPS and a CPW with a 500 μm wide ground, together with the corresponding theoretical estimates.

The results in chapter 6 have already shown that, as expected by theory [9], there is a strong correlation between the behavior of wide-ground CPWs and CPS. This position is further reinforced by Fig. 7.6, which shows the frequency dependent attenuation for these transmission lines. The experimental results indicate that for

frequencies up to 100 GHz the CPS is marginally more lossy, but for higher frequencies the situation is reversed. The theoretical prediction that attenuation will be slightly higher in the CPW for most of the spectrum is confirmed by the experimental results. Even though the experiments show that the difference in attenuation between the two lines is a bit larger than the theoretical prediction, it is still much less than the difference between the CPWs with different grounds (Fig. 7.4 and 5).
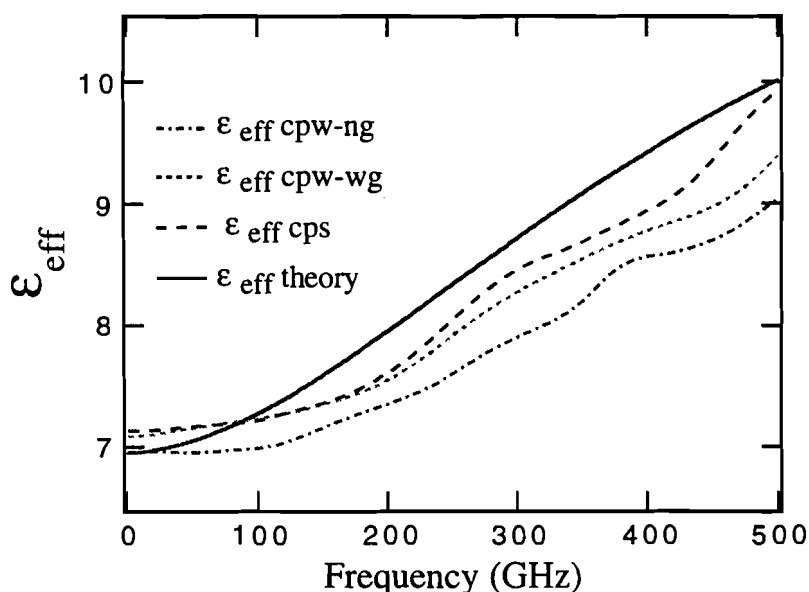
Fig. 7.7   The effective permittivity of 50 μm CPS, and CPWs with narrow and wide grounds of 50 and 500 μm.

Apart from loss, the dispersion characteristics of the wide-ground CPW and the CPS also have a strong similarity. This is clearly shown in Fig. 7.7, where the effective permittivity of all 50 μm lines (CPS, CPW with wide and narrow ground) is compared to the theoretical expectation. For frequencies up to 100 GHz, the effective permittivity of the CPS and the wide-ground CPW are identical but marginally higher than the narrow-ground CPW. For the CPWs this small offset in ε_{eff} remains roughly constant with frequency indicating similar dispersion. For the CPS, ε_{eff} increases slightly faster with frequency and tends to approach the theoretical value, but this effect is weak. To this point, our experiments indicate that, while theory fits our experimental data on attenuation very well, it slightly overestimates dispersion in the 50-μm coplanar lines.

7.3 Straight lines—10 µm technology

The spectral parameters presented here were obtained from the time domain data of the 10-µm transmission lines discussed in section 6.2. We start our analysis with a comparison of narrow-ground CPWs with lateral dimensions of 10 and 50 µm, respectively. Figure 7.8 shows both attenuation and effective permittivity of these transmission lines on a logarithmic scale.
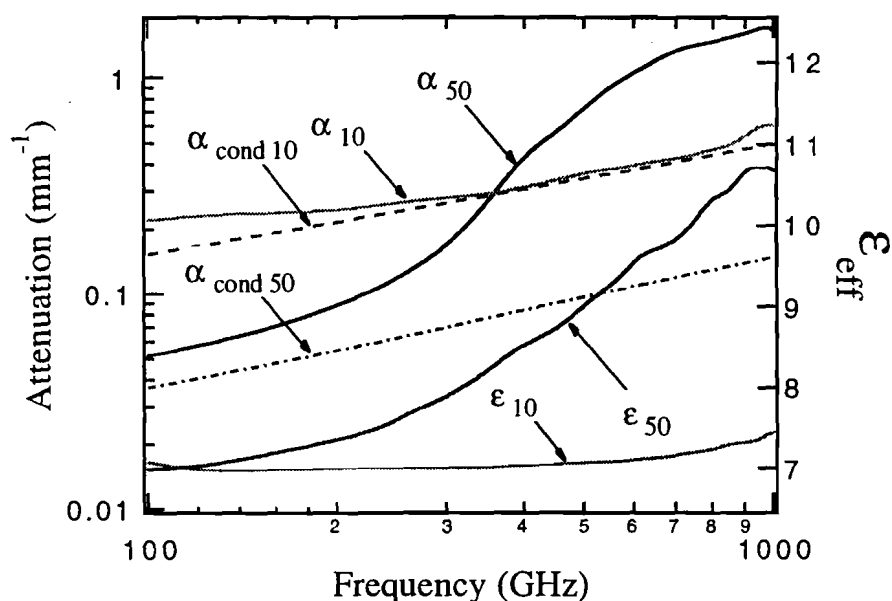
Fig. 7.8   Attenuation and effective dielectric permittivity for narrow-ground CPWs with lateral dimensions of 10 and 50 µm. The ground plane width is the same as the line dimensions.

There is a sharp contrast in the way ε_{eff} changes with frequency in each CPW. For the 50µm line, the value of ε_{eff} increases from about 7 at 100 GHz to almost 11 at 1 THz. This large increase is responsible for the large amount of dispersion visible in the time domain data (Fig. 6.3). As we have already seen in chapter 3, a reduction of the CPW dimensions reduces dispersion considerably. In the 10 µm CPW, the effective permittivity changes only marginally in the same frequency range. For this reason dispersion in this line is very limited and its propagation characteristics are heavily determined by loss.

We have shown that a reduction of the ground plane width reduces radiation loss in 50 µm CPWs. This effect seems to be even stronger for the 10 µm CPWs. A

comparison of the total attenuation and the theoretical expectation of conductor loss for the 10 μm narrow-ground CPW shows a remarkable similarity for frequencies above 300 GHz. One would expect radiation to dominate attenuation for high frequencies but it seems that the narrow ground plane has eliminated this loss mechanism completely. For lower frequencies, the measured attenuation decreases at a slower pace with frequency because the skin depth becomes comparable to the conductor width (Our calculation of conductor loss has assumed that the transmission line is always limited by the skin depth—for our structures the skin depth is equal to the conductor thickness of 290 nm at 90 GHz).

Although the reduction in radiation is more dramatic in the 10 μm CPW, for low frequencies the total loss is reduced to a much larger extent in the 50 μm line. This happens because conductor loss is much higher in the 10 μm CPW, while in the 50 μm line radiation is always dominant. For this reason the range of frequencies the 50 μm line is less lossy is extended to ~350 GHz — a frequency ~180 GHz larger than the corresponding value for wide ground CPWs (see Fig. 7.9).
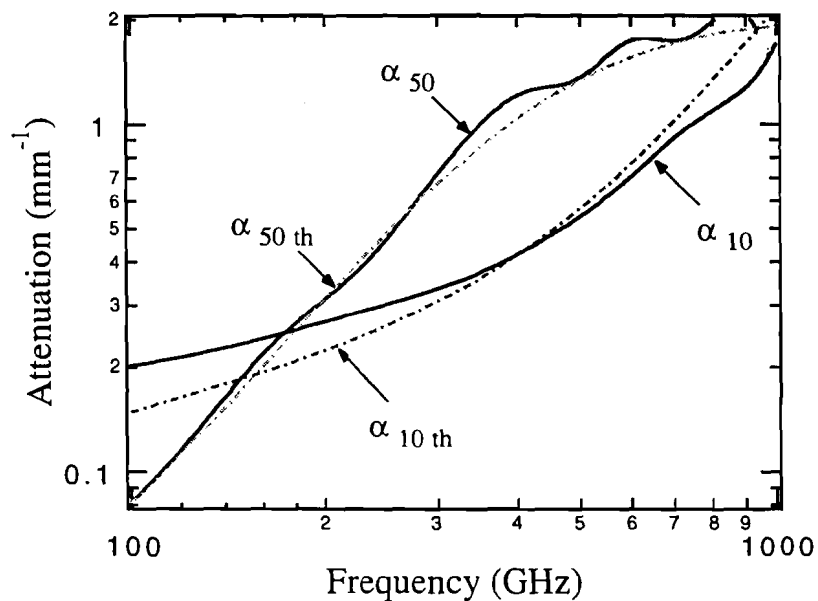
Fig. 7.9   Attenuation in 10 and 50 μm CPWs, with a ground plane width of 500 μm, compared to theoretical predictions.

Like the 50 μm CPW, the 10 μm CPW with wide ground planes has a loss characteristic that is much better fitted by theory. Again, for the lower frequencies the

measured attenuation is higher than the theoretical prediction because of the finite conductor thickness. For higher frequencies, the experimental loss is slightly lower than the theoretical expectation, but still much higher than the corresponding values for the narrow-ground line in Fig. 7.8. More importantly, in the frequency region above 400 GHz, the rate attenuation increases with frequency is consistent with a loss characteristic which is dominated by radiation.
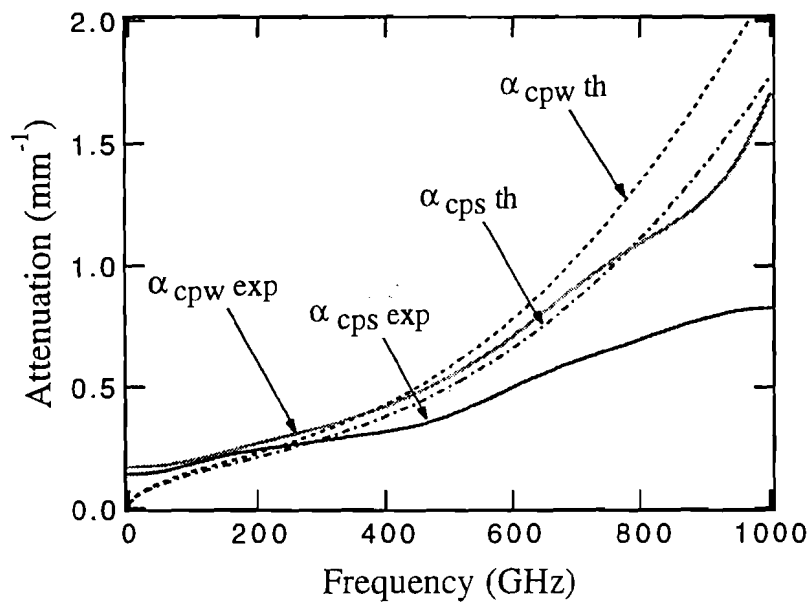
Fig. 7.10   The experimental attenuation in a 10 μm CPW with wide ground and a 10 μm CPS compared to theoretical predictions.

The loss characteristics of a 10 μm CPS and a wide-ground CPW are plotted in Fig. 7.10 on a linear scale. For frequencies below 200 GHz the two transmission lines are indistinguishable. Theory predicts that the CPW will experience marginally higher loss than the CPS in at higher frequencies. Both lines seem to suffer reduced attenuation in this range. Although this effect is only marginal in the CPW, it is more significant in the CPS which appears to have a clear advantage. Nevertheless, compared to the narrow-ground CPW (Fig. 7.8), the CPS is still significantly more lossy .
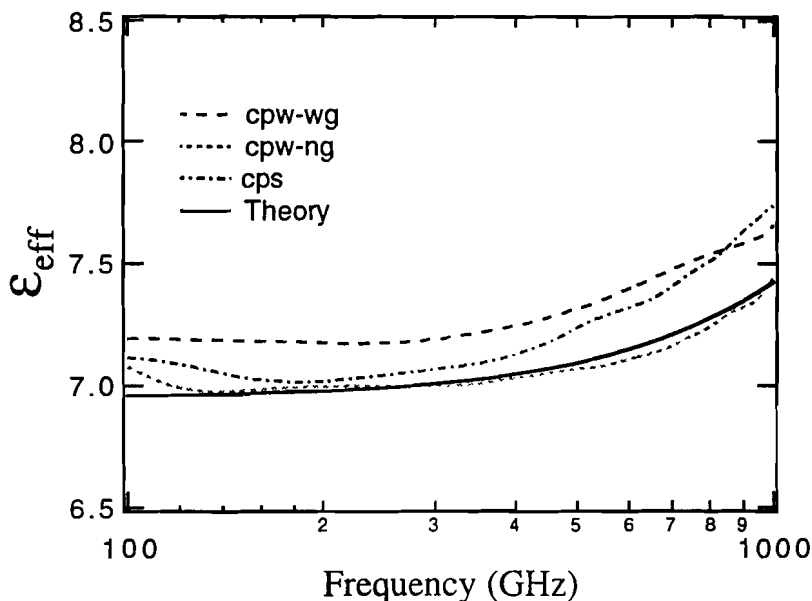
Fig. 7.11   The effective permittivity of 10 μm CPS, and CPWs with narrow and wide grounds of 10 and 500 μm.

There is a very small change in the effective dielectric permittivity of the 10 μm lines compared to the 50 μm CPWs. Nevertheless, as can be seen in Fig. 7.11, there are still some marginal differences between the various 10 μm lines. It appears that the narrow-ground CPW has a value of ε_{eff} that is closest to the theoretical estimate. The result for the wide ground CPW has an identical dependence with frequency but is shifted to a marginally higher value. On the other hand, the CPS starts with a value of ε_{eff} that is closer to the narrow-ground line at low frequencies, but at high frequencies its permittivity is similar to the wide ground CPW. This indicates slightly larger dispersion for the CPS compared to the CPWs. We have to point out that these differences are very small and only correspond to changes in propagation velocity of less than 2%. These small differences in velocity are also well described by the time domain data — see table 6.1.

7.4 Bent lines—50 μm technology

The qualitative analysis of the 50-μm bent-lines in section 6.3, has shown that bends primarily affect high frequencies. It is in this regime where the shape of the

bend can affect the propagation characteristics of the transmission line significantly. In the section we will use spectral analysis in order to give a complete, quantitative description of the bend lines.
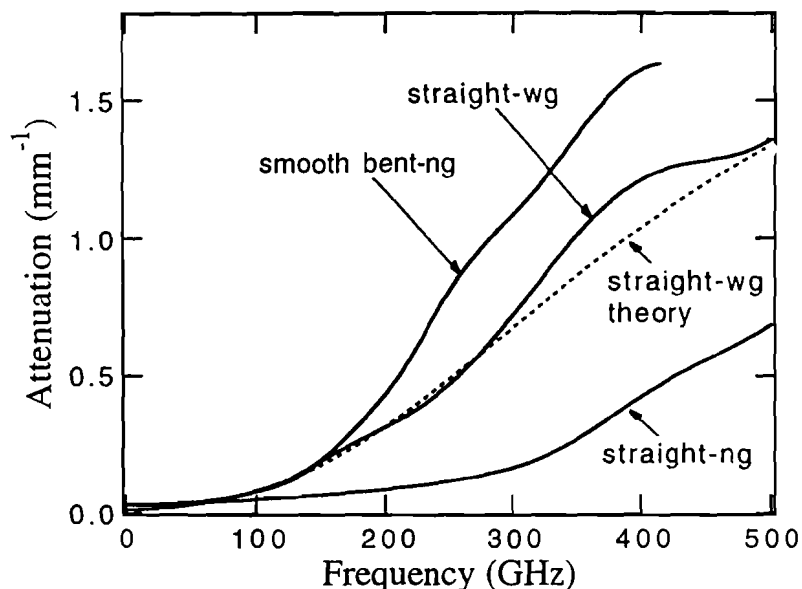
Fig. 7.12   Attenuation in a 50 μm CPW with narrow grounds and smooth bends, compared to the loss in two straight CPWs with narrow and wide grounds of 50 and 500 μm. For the bend line the information is limitted to 400 GHz because signal spectrum is quickly reduced to the noise level.

We begin our analysis with a comparison of loss characteristic of a narrow-ground CPW with smooth bents and its straight counterparts in Fig. 7.12. In the low frequency regime, and up to 100 GHz, all three transmission lines suffer the same attenuation. In this regime the bent CPW can be used freely without any additional compromises in the performance of the circuit it is implemented in. For higher frequencies, the loss in the bent line increases at a much faster pace compared to the straight line with the narrow ground, and in the frequency region around 300 GHz, the characteristics of the two lines become dramatically different. The difference in attenuation is far less apparent if the bent line is compared to the wide-ground CPW because the additional loss induced by the bends is partially balanced by the extra loss induced by the wide ground planes of the straight line. For bent line the span of the experimental data is reduced to 400 GHz because the enhanced loss in this CPW eliminates the high frequencies almost instantly. This effects is generally observed in most of the bent transmission-line characteristics shown in this chapter.
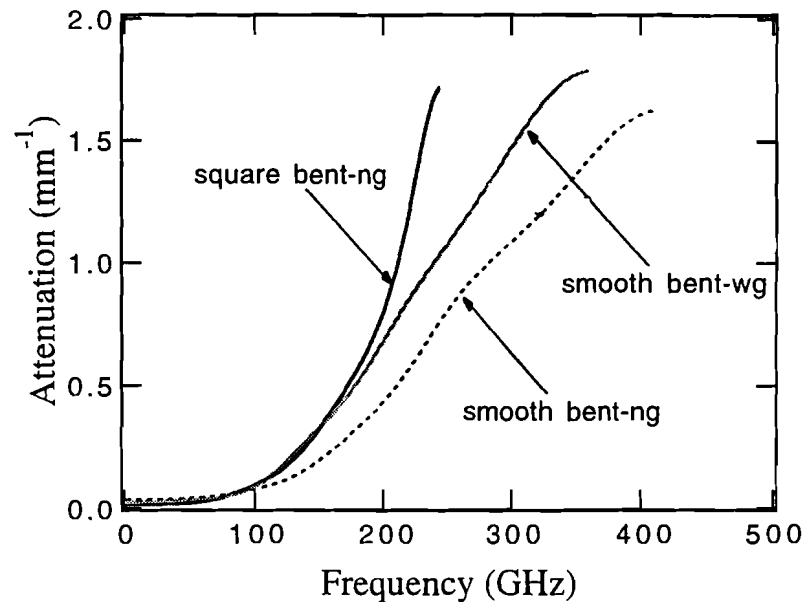
Fig. 7.13   The effect of bend shape and ground plane width on the loss characteristics of 50-μm bent CPWs.

The characteristics of the different bent CPWs are compared in Fig. 7.13. Again, for low frequencies the CPWs are indistinguishable, but above 100 GHz the effects of the bend geometry and ground-plane width become clearly visible. A comparison of the narrow ground lines reveals that for frequencies higher than 100 GHz the square bent CPW has an increasingly higher loss coefficient, which at ~230 GHz is a factor of 2 larger than the coefficient for the smooth-bent line. The use of wide ground plane causes additional attenuation in the smooth-bent CPWs as well. In the frequency region between 100 and 200 GHz the use of a wide ground plane is almost as harmful as the implementation of a square bend. For higher frequencies the increase of loss in the wide-ground line is less dramatic than the square-bent CPW but still significantly higher than the smooth-bent CPW with narrow grounds.

The spectral analysis of the straight lines in sections 2 and 3 of this chapter has shown that the CPS has better high frequency performance than the wide-ground CPW. The difference between the two lines is only marginal for the 50 μm lines but becomes significant in the 10 μm lines. However, when bends are implemented in the transmission lines, the situation changes. Figure 7.14 shows that now it is the bent CPS that is more lossy. In the neighborhood around 100 GHz, the loss characteristic of the CPS deviates significantly from the straight line behavior forcing the

appearance of a solid difference between the loss coefficients of the two bent lines. This difference in attenuation remains roughly constant with increasing frequency and as the total loss in the transmission lines in increased the behavior of the transmission lines converges. Of course in this range, both lines exhibit much higher attenuation than their straight line counterparts.
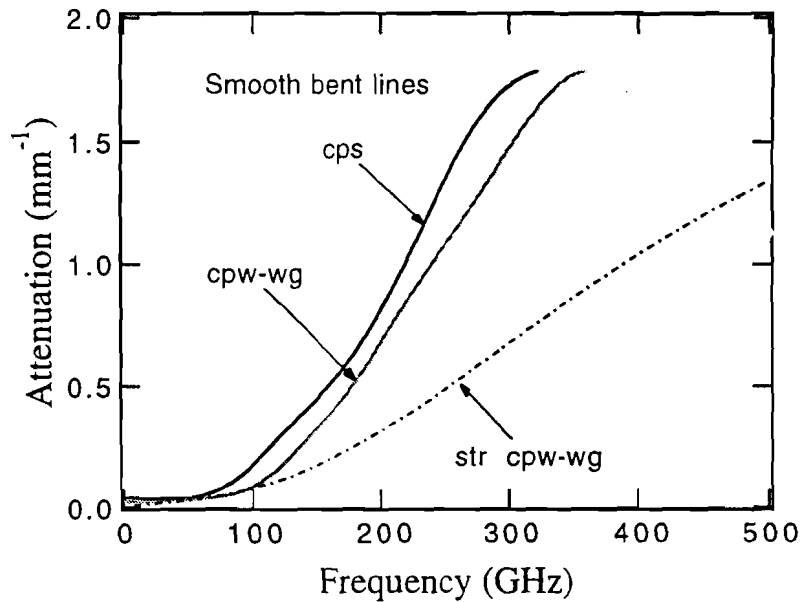
Fig. 7.14   The loss characteristics of a 50-μm bent CPS, and wide-ground CPW of the same dimensions. The attenuation of a straight CPW with a wide ground is also plotted for comparison.

The bends not only alter the loss characteristics of the transmission lines, but also affect their effective dielectric permittivity and dispersion. Figure 7.15 shows that at low frequencies, the bent lines have a marginally lower ε_{eff} than the straight lines. Although this difference is very small, it suggests that the effective length of the bends is slightly shorter than their true geometrical length [10]. However, as the frequencies increase, ε_{eff} changes at a faster pace in the bent lines. This effect is more apparent in the characteristic of the bent CPS— the line that also suffers the most dramatic increase in loss. For frequencies above 150 GHz, the ε_{eff} in the bent CPS is not only higher than the experimental result for the straight CPW, but also the theoretical expectation. The fast increase of the effective permittivity with frequency means that dispersion in the bent transmission lines is enhanced. The decline in the

value of ε_{eff} above 300 GHz is again attributed to the fast loss of the high frequency spectrum in the bent lines.
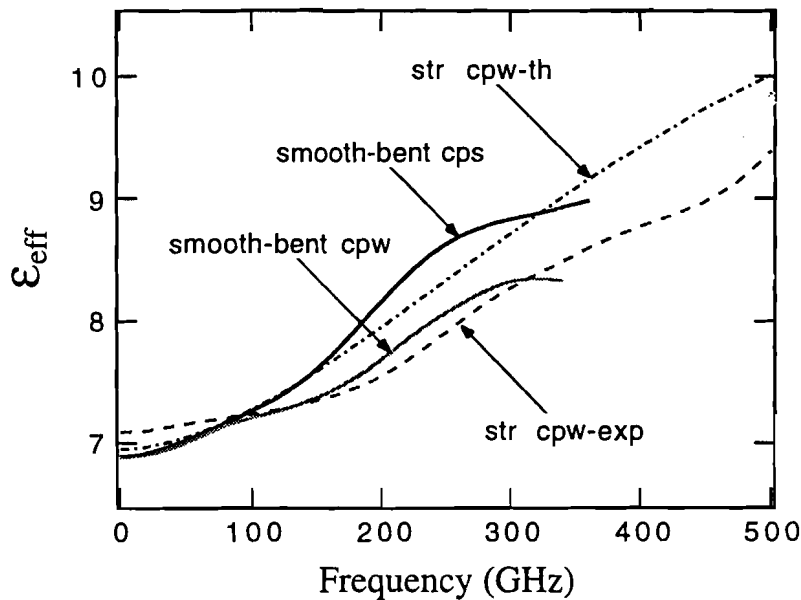
Fig. 7.15   Dispersion curves for bent CPS and CPWs with lateral dimensions of 50 μm, compared to theory and experimental results for a straight CPW with the same dimensions. The ground plane width of the CPWs is 500 μm.

Figure 7.16 shows the effective permittivity of the bent CPWs with narrow grounds. As can be seen in the figure, the behavior of these lines is similar to the bent CPS and CPW with wide grounds. Again, at low frequencies the bent CPWs have a lower value of ε_{eff} compared to their straight counterpart. However, this difference is enhanced for the square-bent CPW. It seems that the effective length of the bend is significantly affected by its geometry, and for a square bend it becomes significantly shorter [10]. Even though the difference in the overall value of ε_{eff} is small, it reflects the higher velocity we have observed in the square-bent line with the time domain measurements — see table 6.1. It is interesting to note, that for frequencies up to 200 GHz both bent CPWs exhibit the same dispersive behavior. Compared to the experimental result for the straight line, however, dispersion in the bent lines is increased significantly. Nevertheless, it is still comparable to the overestimated value given by the theoretical calculation.
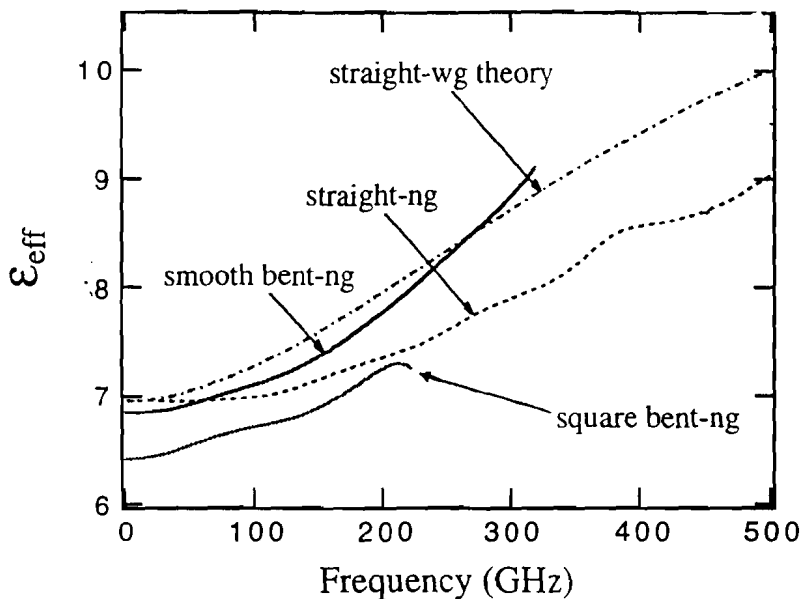
Fig. 7.16   Effective dielectric permittivity for square and smooth-bent CPWs, with narrow-ground and lateral dimensions of 50 μm. The characteristics of a straight CPW and the theoretical estimate for a wide-ground line, are also plotted for comparison.

7.5 Bent lines—10 μm technology

In section 6.4 , we have seen that the difference in the characteristics of the 10-μm straight and bend transmission lines is relatively small compared to the differences observed in the 50-μm lines. This is due to the fact in the 10 μm lines, the bends only cover 10% of the transmission line length, compared to a 50% ratio for the 50-μm lines. In order to emphasize the sharp difference in the behavior of the 10 and 50 μm lines, we plot the loss characteristics of a pair of smooth-bent CPWs in Fig. 7.17. As we have already seen, for frequencies above 100 GHz, the attenuation in the 50 μm line increases at a fast pace. On the other hand, the 10 μm line is essentially unaffected by the presence of the bends for frequencies as high as 450 GHz. The familiar situation where the 10 μm line is more lossy than the 50 μm line at low frequencies, and less lossy at high frequencies, is again observed. The difference is that, because the 50-μm CPW is affected by the bends at low frequencies, the frequency for which attenuation in the two CPWs is the same is shifted down to 150 GHz from the value of 350 GHz seen in the straight CPWs (see Fig. 7.8).
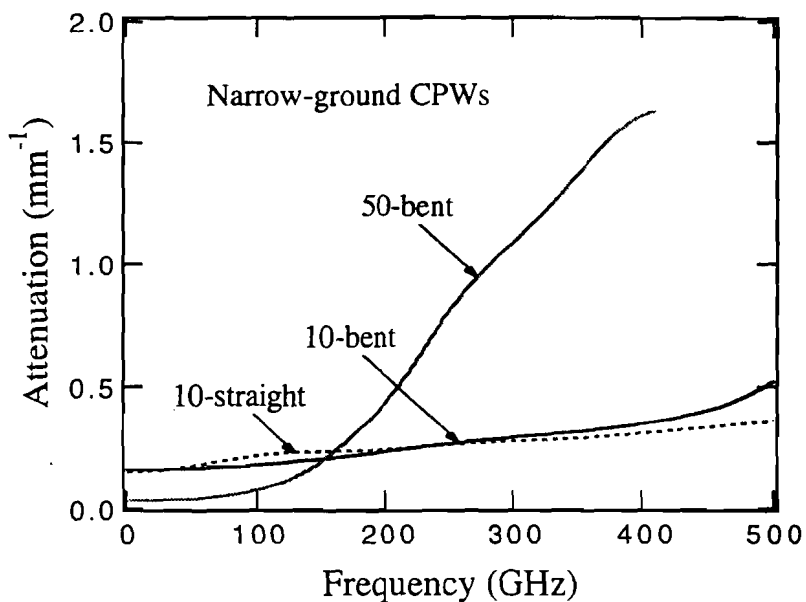
Fig. 7.17   A comparison of attenuation in smooth-bent CPWs with lateral dimensions of 10 and 50 μm.
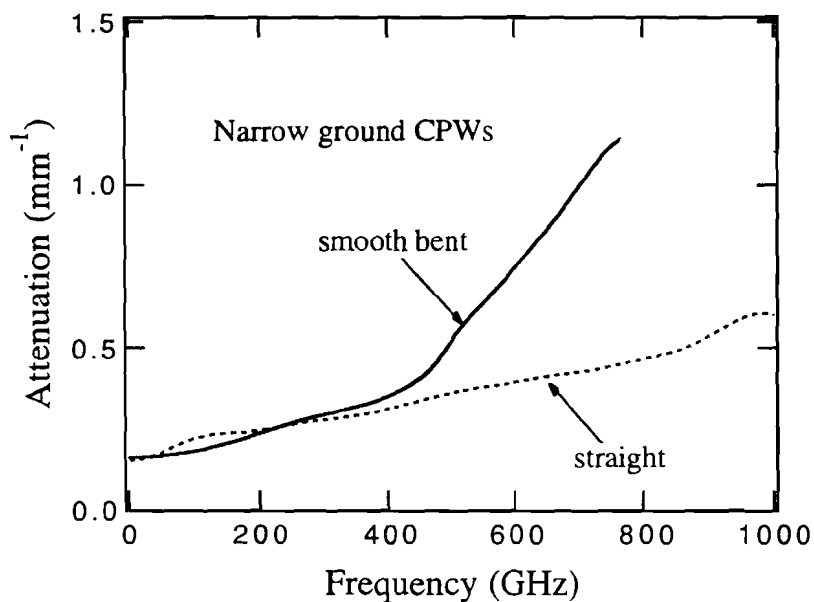
Fig. 7.18   The loss characteristics of a straight and a smooth-bent CPW, with lateral dimensions of 10 μm.

After showing the sharp contrast between the 10 and 50 μm bent CPWs, we will focus our attention on a comparative study of the 10 μm transmission lines. We

continue with a comparison of loss in the straight and bent CPWs (same lines as in Fig. 7.17), but now over a bandwidth of 1 THz. Up to a frequency of 400 GHz, the two CPWs exhibit essentially the same loss behavior and the presence of the bends can be neglected (Around a 100 GHz, the straight line appears to be slightly more lossy but this is clearly an artifact). For higher frequencies, attenuation in the bent-line increases at an accelerated pace, and at 650 GHz it becomes a factor of 2 larger compared to the loss in the straight CPW.
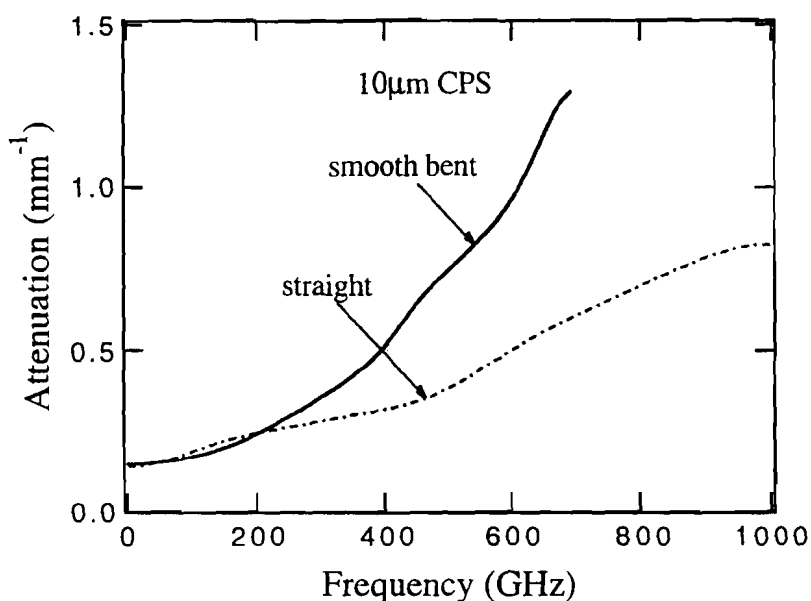
Fig. 7.19   Attenuation in straight and bent CPS, with lateral dimensions of 10 μm.

A comparison of the loss characteristics of straight and bent CPS in Fig. 7.19 leads to similar conclusions. The difference is that for the CPS, attenuation in the bent line starts to increase at the much lower frequency of 200 GHz. As a result, at the bent CPS becomes substantially inferior at frequencies as low as 400 GHz.

Of course, a comparative study of the loss behavior of all bent lines, with lateral dimensions of 10 μm, would be of more interest. Figure 7.20 shows the attenuation suffered by the smooth and square-bent CPWs, together with the loss characteristic of the smooth-bent CPS. In contrast to the 50 μm lines, very little difference is observed between the two bent CPWs. As expected, the square-bent line is slightly more lossy at high frequencies, but the difference is only marginal. On the

other hand, the loss characteristic of the bent CPS is significantly inferior. The difference in the behavior of the CPS is more apparent in the frequency neighborhood around 400 GHz. As we have already seen in the 50 μm lines, attenuation in the CPS is more susceptible to the presence of the bends. Moreover, the CPS can not take advantage of the improved loss characteristic offered to the bent CPWs by the their narrow ground planes.
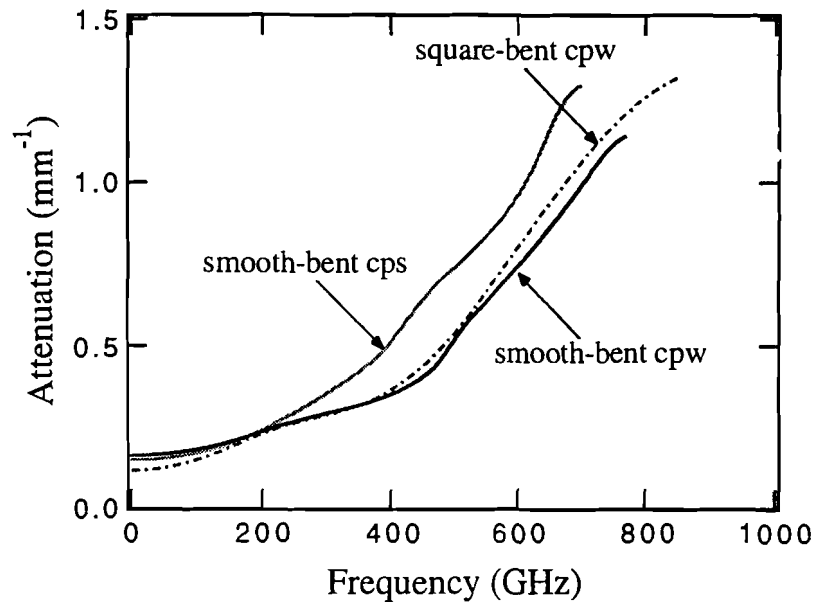
Fig. 7.20   The loss characteristics of all the bent transmission lines with lateral dimensions of 10 μm.

To this point, our experimental data have shown that both bends and wide ground planes tend to increase high frequency loss in the CPWs. In order to test which geometrical factor dominates the behavior of the lines, we overlay the loss characteristics of a straight CPW with a wide ground, and a square-bent CPW with a narrow ground in Fig. 7.21 (The data presented in this figure were extracted from the time domain data shown in Fig. 6.14). The spectral results show that the ground planes dominate the loss behavior of the CPWs at low frequencies. Since up to 400 GHz the bends have essentially no effect on the performance of the line, the bent CPW is significantly less lossy, thanks to its narrow ground planes. Above 400 GHz, attenuation in the bent CPW increases abruptly and surpasses the loss in the straight line at ~500 GHz. For higher frequencies, the bend line becomes slightly more lossy.

In general terms, the difference in the performance of these lines is significant, but nevertheless not dramatic. It seems that the two geometrical effects increase loss in the CPWs by similar amounts. This means that by using a narrow-ground CPW, one can afford to introduce bends in the transmission line and still expect a performance comparable to a straight line with wide grounds. It has to be pointed out that the same conclusions about these CPWs were reached in chapter 6 with time domain analysis. However, with spectral analysis we are able to give a quantitative comparison as well.
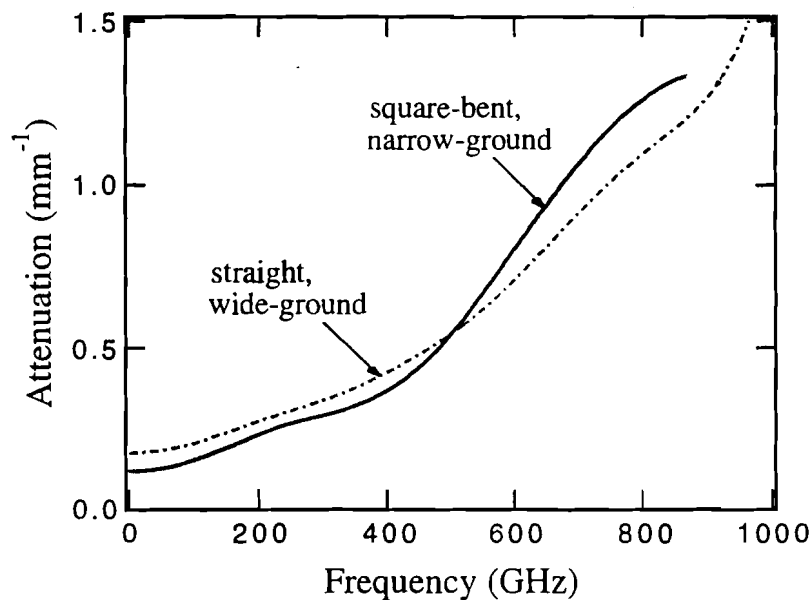
Fig. 7.21   A comparison of the effects of bends and wide ground planes on the loss characteristics of 10-μm CPWs.

The dispersion curves for all three bent lines are shown in 7.22 together with the experimental result for a straight CPW with a narrow-ground, and the theoretical estimate for a straight CPW with a wide ground. The results show that ε_{eff} for all lines, straight or bent, is essentially the same and dictate that the effective dielectric permittivity in the 10 μm transmission lines is not significantly affected by the presence of the bends. This is not an unexpected result since the 10 μm transmission lines suffer very limited dispersion to begin with, and the bends only cover 10% of their geometrical length.
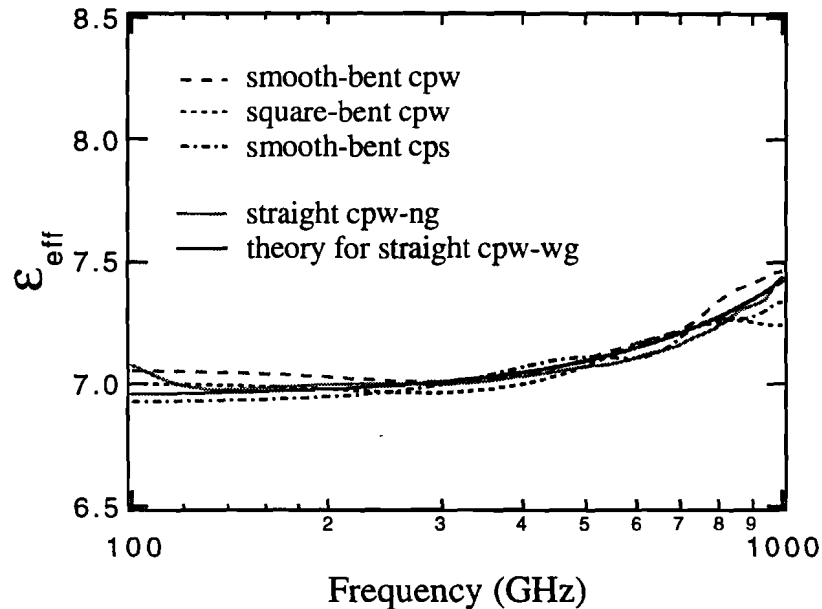
Fig. 7.22   Effective dielectric permittivity in 10 μm straight, and bent transmission lines .

7.6 Odd and even modes

We have studied the evolution of the odd and even modes, which can routinely be excited after CPW discontinuities, in sections 6.5 and 6.6. Our time domain analysis has shown that in order to understand the evolution of the signals after such discontinuities (see Fig. 6.15), the odd and even modes have to be treated separately. The odd mode, which corresponds to the standard CPW mode, has been studied in detail both in the time and frequency domain (sections 6.1 and 7.2). On the other hand, it is known that the even mode has distinctly different characteristics [11] because it corresponds to the mode of a CPS defined by the two ground of the 50-μm CPW (for wide-ground CPWs the even mode corresponds to the mode of a slotline specified by the two ground planes).

We have tried to extract the spectral characteristics of both the odd and even mode from the time domain data, measured after a single CPW bend, but with limited success. The case where wirebonds were used to limit the excitation of the even mode is studied separately from the case no wirebonds were used. The results on

attenuation, which represent the most inferior outcome of our analysis, are shown first in Fig. 7.23.
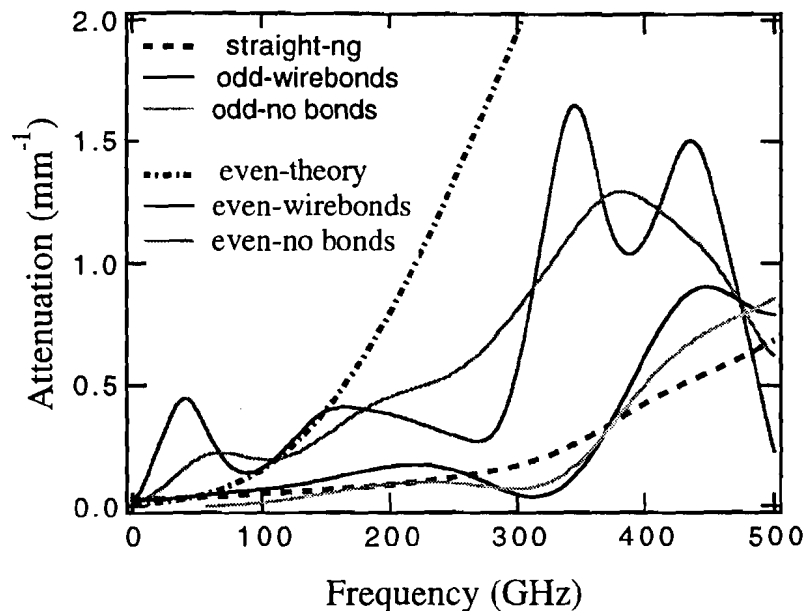
Fig. 7.23   The attenuation suffered by the odd, and the even modes excited after the signal propagates through a CPW bend, is distinctly different.

Although the even-mode results on attenuation are poor, they still indicate that the loss in this mode is much higher than the odd mode. This observation is in qualitative agreement with the theoretical expectations [12] which predict higher loss for the even mode. The odd mode results are significantly more solid, and they clearly indicate that the loss in this mode corresponds to the result given by the straight CPW with narrow grounds. On a qualitative level, little difference is observed between the case where the grounds were connected with wirebonds and the case no bonds were used. This is to be expected because, in a linear system like our transmission lines, the future evolution of the propagated signal is independent of its history.

The results on the effective dielectric permittivity of the two modes (seen in Fig. 7.24) are visibly better, nevertheless the even mode results are still significantly inferior. For the odd mode, there is an excellent agreement between the value of ε_{eff} recorded here and the result for the narrow-ground CPW. However, both results show that the theoretical expectation for the wide-ground CPW clearly overestimate dispersion. The results on the even mode are less impressive, but are accurate enough

to indicate that the increase of ε_{eff} with frequency is significantly lower than the theoretical prediction. Again, the presence of wirebonds has no significant effect on the effective permittivity of either mode. For frequencies less than 100 GHz, the ε_{eff} of the even mode seems to increase abruptly. This is an artifact caused by the fact that the even mode signal is bipolar in nature (see Fig. 7.25), and its spectral content in this frequency range is minimal. For the same reason, the results on the attenuation of the even mode in this frequency range(Fig. 7.23) were also poor.
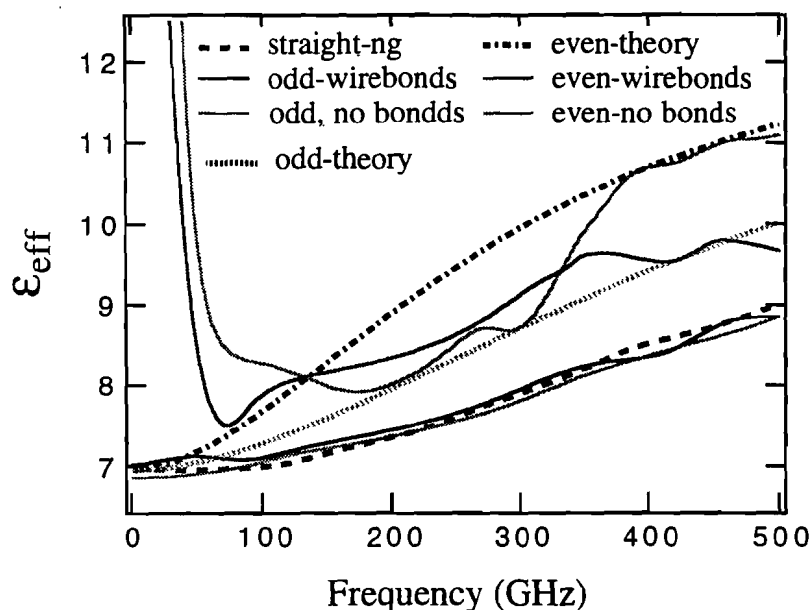
Fig. 7.24   Dispersion curves for the odd and even CPW modes. The theoretical estimates are also plotted for comparison.

The accuracy of the results in this section, both for the odd and even mode, is also affected by two other parameters. The first is the fact that the time-domain measurements only span a time window of approximately 20 ps compared to more than 50 ps for the straight lines and more than 80 ps for the bend lines. This means that the accuracy of the measurements for the mode evolution is intrinsically inferior. Moreover, the geometry of the transmission line used for studying the odd and even modes has proven to be more susceptible to radiation because there is a direct path for the radiation emitted from the excitation site to reach the measurement positions — see Fig. 6.15. Of course, this is more of a problem for the even mode which is affected by radiation to a much larger extent. In addition, the even mode

measurements also have to face the problem of the fast loss of the high frequency spectrum induced by the extraordinary high loss experienced by this mode.

In order to overcome the fundamental limitations imposed on the study of mode evolution by frequency-domain analysis, we will address the problem in a different direction. By this stage we have been able to obtain solid experimental results for both loss and dispersion of the standard CPW mode — the odd mode. For the even mode, where the situation is less clear, we can use the expected values of α and ε_{eff} and simulate the propagation of the even mode data. This is done in Fig. 7.25 for the case no wirebonds were used to limit the excitation of the even mode.
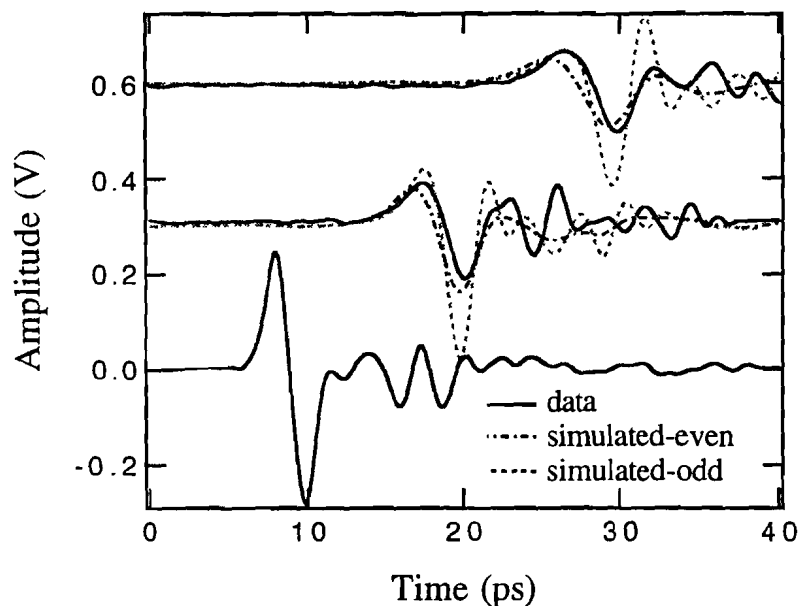
Fig. 7.25   The evolution of the even-mode signal excited by a CPW bend with no wirebonds. The propagation of the initial data is simulated with the odd and even mode parameters for comparison.

For the simulation of the even mode propagation we used the loss characteristic for the CPS formed by the two ground of our CPW (same data plotted in Fig. 7.23). However, for the ε_{eff} we used the theoretical value corresponding to the odd mode because it gives a better fit to the experimental results in Fig. 7.24 (it seems that theory overestimates dispersion in all 50 μm lines we tested). For comparison purposes, the same *even-mode* data are also propagated with the *odd–mode* experimental parameters in Fig. 7.25. The data propagated with the even-mode

parameters fit the experimental results well. They experience approximately the same loss and high frequency dispersion. There seems to be a small discrepancy for low frequency dispersion, however. It seems that the low-frequency part of the simulated data travels at a marginally higher speed and suffers more dispersion than the experimental data. On the other hand, the data propagated using the odd-mode parameters behave in a distinctly different manner. The loss they experience is only a small fraction of the attenuation suffered by the experimental data. In addition, dispersion is also much less than what is indicated by the experiment.

Summary

This chapter presented a spectral characterization of a family of wide bandwidth coplanar transmission lines. The characteristics of straight and bend lines with various geometries were studied in detail. The excitation of the even mode was also investigated. The results of our frequency-domain studies are quantitative in nature, and span a bandwidth up to 1 THz. The conclusions of our analysis are summarized below.

- In CPWs, a reduction of the ground plane width limits radiation and causes a dramatic reduction of total loss. For some frequencies, the attenuation coefficient is reduced by half an order of magnitude.
- For the 50-μm lines, this effect is dominant for frequencies up to 400 GHz. For the 10-μm CPWs, radiation is completely eliminated.
- The loss characteristics of the 50-μm CPWs, and CPSs, are in good agreement with theory and comparable up to very high frequencies.
- The 10-μm CPS is significantly less lossy than both its the theoretical estimate, and its CPW counterpart.
- Theory clearly overestimates dispersion in all 50-μm lines. On the other hand, the 10–μm lines are almost dispersionless.
- The bends degrade the loss characteristics of all transmission lines, but only at high frequencies — higher than ~100 GHz for the 50-μm lines, and ~400 GHz for the 10-μm lines.

- In contrast to the straight lines, bent CPS are significantly more lossy than CPWs.

- In 50-μm lines, smooth bends cause a significant reduction in attenuation, but for 10-μm lines the advantage is only marginal.

- The use of wide ground planes, or bends, increases lossless in CPWs. For 50-μm lines the effect of bends is clearly dominant, but not for the 10-μm CPWs.

- In 10-μm CPWs, attenuation is dominated by the bends for frequencies higher than 500 GHz, but for rest of the spectrum the ground plane width is more important.

- Bends increase dispersion in the 50-μm lines, but also reduce the quasistatic value of ε_{eff}. The reduction of ε_{eff} depends on the bend geometry and is much stronger for the square bends.

- The signal evolution after discontinuities can be understood by the separate treatment of the odd and even modes.

- The excitation of the even mode at discontinuities can effectively be eliminated by wirebonds, but only at low frequencies.

- The attenuation of the even mode in the 50-μm CPW with a narrow ground is equivalent to the loss suffered by a CPS defined by the CPW ground conductors. Dispersion, however, is again overestimated.

- Because the even mode suffers dramatically higher losses, the high-frequency signal asymmetries are only important at very short distances.

References

[1]   W. H. Press, B. P. Flannery, S. A. Teukolky, and W. T. Vettering, "Numerical recipes in C" Cambridge University Press, New York, NY, 1988.

[2]   M. Y. Frankel, S. Gupta, J. A. Valdmanis, and G. A. Mourou, "Terrahertz attenuation and dispersion of coplanar transmission lines," *IEEE MTT.*, vol. 39, No. 6, pp. 910-916, June 1991.

[3]   G. Hasnain, A. Dienes, and J. R. Whinnery, "Dispersion of picosecond pulses in coplanar transmission lines," *IEEE MTT.*, vol. 34, No. 6, pp. 738-74, June 1986.

[4]   M. Tsuji, H. Shigesawa, and A. A. Oliner, "New coplanar leakage behavior on coplanar waveguides of finite and infinite widths,"*IEEE MTT.*, vol. 39, No. 12, pp. 2130-2237, December 1991.

[5]   J.S. McLean and T. Itoh, "Analysis of a new configuration of coplanar stripline," *IEEE MTT.*,, vol. 40, No. 4, pp. 772-774, April 1992.

[6]   G. Goine and C. U. Naldi, "Coplanar waveguide for MMIC applications: effect of upper shielding, conductor backing, finite-extent ground planes, and line-to-line coupling," *IEEE MTT.*, vol. 35, No. 3, pp. 260-267, March 1987.

[7]   M. Riaziat, R. Majidi-Ahi, and I.-J. Feng, "Propagation modes and dispersion characteristics of coplanar waveguides," *IEEE MTT.*, vol. 38, No. 3, pp. 245–251, March 1990.

[8]   D. S. Phatak, N. K. Das, and A. P. Defonzo, "Dispersion characteristics of optically excited coplanar striplines: comprehensive full wave analysis," *IEEE MTT.*, vol. 38, No. 11, pp. 1719–1730, November 1990.
Also, D. S. Phatak, and A. P. Defonzo, "Dispersion characteristics of optically excited coplanar striplines: Pulse Propagation," *IEEE MTT.*, vol. 38, No. 5, pp. 654–661, May 1990.

[9]   K. C. Gupta, R. Garg, and I. J. Bahl, "Microstrip lines and slotlines," Norwood, MA, *Artech House*, 1979.

[10]   R. N. Simonns, G. E. Ponchak, K. S. Martzaklis, and R. R. Romanofsky, "Channelized coplanar waveguide; discontinuities, junctions, and propagation characteristics," *IEEE Int. Sump. Digest*, pp. 915–918, 1989.

Also, R. N. Simonns and G. E. Ponchak, "Modeling of some coplanar waveguide discontinuities," *IEEE MTT.*, vol. 36, No. 1796-1803, December 1988.

[11] T. Itoh, Ed., *Planar Transmission Line Structures*. New York: IEEE Press, 1987, p. 253.

[12] D. S. Rutledge, D. P. Neikirk, and D. P. Kasilingham, "Infrared and millimeter waves," vol. 10 , chapter 2, K. J. Buttton, Ed. New York: *Academic press,* 1983.

Also, D. P. Kasilingham and D. B. Rutledge, " Surface wave losses of coplanar transmission lines," *IEEE Int. Sump. Digest*, pp. 113–116, 1983.

Appendix

The experimental data presented in this thesis constitute a considerable load. Just the results in chapters 6 and 7 cover measurements on 15 different transmission lines. For each line, there were on average, more than 10 sets of separate measurements. In all, we have collected more than 200 sets of data of voltage as function of time. Converting, sorting, and comparing all this data, in a manner that could provide functionality and relatively easy access, was a challenge of its own.

Since it was known from the start that the nature of our measurements would require a large load of graphical outputs, we chose to do the data manipulation in Igor — a software package with extensive graphics support. The experimental data was converted to ASCII files and then loaded to Igor. A series of mostly small programs called *Macros* were written in order to extract the important parameters of each line. The code was written in such a way, so that the data from every transmission line could be dealt with as a cohesive unit, called a *family* of data. In this manner the operations became simple and repetitive, because they could be used in every line with minor alternations. keeping track of the results was also simplified. Most of these macros were primarily used in spectral analysis. Their code is listed in the following pages.

```
|_____

| This macro (xFtransform) takes the Fourier transform of wave called "signal" which
| has wave "time" as its time scale. It is assumed that both waves have the same
| number of points. The macro returns 3 waves: amplitude and phase, plotted as
| functions of frequency.


Macro xFtransform(signal, time)                    | wave1 to hold amplitude and
                                                   | wave2 to hold time

string signal, time
variable points=(numpnts($signal))
PauseUpdate; Silent 1                              | freeze screen to speed macro
                                                   | execution
Make /O/N= (points) afft                           | make a wave to hold the fft
Make /O/N= (points/2+1) magnitude, phase, frequency   | make 3 waves to hold
                                                      | magnitude, phase, and
                                                      | frequency
afft = $signal                                     | input amplitude and
FFT afft                                           | do the fft


magnitude = sqrt(magsqr(afft))                     | calculate magnitude and
phase = imag (r2polar(afft))                       | recover the signal phase


phase[0] = 0                                        | accumulate the phase function
Unwrap 2*Pi, phase                                  | to avoid restriction btn +/- π/2


frequency =p*1000/($time[points-1]-$time[0])        | do the frequency scaling from
                                                    | ps in time wave, to GHz


Display  magnitude Vs frequency                     | create a graph of magnitude and
Append  phase Vs frequency                          | phase vs frequency


EndMacro
|_____
```

| This Macro (alpha50cpw) estimates the frequency dependent values of *attenuation*
| and *effective dielectric permittivity* of our transmission lines. The substrate and the
| geometry dependent parameters are already inputted in the program.

Macro Alpha50cpw(points)
variable er,eq,a,b, ft, r,points | declare parameters

PauseUpdate; Silent 1 | freeze screen to speed macro execution

Make /O/N =(points/2+1) eefft, arad, acond, alpha | make 4 waves to hold effective
                                                     | permittivity, conductor,
                                                     | radiation, and total loss

er = 12.9 | er is the substrate dielectric constant
eq = (er+1)/2 | eq is the quasistatic permittivity
a = 67 | a is a geometrical parameter with value of 67
                             | for 50 μm lines
b = 1.8 | b is a geometrical parameter, as well

ft = 43 | ft is the cut-off frequency in GHz
r = 2.99*10^-8 | r is the conductor resistivity in Ω.m

| calculate effective dielectric permittivity
eeff = (sqrt(eq)+(sqrt(er)-sqrt(eq))/(1+a*(frequency/ft)^(-b)))^2

| calculate radiation loss for 50 um coplanar strips
| arad =Pi^5*((3-sqrt(8))/2)*sqrt(eeff/er)*(1-eeff/er)^2*(frequency^3)*(4.063*10^-13)*(150^2)

| calculate radiation loss for 50 um coplanar waveguide
arad = (Pi/2)^5*2*(((1-eeff/er)^2)/sqrt(eeff/er))*frequency^3*(4.063*10^13)*(150^2)

| calculate conductor loss for 50 μm CPW

```
acond=0.115*68.5*sqrt(eeff)*sqrt(r*abs(frequency))     | 0.115 converts from
                                                        | (dB/mm) to (1/mm)
talpha = arad+acond                                     | estimate total loss
```

EndMacro

|_____

| This small macro (beta) uses the values of the ε_{eff} calculated by macro Alpha50cpw
| to estimate the frequency dependent value of the imaginary propagation factor β .

```
Macro Beta(points)
variable c, points
c= 3*10^11                              | the speed of light in mm/sec


Make /O/N =(points/2+1) bet             | make wave  for propagation constant $\beta$


| calculate the propagation constant in units of mm-1
bet = 2*Pi*frequency*10^9*sqrt(eeff)/c
```

EndMacro

|_____

| The macro Propagation simulates the evolution of an input waveform "inputwave"
| (whose time scale is defined by the wave "T") at a distance "d" on a hypothetical
| transmission line. This line has a propagation factor whose real and imaginary parts
| given by the waves *talpha* and *bet*, respectively

```
Macro Propagation(inputwave,T,d)    | propagate the waveform "inputwave" a length
                                    | "d" ( in mm) on the transmission line
string inputwave,T                  | declare parameters
variable d, points


points=numpnts($inputwave)
PauseUpdate; Silent 1               | freeze screen to speed macro execution


Make /O/C/N =(points/2+1) promagn    | make a  wave for the inverse fft
```

```
Make /O/N = (points) iamplitude, iphase      | make 2 waves to hold the magnitude
                                              | and phase of the input waveform


xFtransform(inputwave,T)                      | transform input wave to the frequency domain


| Multiply by the attenuation and propagation coefficients ($\alpha$ and $\beta$).
promagn =
cmplx(real(afft),imag(afft))*cmplx(exp(d*talpha),0)*cmplx(cos(d*bet),sin(d*bet))


IFFT promagn                                  | transform input wave back to the time domain


iamplitude =real(promagn)                     | calculate inverse magnitude and phase
iphase = imag(promagn)


EndMacro

|_____

| The macro ExperimentalAlphaBeta calculates the attenuation coefficient $\alpha$ and the
| $\varepsilon_{eff}$ of a transmission line based on a set of 2 experimental waveforms (inputwave
| and outputwave) measured on this line. The 2 waveforms have 4k points and share
| the same time scale. It uses macro xFtransform to do the Fourier transforms and
| displays the value of $\alpha$ (expalpha) and $\varepsilon_{eff}$ (exeef) as functions of frequency.


Macro ExperimentalAlphaBeta(inputwave, outputwave,T, distance)


string inputwave, outputwave,T                | declare parameters
variable distance, c, points


PauseUpdate; Silent 1                         | freeze screen to speed macro execution


c= 3*10^11                                    | the speed of light in mm/sec
points=4096


Make /O/N= (points/2+1) expalpha,exbet,exeef  | expalpha = measures attenuation
                                              | exbet = dispersion and exeff takes the
```

| experimental value of ε_{eff}

Make /O/N= (points/2+1) magnitudein,phasein,magnitudeout,phaseout | make 4
                                        | waves to hold return waves

Code	Comment
wavestats /Q $inputwave	| Gate input waveform by a
$inputwave*=exp(-((x-V_maxloc)/150)^2)	| square Gaussian

Code	Comment
xFtransform(inputwave,T)	| call xFtransform to do the fft
magnitudein = magnitude	| calculate magnitude and phase of the input
phasein = phase	| waveform

Code	Comment
wavestats /Q $outputwave	| Gate output waveform by a
$inputwave*=exp(-((x-V_maxloc)/150)^2)	| square Gaussian

xFtransform(outputwave,T) | call xFtransform to do the fft

Code	Comment
magnitudeout = magnitude	| calculate magnitude and phase of the output
phaseout = phase	| waveform

Code	Comment
expalpha=ln(magnitudein/magnitudeout)/distance	| calculate exp. attenuation
exbet=(phaseout-phasein)/distance	| and dispersion
exeef =((exbet*c)/(2*Pi*frequency*10^9))^2	

Code	Comment
Display expalpha,talpha vs frequency	| create a graph of magnitude and
Append /R exeef, eeff vs frequency	| phase vs frequency

EndMacro

|_____

| The macro LowPassFilter filters the high frequencies from a waveform called
| "wave", using a specified cut-off frequency (cutoff_GHz) given in GHz. It is a
| second order filter

Macro LowPassFilter(wave,T,cutoff_GHz)

```
string wave, T                          | T should be in ps
variable cutoff_GHz,points              | define the cutoff in GHz
points=(numpnts($wave))


PauseUpdate; Silent 1                   | freeze screen to speed macro execution


Make /O/N=( points/2+1) frequency


frequency =p*1000/($T[points-1]-$T[0])   | do frequency scaling from time wave


FFT $wave                               | convert data to frequency domain
$wave =$wave/cmplx((1+(frequency/cutoff_GHz)^2),0)   | use a second order filter


IFFT $wave                              | convert filtered data back to time domain


EndMacro
|_____
| The macro HighPassFilter filters the low frequencies from a waveform called
| "wave", using a specified cut-off frequency (cutoff_GHz) given in GHz. It is a
| second order filter


Macro HighPassFilter(wave,T,cutoff_GHz)


string wave, T                          | T should be in ps
variable cutoff_GHz,points              | define the cutoff in GHz
points=(numpnts($wave))


PauseUpdate; Silent 1                   | freeze screen to speed macro execution


Make /O/N= (points/2+1) frequency


frequency =p*1000/($T[points-1]-$T[0])   | do frequency scaling from time wave
```

FFT $wave | convert data to frequency domain
$wave =$wave*(1-1/cmplx((1+(frequency/cutoff)^6),0)) | use a second order filter

IFFT $wave | convert filtered data back to time domain

EndMacro
|_____
| This Macro (Allffts) takes the FFTs of a family of waveforms that share the same
| base name(e.g. s1,s2,..s8) and creates a plot of their corresponding magnitude and
| phase. The base name, corresponding time wave, and the number of the waves are
| specified.

Macro Allffts(basename,T, distance)

string basename,name,nmag,nph,nor_ph,T,distance | declare parameters
variable count,positions

PauseUpdate; Silent 1 | freeze screen to speed macro execution

count=1
positions=numpnts($distance)

do | start loop
       name=basename+num2istr(count) | generate name of corresponding
                                         | waveform

       Make /O/N=(numpnts($name)/2+1) swap | create a wave to hold the
       swap=$name | waveform temporarily

       wavestats /Q $name | gate waveform with a
       $name*=exp(-((x-V_maxloc)/150)^4) | (Gaussian)^2 function

```
xFtransform(name,T)              |transform  wave in freq. domain
$name=swap


nmag="m"+num2istr(count)         | generate names for the waves
nph="ph"+num2istr(count)         | magnitude and phase
nor_ph="nor_ph"+num2istr(count)  |


|create magnitude wave and phase waves
Make /O/N=(numpnts($name)/2+1) $nmag, $nph,$nor_ph
$nmag = magnitude .


if (count==1)                    | generate the first graph and set
Display $nmag vs frequency       | range for 1000 GHz
Setaxis bottom 0,1000


    else
            Append $nmag vs frequency | add additional waves to graph
    endif


$nph = phase                     | send  normalized phase to graph
$nor_ph =phase/frequency         | as well
Append /R $nor_ph vs frequency   |


count +=1                        | go to transform the next wave


| check if all waves have been transformed
while(count<=positions)


EndMacro
|_____

| This Macro determines the experimental value of the attenuation and effective
| dielectric permittivity for a given transmission line–A family of waveforms that
| share the same base name (e.g. m1, m2,..m8) for magnitude and phase. It creates a
| plot of α and εeff vs frequency and compares with theoretical values. This macro is
```

I similar to macro Experimental AlphaBeta. The advantage is that now a whole
I family of waveforms can be used to extract the line parameters with better accuracy

```
Macro Exctract(magbase,phbase,z,frequency)

string magbase,phbase,frequency,z,n_mag,n_ph      I Declare parameters
variable count_z,count_f,end_f,end_z,temp,c


c= 3*10^11                          I the speed of light in mm/sec


PauseUpdate; Silent 1               I freeze screen to speed macro execution


count_f=0                           Icounter for frequency
end_f=numpnts($frequency)/8         Icounter limits for both, distance and frequency
end_z=numpnts($z)                   I


Make /O/N=(numpnts($z)) s_mag,s_ph      Icreate slave magnitude and phase waves
                                        I for distance
Make /O/N=(numpnts($frequency)) a,ef    Icreate α and εeff waves


do                                  Istart frequency loop
        count_z=1                   Iresetset counter for distance


        do                          Istart distance loop


            n_mag=magbase+num2istr(count_z)     Igenerate names of corresponding
            n_ph=phbase+num2istr(count_z)       I magnitude and phase waves


            temp=$n_mag[count_f]
            s_mag[count_z-1] = ln(temp)         I load values into distance slave
            s_ph[count_z-1] = $n_ph[count_f]    I waves


            count_z +=1                         I move to next wave at this frequency
```

```
        while(count_z<=end_z)

        CurveFit /Q line s_mag /X=$z          I calculate α and ε_eff  for this
        a[count_f]=-k1                        I frequency
        CurveFit /Q line  s_ph /X=$z          I
        ef[count_f]=((k1*c)/(2*Pi*frequency*10^9))^2

        count_f +=1                                   I increment frequency

        while(count_f<end_f)


ef[0]=ef[1]
Display a,talpha vs $frequency    Igenerate graph and set range for 500 GHz
Setaxis bottom 0,500


Append /R ef,eeff vs $frequency    I send phase to graph as well


EndMacro
I_____

IThis Macro loads a family of ASCII waveforms that share the same base name
I (e.g. nu1f2.xx) and creates the corresponding time and amplitude Igor waves.
I The number of the waves must be specified


Macro LoadWaves(inbasename,outbasename, how_many)


string inbasename,outbasename, name_in,name_out    Ideclare parameters
variable count,positions,how_many                  I


PauseUpdate; Silent 1             I freeze screen to speed macro execution


count=1
positions=1
do
```

```
name_in=inbasename+"r"+num2istr(count)          | generate names for
name_out=outbasename+num2istr(positions)         | input and output waves


Make /O/N=(numpnts($name_in)*4) $name_out        | make the waves
$name_out[1024,2047]=$name_in(p-1024)            |
|Make /O/N=(numpnts($name_in)) $name_out          |


$name_out=$name_in


if(count==1)                                      | display imported waves
        Display $name_out vs tm                   |
else                                              |
        append $name_out vs tm                    |
endif


count=count+1                                     | load next wave
positions+=1


while(positions<=how_many)


EndMacro
|_____

|This Macro determines the experimental value of the propagation velocity for a given
| transmission line. It uses family of waveforms that share the same base name
|(e.g. m1,m2,..m8) and creates a plot of propagation distance and speed vs time


Macro Velocity(base,z,time_w)      |declare parameters
string base,z,time_w, name         |distance z is in (mm) and time_w in (ps)
variable count_z,end_z


PauseUpdate; Silent 1              | freeze screen to speed macro execution


end_z=numpnts($z)                  |
count_z=1                          |set counter for distance
```

```
I create a waves to store arrival times and speed and its smoothing wave
Make /O/N=(numpnts($z)) arival_time
Make /O/N=(numpnts($z)-1) speed, sm_speed


        do                              Istart distance loop


                name=base+num2istr(count_z)        I generate name of corresponding
                Make /O/N=(numpnts($name)) slave I wave together with slave wave
                Make /O/N=(numpnts($name)) slave I


                slave = $name
                smooth 50, slave        I smooth data to avoid radiation and
                WaveStats /Q slave      Ifind maximum amplitude location


                slave*=exp(-((x-(V_minloc-30))/50)^8)      I gate to avoid radiation
                                                           I for even mode measurements
                WaveStats /Q slave
                arival_time[count_z-1] = tm[V_maxloc]      Iload time value of wave's
                                                           I maximum amplitude


                if (count_z>1)                      I use forward difference to
                speed[count_z-2]=                   I calculate velocity
        ($z[count_z-1]$z[count_z2])/(arival_time[count_z-1]-arival_time[count_z-2])
                endif


                count_z +=1                         I move to next position


        while(count_z<=end_z)


speed = speed*10/3          Iconvert speed as a fraction of the speed of light
sm_speed = speed
smooth 2, sm_speed
```

```
Display $z vs arival_time          |generatete graph of prop. distance Vs time
Append /R speed, sm_speed vs arival_time       | send speed to graph


EndMacro
|_____
```